**Material Characterization of Leadfree SAC Solder Alloys at High Strain Rates with Finite Element Analysis**

by

Sandeep Shantaram

A dissertation submitted to the Graduate Faculty of
Auburn University
in partial fulfillment of the
requirements for the Degree of
Doctor of Philosophy

Auburn, Alabama
December 14, 2013

Keywords: High Strain Rate, Lead-free Solder, SAC, Peridynamics, Drop, Shock

Approved by

Pradeep Lall, Chair, Thomas Walter Professor of Mechanical Engineering
Jeffrey C Suhling, Quina Distinguished Professor of Mechanical Engineering
George T Flowers, Professor of Mechanical Engineering
Michael J. Bozack, Professor of Physics

Abstract

The electronics may experience high strain rates under single, sequential and simultaneous exposure to thermo-mechanical and transient dynamics loads at various stages of their life-cycle i.e. manufacturing, transportation, and deployment in field. Models for high-g electronic survivability require high strain rate properties of materials for different loading scenarios. Second-level interconnects have high susceptibility to failure in fine pitch electronics. In the recent past, the electronics industry has migrated to lead-free solder alloy compositions or so called "green" products under the ROHS initiative. Tin-Silver-Copper (SnAgCu or SAC) alloys are being widely used as replacements for the standard 63Sn-37Pb eutectic solder. High strain rate properties of electronic materials are scarce.

In this research work, a new test-technique developed by the author has been presented for measurement of material constitutive behavior. The instrument enables attaining strain rates in the neighborhood of 1 to 100 sec$^{-1}$. The high strain rate properties of Sn1Ag0.5Cu and Sn3Ag0.5Cu lead-free solder alloys under prolonged exposure to high temperature have been measured. An impact hammer has been used in conjunction with digital image correlation and high-speed video for measurement of material constitutive behavior of lead-free SAC alloys in the strain rate range of 1-100sec$^{-1}$. Thin-bar samples have been fabricated by reflowing solder in glass tubes using reflow profiles typical of lead-free assemblies. Bar sample thickness has been selected to be in the neighborhood of typical heights of solder interconnects in fine-pitch electronics. Sn1Ag0.5Cu and Sn3Ag0.5Cu specimen have been subjected to various lengths of

aging temperatures, aging times (0-2 months) and strain rates. Rate independent material AL7075-T6 has been used as a bench mark experiments at various strain rates in the range of 1-100 sec$^{-1}$. The experimental data has been fit to the Ramberg Osgood model and implemented in the finite element analysis for full-field strain correlation between DIC and simulation.

Also when electronics are subjected to high strain rates during accidental drop and shock there are high possibility of second level solder interconnects to fracture completely due to dynamic crack propagation. Additional failure modes may include copper trace fracture, underfill cracking, chip delamination and chip cracks. Previously, modeling approaches are based on the classic continuum theory of solid mechanics which uses partial differential equations (PDE). Since, PDE are not valid in presence of discontinuities such as cracks, voids, any numerical scheme derived from these equations fails to model cracks. Henceforth, such methods require auxiliary equations that govern the damage initiation and damage progression. These auxiliary equations get more complicated to solve discontinuities which can occur simultaneous at multiple locations in 3D fashion. In order to overcome these modeling issues an alternative theory know as peridynamic theory which uses integral equations has been implemented in this work. Peridynamic scheme reformulates the basic mathematical description of solid mechanics in order to retain the same equation on or off the discontinuity location. Previosuly, feasibility of using peridynamics in drop simulation of electronics has been demonstrated using EMU code. Use of finite element based peridynamics for electronics packaging under drop and shock in this work is new.

Acknowledgments

Table of Contents

List of Tables

List of Figures

xvi

## Chapter 1

## Introduction

### 1.1 Electronic Packaging

Electronic Packaging is an art (based on Science) of establishing interconnection between various levels of electronic devices, components, modules and systems [Suhling 2007]. In this dissertation, electronic packaging refers to packaging of microelectronics (i.e. semiconductor chips). The main function of electronic packaging are signal distribution, power distribution, heat dissipation and protection (mechanical, chemical, and electromagnet) of components and interconnection.
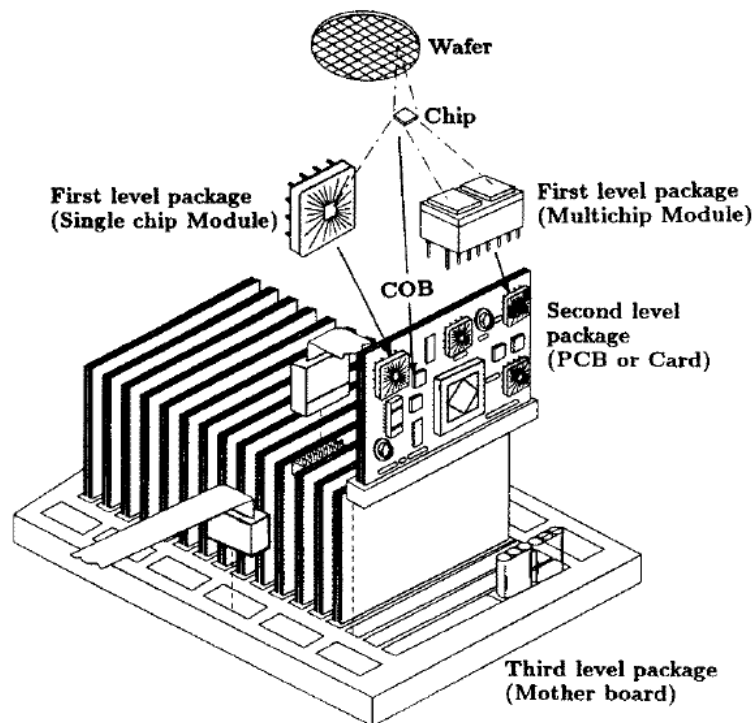
Figure 1.1: Hierarchy of Electronic Packaging (source: Suhling 2007)

Figure 1.1 provides the hierarchy of electronic packaging. In this dissertation emphasis is on the reliability of second level package (board level) with the surface mount components subjected to high strain rate events such as drop and shock.

## 1.2 Soldering for Second Level Package

Soldering is defined as a metallurgical process in which minimum two metallic surfaces are joined together by melting a filler metal at the joint. Relatively low melting point filler metal (usually below 425 °C) is termed as solder [Rahn 1993]. In electronic industry, solders are mainly used to attach discrete components to printed circuit boards (PCBs). These attachments typically also serve as the electrical interconnection between the attached components and the PCB [Puttlitz 2004]. There are two main assembly line soldering processes which have been widely implemented which are reflow soldering (surface mount) and wave soldering (plated-through-hole and surface mount).



(a)



PTH                          SMT

(b)
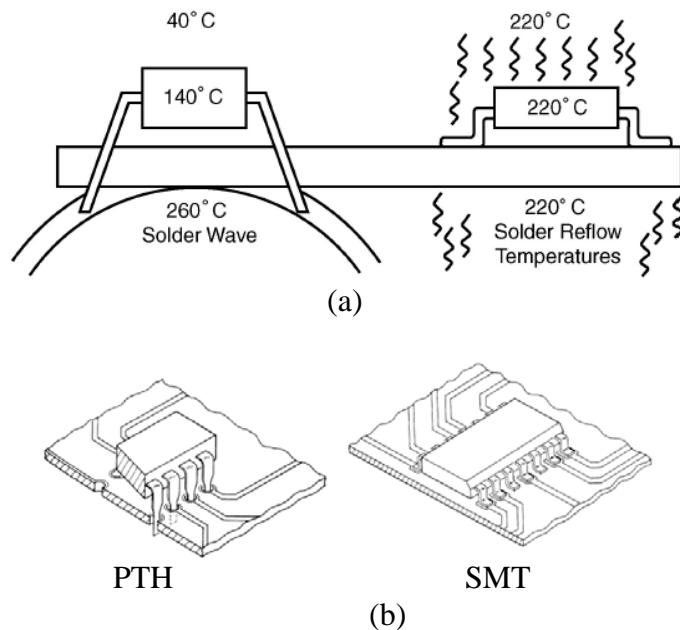
Figure 1.2: (a) Major assembly line solder process (b) plated-through-hole technology (PTH) and surface-mount technology (SMT) [source: Suhling 2007]

### 1.3 Soldering Materials for Second Level Package

### 1.3.1    Tin-Lead (Sn-Pb) Soldering Materials

Usage of lead based solder materials such as 63Sn-37Pb (a eutectic composition) had been widely accepted in electronic industry, but most notably the use of eutectic tin-lead (Sn-Pb) solders to attach discrete components to PCBs [Puttlitz 2004].  The Sn-Pb binary system features a melting eutectic temperature as low as 183 °C and provides material compatibility with most substrate materials and devices [Zhang 2010]. The lead has many advantages over other alloying elements which is a primary component in tin lead solder. Some of the advantages of leaded solders are: Pb facilitates wetting by reducing the surface tension of Sn-Pb solders. Pb is inexpensive and readily available with no patent issue. Also, extensive research has been carried out on the physical metallurgy, mechanical properties, flux chemistries, manufacturing processes and reliability of Sn-Pb solders [Zhang 2010]. However, the electronics industry has migrated to leadfree solder alloy compositions or so called "green" products under the Restriction of Hazardous Substance (ROHS) Directive initiative. Worldwide consumption of lead-free solder is now at 68% [Figure 1.3].

**Global Consumption  of Tin/Lead versus Lead Free Solder for
1st Quarter 2012
(Solder Shipments in Kg)**

Tin/Lead
32%
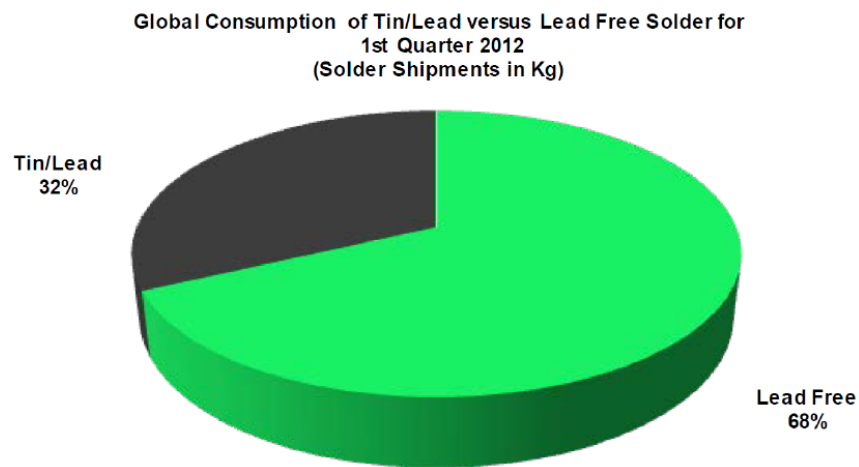
Lead Free
68%

Figure 1.3: Global consumption of Sn-Pb vs Pb-free solder for the 1st quarter 2012 [Source: Market Research Services]

### 1.3.2 Lead-free Soldering Materials

*Lead-free definition*, "Component and assembly Pb content shall be less than 0.1% by weight of the device (in accordance with IPC/EIA J-STD-006) and shall not be intentionally introduced." Source: http://golledge.com/docs/products/rohscentral.htm. Also, many electronic industries have adopted a 0.1% maximum residual lead content (this value appears arbitrary and not based on some health-related threshold value) [Puttlitz 2004].

### 1.3.3 Selection Criteria for Lead-free Solder Candidates

In order to replace Sn-Pb solders in electronic assemblies, the lead-free solders must satisfy a very wide range of properties and characteristics. Lead-free solder candidates has to be compatible according to the packaging trend such as densification to meet the demands for more functionality and portability while withstanding increased mechanical, electrical and thermal loads, which reduces the reliability and eventual failure during manufacturing, shipping and in the field. There are two basic requirements that all the solder interconnection alloys must satisfy [Puttlitz 2004].

(1) Solder must wet and bond to metallic terminals or features on components and substrates.

(2) Solder must have a melting point that is sufficiently low to be reflowed as paste when surface mount reflow attaching components to PCBs, yet high enough to avoid any ill effects due to operating temperatures in the field.

There are about 70+ lead-free solder alloys candidates available in the literature including binary, ternary, quaternary alloys [Abtew 2000]. For most of the solder alloy candidates, Sn-rich alloy with Sn serving as primary or major constituents [Zhang 2010].

### 1.3.4   Tin (Sn)-Silver(Ag)-Copper(Cu) (SAC) Series Alloys

SAC series, a ternary system obtained from Sn-Ag and/or Sn-Cu binary systems, has been widely accepted by major electronics manufacturers. Lead-free SAC solder alloys have many advantages over the other lead-free system including relatively lower melting temperatures, superior mechanical properties, solderability properties and good tolerance for Pb combination [Zhang 2010, Lee 1999, Lopes 2003]. Figure 1.4 provides the strong evidence of SAC series alloys world-wide acceptance.
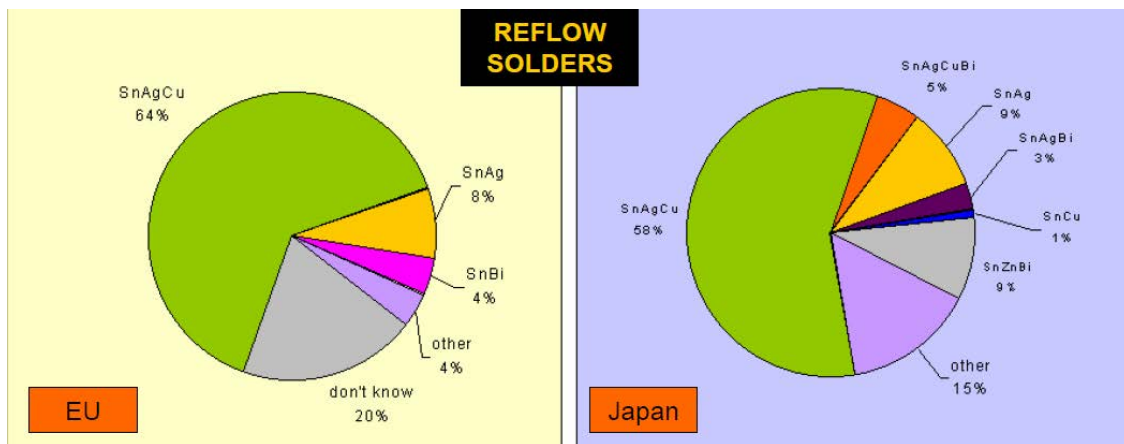


Figure 1.4: Lead-free solder Market share [Lopes 2003]

Though the SAC series alloys have many benefits with high market share it's not a perfect Pb-free replacement choice due to many short comings:

(1) High reflow temperatures are need for SAC alloys since they have higher melting points as opposed to eutectic Sn-Pb [Zhang 2010, Cai 2012].

(2) Reliability issue due to excessive growth of intermetallic compounds at the solder interface between solder joints and copper pads [Zhang 2010, Cai 2012].

(3) SAC alloys have higher material costs [Zhang 2010, Han Cai 2012].

(4) Patent issues [Cai 2012]

(5) Aging effects SAC alloys i.e. loss in the material strength even at room temperature over a period of time [Zhang 2010, Cai 2012].

### 1.3.5 SAC Phase Diagram

Ternary system, SAC series, eutectic melting temperature is of great importance and interest since they are replacing the traditional Sn-Pb solders.
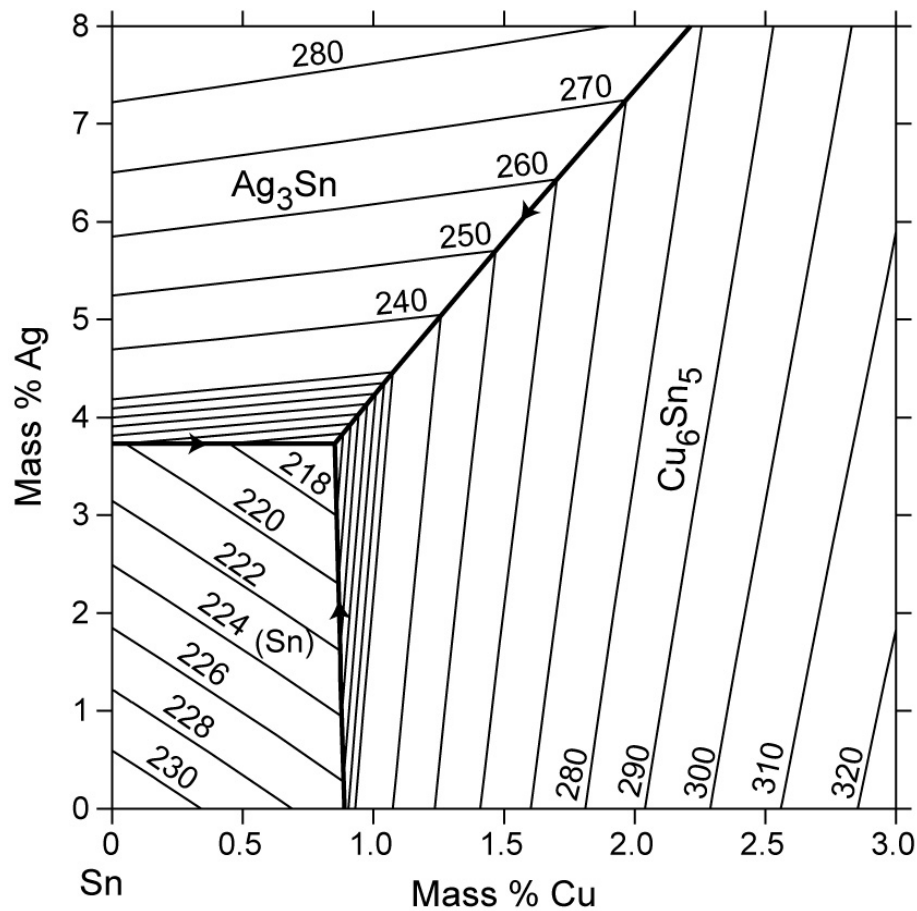


Figure 1.5: Sn-Ag-Cu Ternary Phase Diagram
(http://www.metallurgy.nist.gov/phase/solder/solder.html)

The eutectic composition of SAC series alloys was first discovered by Miller, et al. in 1994 using DTA [Zhang 2010]. The eutectic point was 4.7 wt.% Ag and 1.7 wt.% Cu in the ternary system

and the corresponding melting temperature of 217°C. This composition was refined to 3.5 wt.% Ag and 0.9 wt.% Cu by Loomans and Fine in the year 2000 who used thermal analysis of monovariant Sn-Cu and Sn-Ag binary eutectics. Their work was then confirmed using thermal analysis [Moon 2000], simulated DTA curves and thermodynamic calculations. The melting point of the ternary system was fixed to 217.2 ± 0.2 °C [Zhang 2010]. Figure 1.5 shows the ternary phase diagram of Sn-Ag-Cu within red region termed as near eutectic composition.

**1.4 Major Cause of Electronics Failure**

Electronics can be subjected to harsh environments such as extreme high/low temperatures, vibration/drop/shock, corrosion/radiation/pressure, during manufacturing, transportation, field applications which results in the product failure. In this work, the main focus is on reliability analysis of lead-free handheld electronics such as cell phones subjected to high strain rate events such as drop and shock with and without sequential thermal loads.
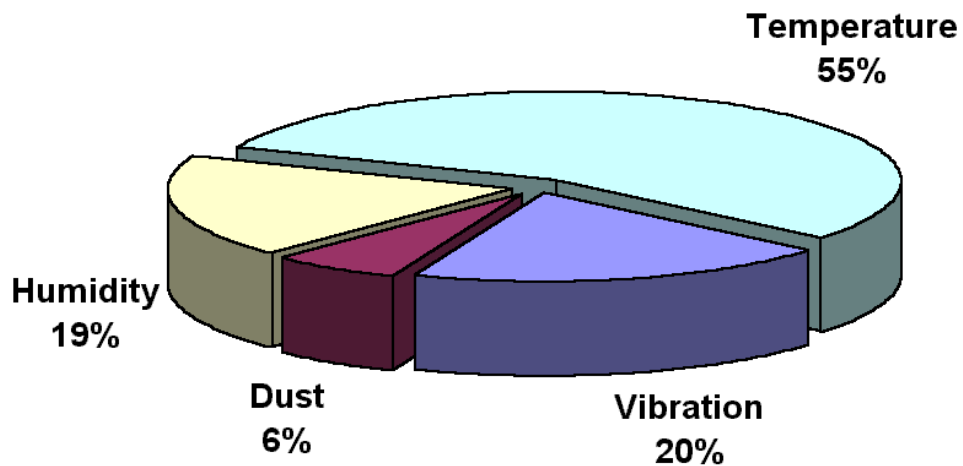


Figure 1.6: Major causes of electronic failure [source: U.S. Air Force Avionics Integrity Program, Reynell, M. 1990]

**1.5 Drop/Shock - Transient Dynamic Vibration in Handheld Electronics**

Shocks events are transient dynamic condition where a single impulse of energy is transferred to a system in a short period of time (milli-seconds) with large acceleration such as dropping of handheld devices. Handheld electronics includes cameras, calculators, cell phones, pagers, palm size PCs, Personal Computer Memory Card International Association (PCMCIA) cards, smart cards, personal digital assistants (PDAs) and other electronic products that can be conveniently used while held in user's hand. These handheld electronic products may be subjected to drop during manufacturing, shipping and operational periods. These drop events may not only results in mechanical failures in the housing of the devices but also causes electrical failures in the PCB assemblies mounted inside the housing due to energy transfer through PCB supports. Various failures modes includes cracking of solder interconnections between components and the boards, cracking of PCB, copper trace cracking on board, component cracks (Figure 1.8). The primary driving force of these failures is excessive flexing of circuit board due to input acceleration created from dropping the handheld electronic product [JESD22-B111 2003]. (Figure 1.7). When the board flexes due to drop events, it results in the relative motion between the board and the component mounted on it as a result component, interconnect or board fails. It should be noted that the failure is function of the combination of the board design, construction, material, thickness, surface finish, interconnect material, standoff height and component size [JESD22-B111 2003]. Also, in recent years, trends towards miniaturization of the fine pitch electronics have resulted in the increased susceptibility to failure in shock and vibration which are high strain rate events. A basic understanding regarding failure mechanism accompanied with analytical, experimental, numerical and statistical techniques, is necessary to enable product reliability over the design life.

At rest,

Mold

Solder

PCB

Board flexing due to
shock event
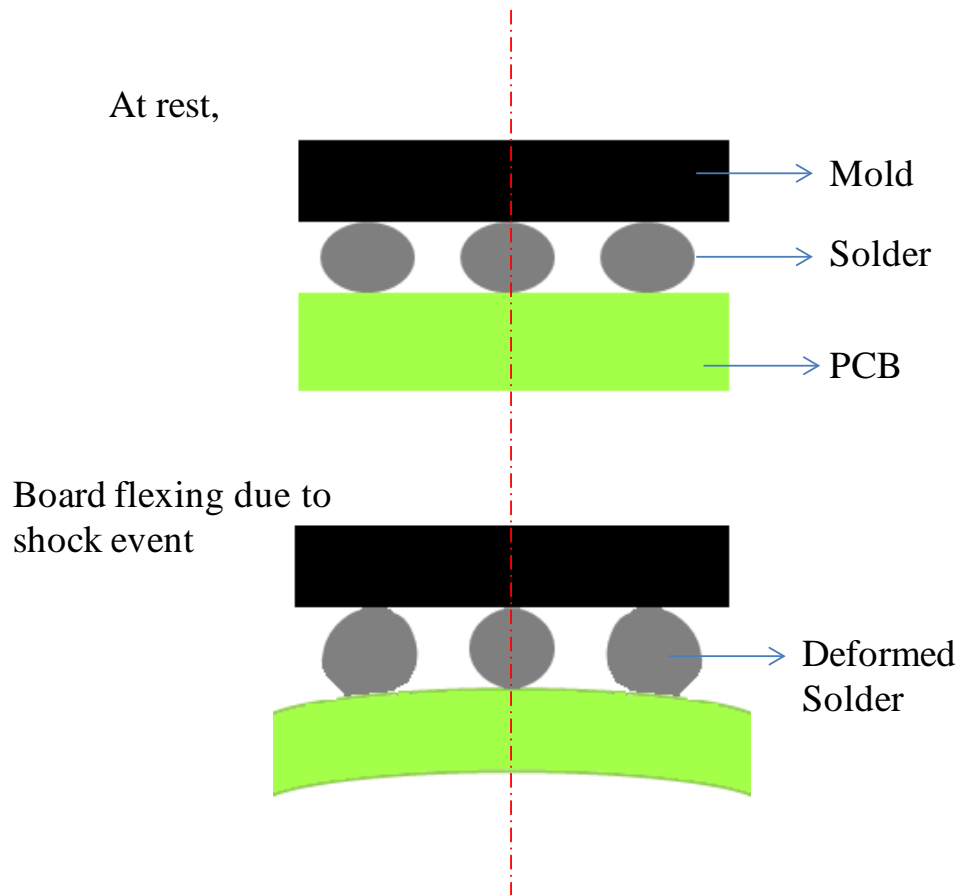
Deformed
Solder

Figure 1.7:  Typical PCB assembly deformation under shock and vibration load with normal stress component (solder interconnect axis) being dominant for deformed solder

Drop/shock is a high strain rate events and the solder interconnects which are Pb-free materials are strain rate dependent (i.e.solder mechanical properties are function of strain rates). Thus, it is important to know the solder material behavior at high strain rates to determine solder joint reliability in shock and vibration scenarios.

## 1.6 Mechanical Testing of Solder Material

Solder joint which are bonding material provides electrical, mechanical and thermal continuity in PCB assemblies. It is important to know the solder joint properties for their reliability concern. Solder joint reliability is the ability of solder joints to remain in conformance

with their mechanical and electrical spec over a given period of time for a given operating conditions [Zhang 2010]. Most failure which occur in the electronic packages in drop/ shock events are across solder joint since they are the weakest link in the entire structure as shown in Figure 1.8. This type of failure, are associated with mechanical behavior of solder alloys, is usually called mechanical failure of solder joints.
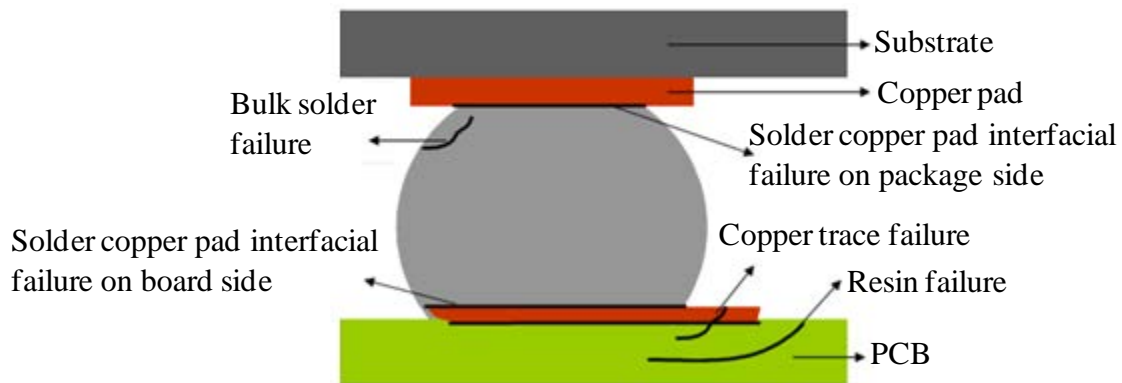


Figure 1.8: Types of failure mode across solder joint in drop/shock event

Mechanical testing of materials is typically performed for one of the following reasons [Han 1992]:

(1) Test Development: to create or refine the test methods itself

(2) Design: to create or select materials for specific applications

(3) Quality Control: to verify that incoming material is acceptable.

### 1.6.1 Uniaxial Tensile Testing

Uniaxial tensile testing is one of the most commonly performed mechanical tests. In this test, it involves griping a test specimen at both ends and subjecting it to increasing axial load until the specimen rupture/breaks. During the test, recording the load and the elongation data enables to determine several characteristics about mechanical behavior of the material. To obtain

meaningful data, one has to understand the factor that affects test results. Also, to use tensile data effectively, one has to understand the connection between actual material behavior and the data generated by tests. Figure 1.9 shows the typical tensile specimen. Tensile specimen may or may not have shoulders. Shoulders are provided for gripping tensile specimen for specific grippers. Gauge length should be much larger than its width or diameter for rectangular cross-section and circular cross-section respectively. This condition is necessary to achieve uniaxial loading conditions. Otherwise, stress state will be more complex than a simple tension. Also, specimen has to be perfectly straight because an initially bent specimen will create non axial loading.
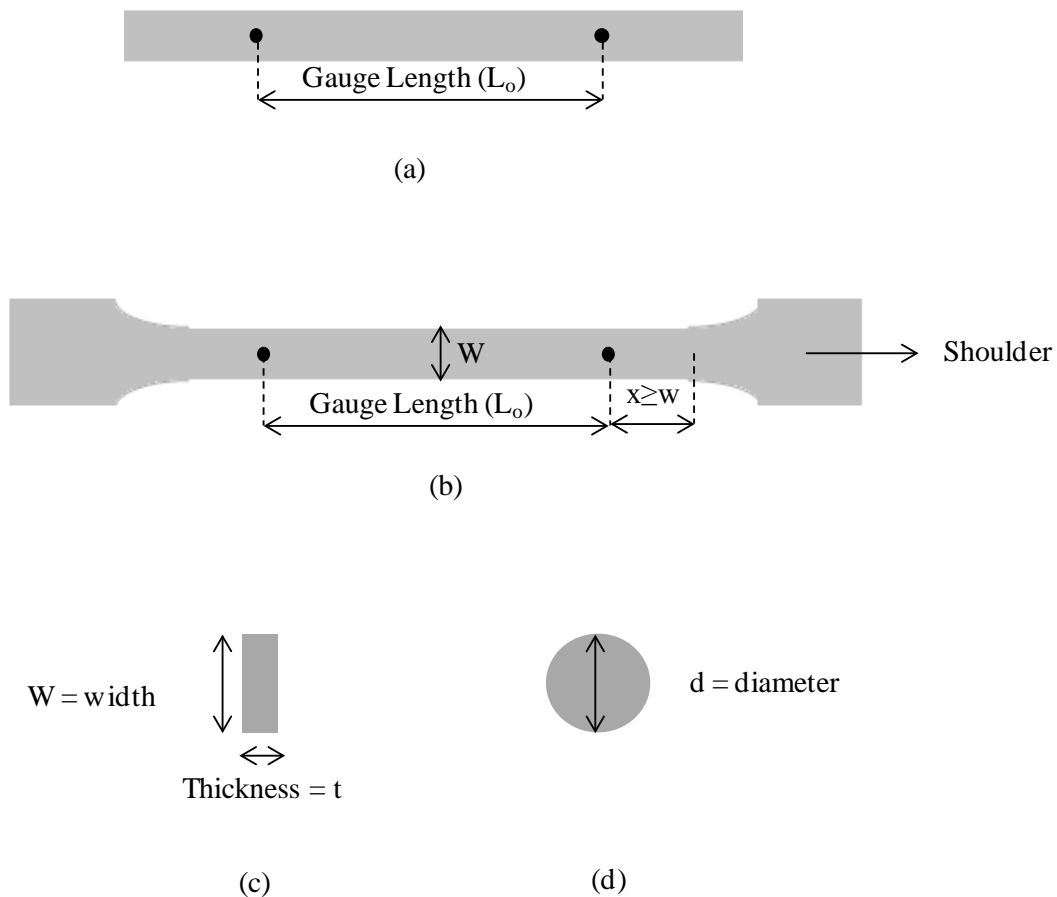


Figure 1.9: Typical tensile specimen (a) without shoulders (b) with shoulders (c) rectangular cross-section (d) circular cross-section

For tensile testing, there are many ways to grip the specimen, some of the methods are illustrated in Figure 1.10. The ends may be connected to serrated grip, may be screwed into threaded grip, pin grip can be used or solid collar grip can be used. The most important requirement is to ensure that the specimen can be held at maximum load without slippage or failure in the grip section.
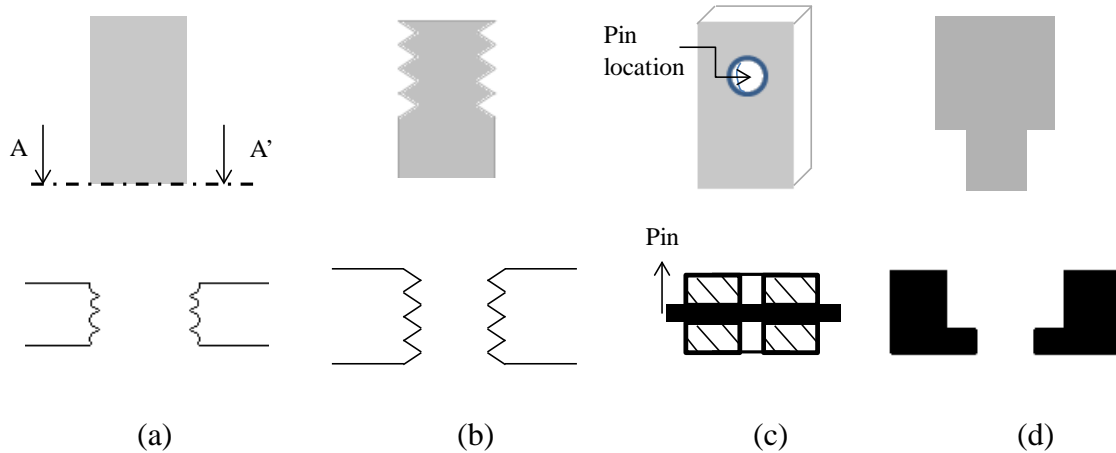


Figure 1.10: System for gripping tensile specimen (a) serrated grip (b) threaded grip (c) pin grip (d) solid collar grip

Tensile test setup requires that the specimen be properly aligned with a rigid unworn grip/crosshead. The actual physical alignment of the two ends of the test specimen becomes crucial, because (a) an off-centered loading will create bending load onto the specimen (b) also if specimen major axis is initially tilted with respect to its loading direction than there could be significant stress components within the test specimen other than its major axis direction. Including the specimen alignment other alignment will be affected by the testing machine load frame, any grip or fixtures used.

$\theta^0$

Cross head

F=force

Metal bolts

Specimen

F=force

(a) Wrong

Not centered

(b) Wrong

$90^0$
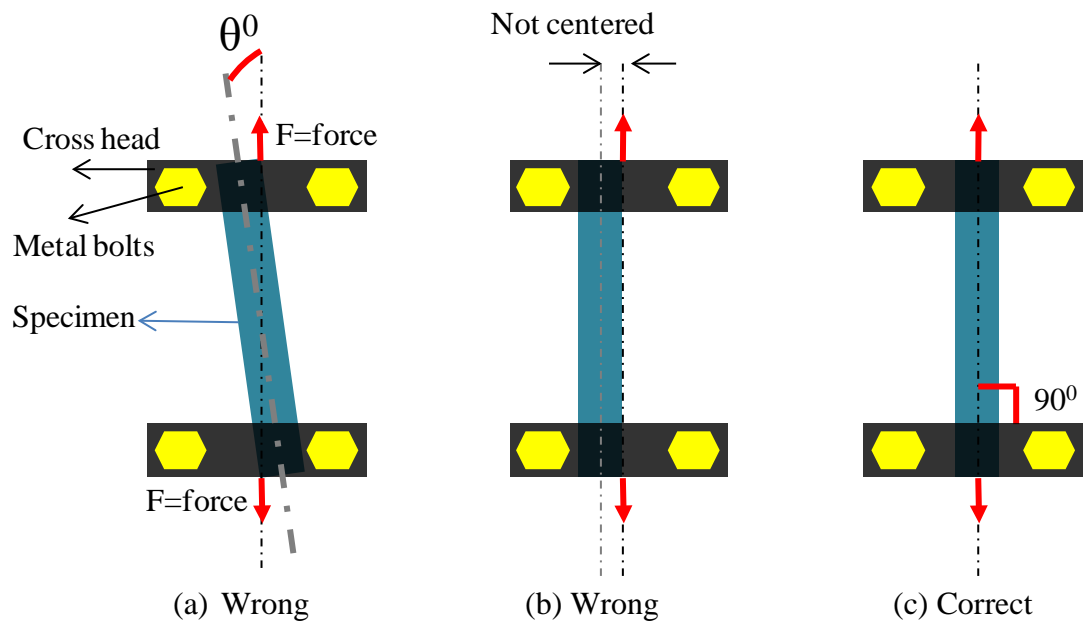
(c) Correct

Figure 1.11: Specimen alignment under grip (a) specimen not parallel to the test direction (b) specimen off-centered (c) correct specimen alignment

**1.6.2 Concept of Elastic and Plastic Deformation**

When a solid material is subjected to a small load then the material undergoes small deformation (change in shape). When the load is removed then the material returns to its original shape. This complete reversible deformation is termed as elastic deformation. If the deformation is not recovered i.e. if the material is permanently deformed even after the removal of the load then it is termed as plastic deformation (Figure 1.12).
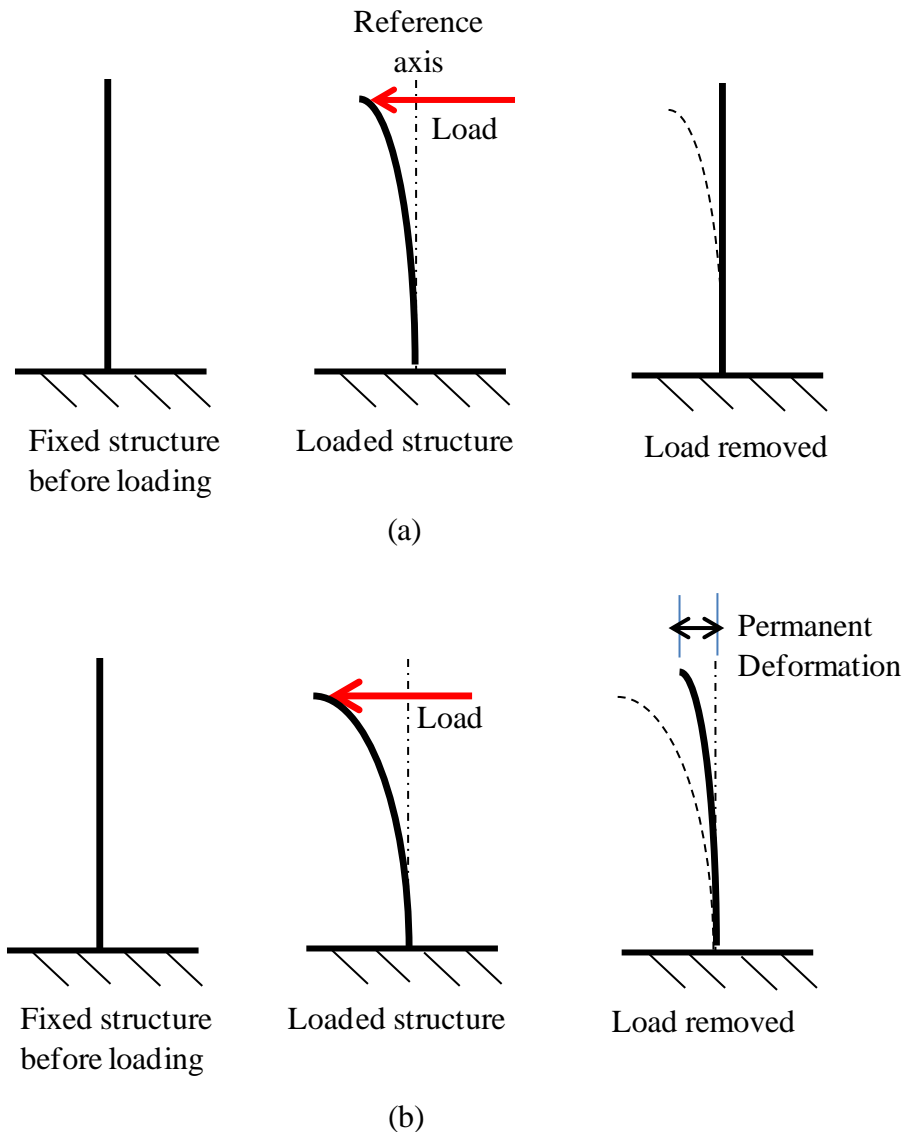


Figure 1.12: Concept of (a) Elastic deformation and (b) Plastic deformation

### 1.6.3 Tensile Tester

Tensile testers are the equipment which consists of several types of devices used to apply controlled tensile loads to test specimens. Tester should be capable of varying the speed of load application and accurately measure the forces, elongation applied to the test specimen. Figure 1.13 shows the commercial tensile tester. It consists of load cell to measure the load applied to the test specimen. Specimen extension is usually measured using extensometer or strain gauge system. Figure 1.14 (a, b) shows the typical tensile test data.
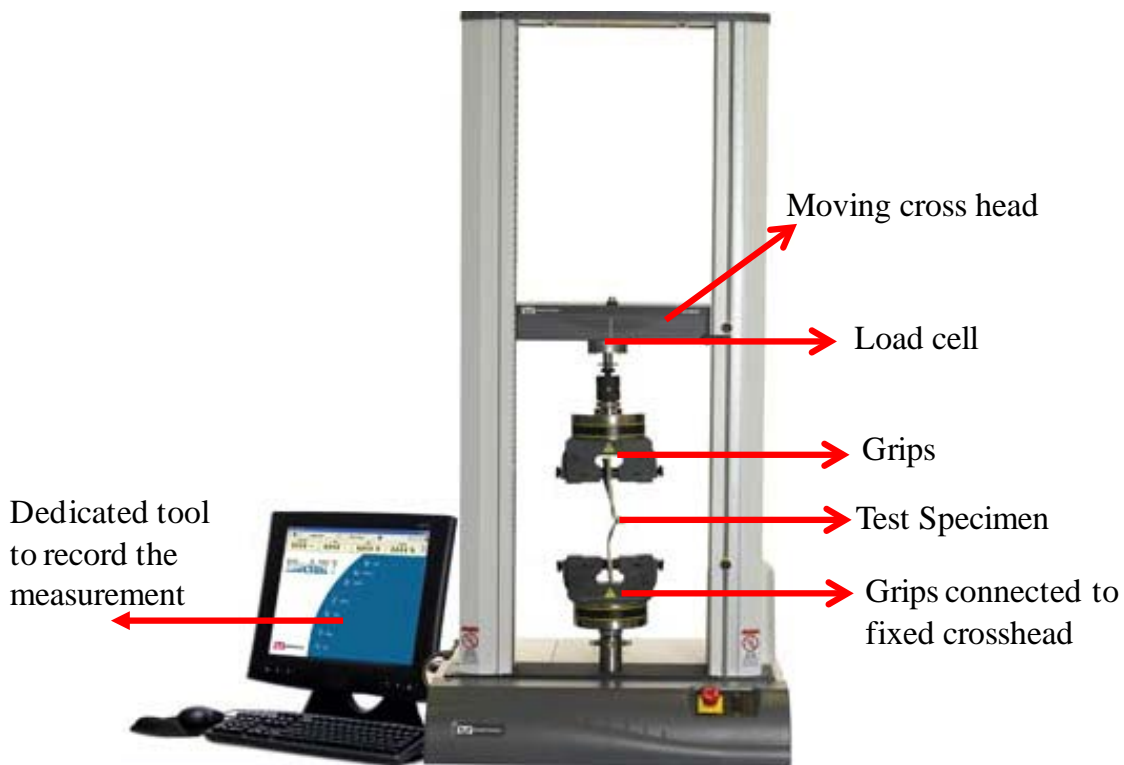


Figure 1.13: Typical Tensile Tester (Source: http://www.instron.us/wa/product/3300-Dual-Column-Testing-Systems.aspx)

### 1.6.4 Force-Displacement and Stress-strain Relationship:

$Force = Stiffness \times Displacement$

$F = Kx$ (1.1)

Engineering Stress = Force/original cross-sectional area

$$\sigma = \frac{F}{A_0}$$ (1.2)

Unit for Stress:

$$\frac{Newton(N)}{meter - Square(m^2)} \quad Or \quad Pascal(Pa) \quad Or \quad 10^6 Pa = MPa$$

Engineering Strain = Change in length (mm)/ Original length (mm)

$$\varepsilon = \frac{x}{L_0}$$ (1.3)

Within the linear elastic portion, stress and strain are related by Hooke's law:

$\sigma = E\varepsilon$ (1.4)

Where E = elastic modulus or Young's modulus
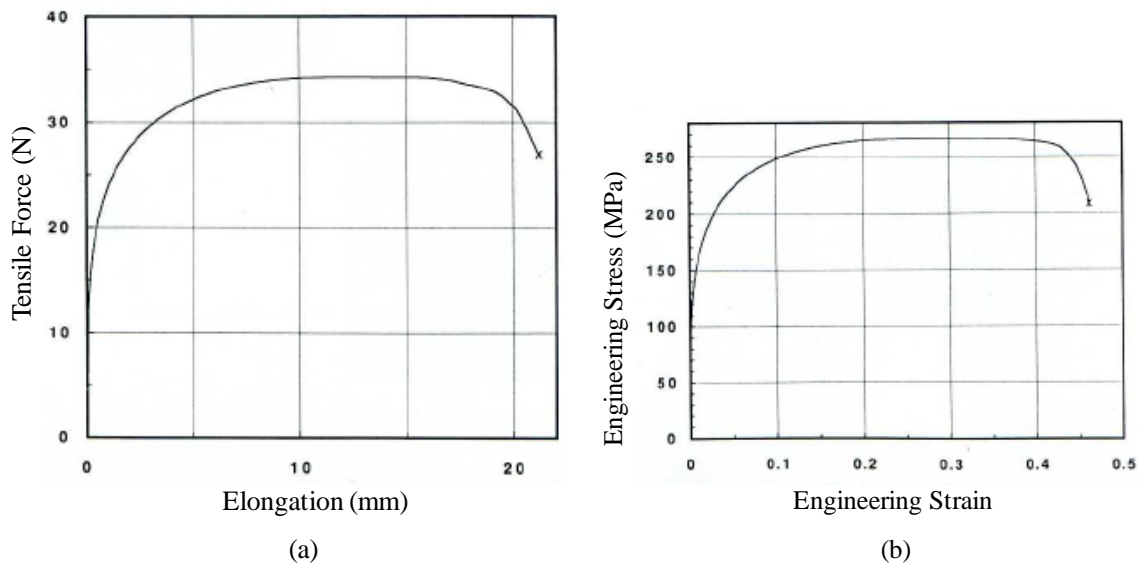


Figure 1.14: (a) Load-Elongation curve from tensile test and (b) corresponding engineering stress-strain curve. Specimen diameter 12.5 mm and gage length 50 mm [Han 1992].

Tensile specimen can undergo pure elastic deformation (brittle materials like high carbon steel) or elastic with perfectly plastic deformation, for example by certain steels (1025 carbon steel) and certain low-strength magnesium alloys or elastic deformation and then plastic deformation with strain hardening effect (Sn-Pb or SAC solder alloys) as shown in Figure 1.15. Once the material properties are experimentally determined then the same properties can be applied to determine state of stresses and strains in more complex loaded structures since the properties are independent of material dimensions.
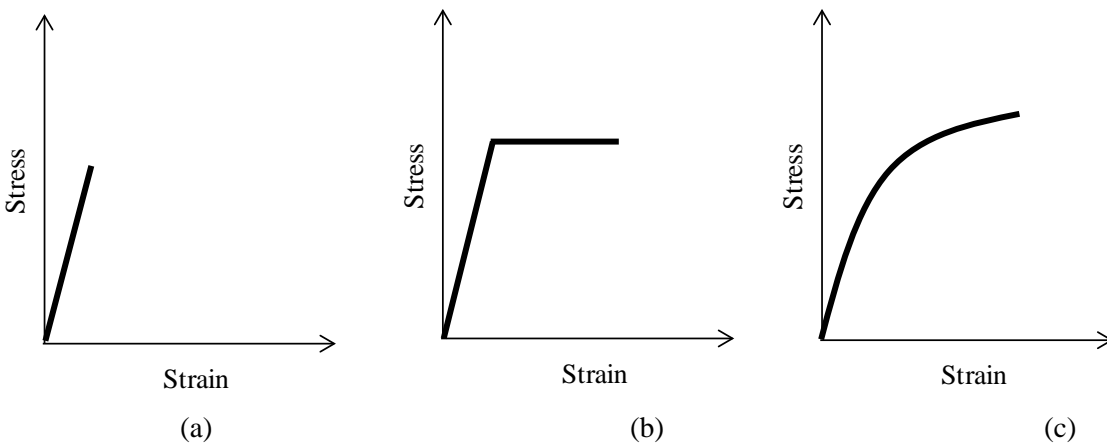


Figure 1.15: Tensile data (a) Pure Elastic deformation (b) Elastic with perfect plastic behavior (c) Elastic deformation and plasticity with strain hardening effect.
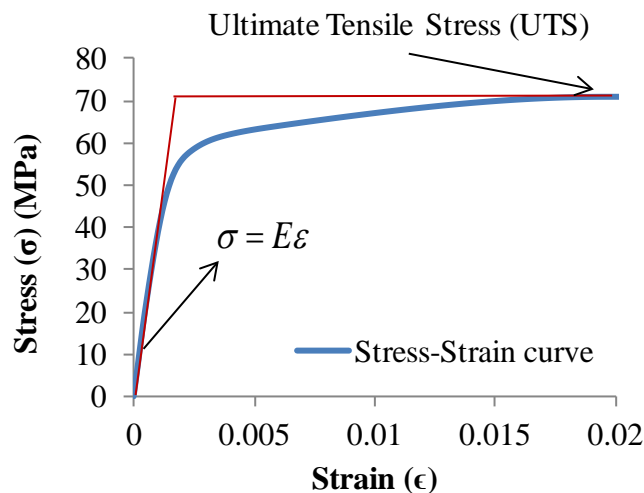


Figure 1.16: Typical Stress-strain curve of Pb-free Alloys [Zhang 2010]

17

### 1.6.5 Strain Rate Effect

Strain rate is defined as rate of change of strain with respect to unit time. On the stress-strain curve, the effect of strain rate is often neglected. For many metallic materials at room temperature, the strain rate has only a small effect on the level of stress-strain curves. Typically, materials are tested at low strain rate values well below 1 ($\dot{\varepsilon} << 1$). For drop/ shock events, solder interconnect experience high strain rates in the neighborhood of 1-100 sec$^{-1}$. For most of the engineering materials at high strain rates their material properties differ with respect to low strain rate properties. Hence it's crucial to know the accurate material properties as a function of strain rates.
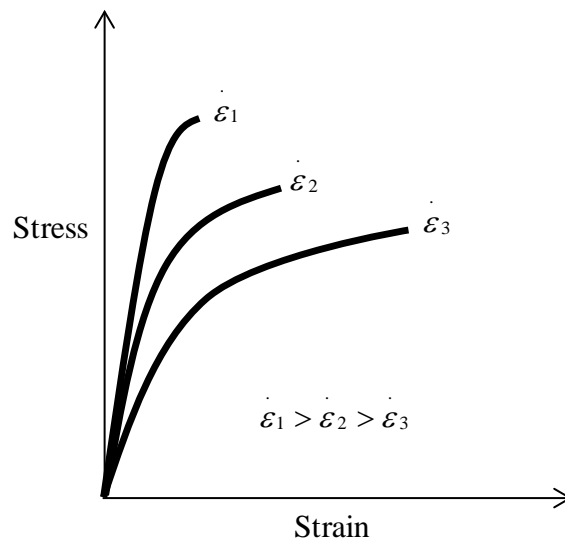


Figure 1.17: Strain rate effect on tensile behavior.

### 1.7 Finite Element Analysis (FEA)

FEA is a numerical method to address field problems. A field problem involves in determination of spatial distribution of one or more dependant variables such as displacement, stress and temperature. FEA involves discretization of continuous structure into discrete elements. Elements are connected at a point called nodes. The complete assemblage of elements

is termed as finite element structure [Figure 1.18]. Mathematically, FE structure is represented by a system of algebraic equations to be solved for unknowns such as displacement at nodes. In FEA, field quantity over the complete structure is approximated element by element in piecewise function.
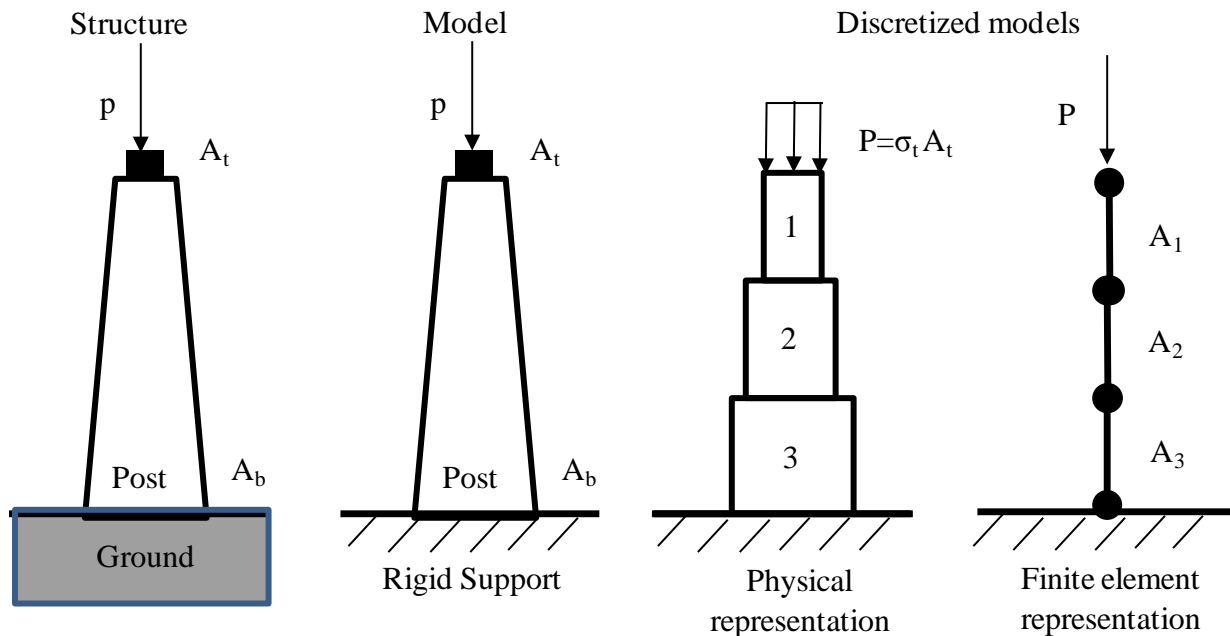


Figure 1.18: Steps involved in modeling and FE analysis of tapered support post [Cook 2005]

Advantages of FEA [Cook 2005]:

(1) FEA is applicable to any field problems such as stress analysis, heat transfer, magnetic field etc.

(2) No geometric restrictions.  Body to be analyzed can have any shape.

(3) Boundary conditions and loading conditions are not restricted.

(4) Material properties of structure to be analyzed are not restricted. Further, properties can change from element to another or even within an element.

(5) Different behavior and different mathematical description for the components can be combined. For example, single FE model can have bar, beam, plate and shells so on.

19

(6) Approximation of the modeling technique can be improved by increasing the elements density where field gradients (such as stress) are high and more resolution is required.

For the electronic components subjected to drop/shock event can not only undergo large deformation but also fails as described in the Drop/Shock - Transient Dynamic Vibration in Handheld Electronics section. Conventional FEM is used to solve field problems which do not involve voids or crack initiation and growth. FEM is based upon governing equations which are partial differential equations (PDE) and PDEs is used to solve continuum structures since PDEs are not valid in the presence of discontinuities such as crack. The spatial derivatives needed for these PDEs to make sense do not exist on a crack tip or surface. In order to address crack growth issue within FEM frame work there are few alternative techniques evolved over the time which includes stress intensity factor (SIF) method based upon fracture mechanics, extend finite elements (Xfem), cohesive zone modeling (CZM) approach. These techniques get more complicated to solve discontinuities which can occur simultaneous at multiple locations in 3D fashion. In order to overcome these modeling issues an alternative theory know as Peridynamic theory which uses integral equations has been implemented via FEA in this work.

**1.8 Dissertation Organization**

This dissertation is divided into following chapters:

Chapter 1: Introduction to electronic packaging and Pb-free soldering alloys. In this chapter emphasis is on issues associated with the drop/shock events of portable electronics. Material testing using uniaxial tensile testing method and finite element analysis for mechanical loaded structure.

Chapter 2: Literature survey on drop/shock tests for portable electronics. Material properties of lead-free solder alloys at high strain rates. Aging effects on lead-free solder alloys. Constitutive model for tensile test data of SAC solder alloys. Digital image correlation for drop/shock events. Finite element analysis for portable electronic subjected to impact loads such as drop/shock.

Chapter 3: Material characterization of lead-free SAC solder alloys at high strain rates. This chapter includes experimental set-up for high strain rate material testing, effect of high strain-rate on mechanical properties of SAC Lead-free Alloys. Ramberg-Osgood's Nonlinear Model used to fit the nonlinear stress-strain curve and implemented in the commercial finite element code.

Chapter 4: Peridynamic via finite element analysis for lead-free electronic under drop/shock. This chapter includes Peridynamic based finite element model for high speed uniaxial tensile test all the way till specimen rupture. Peridynamic model for zero-degree drop test of second level package subjected for high G load over 10,000 G-level.

Chapter 5: Summary and Conclusion of the dissertation

# Chapter 2

# Literature Survey

## 2.1 Introduction

The handheld electronic products such as cell phones and cameras etc are often subjected to impact loads such as drop and shock during manufacturing, transportation and their actual service life. As a result, entire assembly is subjected to high strain rates and typically solder interconnects which are the weakest links in the entire structure fails due to bending of PCB.

## 2.2 Drop/Shock Test for Portable Electronics

Figure 2.1 shows typical drop tester and mounting scheme for PCB assembly. JEDEC drop test is most commonly adopted experimental methods to address shock and vibration reliability for portable electronics. In this method, test boards are subjected to a 1500g pulse for 0.5 milliseconds half-sine pulse in $0^0$ horizontal drop orientation. This standard has been largely accepted and implemented by researchers to compare reliability results.

The JEDEC standard specifies that the test vehicle should be mounted with the package side facing downwards. This downward facing package creates a more critical loading condition [Yeh 2004]. It also states that the drop orientation should be horizontal which is zero degrees during the drop test. Since this is not the only angle at which a product might hit the floor previous researchers have conducted experiments on cell phones by Liu et. al. [Liu 2005], Seah et. al. [Seah 2002], Ong et. al. [Ong 2003] and Lall et. al. [Lall 2006[a,b]] showing that impact reliability is very sensitive to the impact angle of the product. Chong et. al [Chong 2005].

reported that pin-supported vertical drop of PCB generated much lower PCB flexing and impact stress damage to the solder joints compared to the horizontal orientation drop.
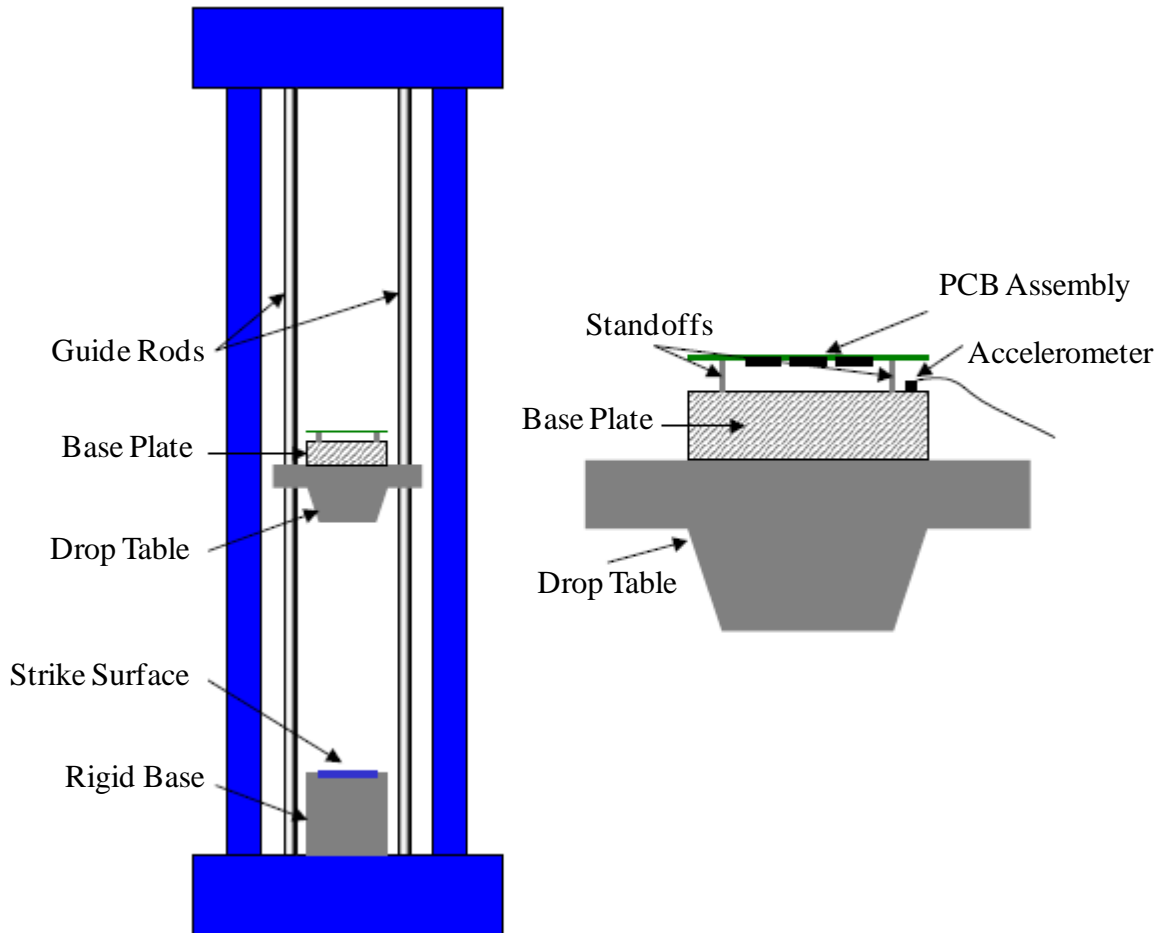


Figure 2.1: Typical drop test apparatus and mounting scheme for PCB assembly (Source: Board Level Drop Test Method of Components for Handheld Electronic Products JESD22-B111)

## 2.3 High Strain Rate Material Properties Lead-free SAC Solder Alloys

Previously, eutectic or near eutectic tin-lead based solder joints were widely used in the electronics industry because of their ease of solderability and long term reliability under a variety of commonly used environmental conditions. In the recent past, the electronics industry has migrated to leadfree solder alloy compositions or so called "green" products under the ROHS initiative. Tin-Silver- Copper (SnAgCu or SAC) alloys are being widely used as replacements for the standard 63Sn-37Pb eutectic solder. Properties of leadfree solder alloys at strain rates

23

typically experienced by the solder joint during typical mechanical shock events are scarce. Previously, constitutive material behavior of solder has been studied at high strain rates by using Split Hopkinson Pressure Bar test [Jenq 2009, Chan 2009, Siviour 2005] high strain rate impact tester [Wong 2008] dynamic Impact tester [Meier 2010]. Table 2.1 provides the brief survey on material properties of SnAgCu based solder alloys at various strain rates.

Table 2.1 Literature Survey on Lead-free Solder Alloys Material Properties at high Strain Rate [tested at room temperature (20-25$^0$C)]

| Solder Alloys Composition | Specimen Details | Instrument /technique | Strain rate (per sec) | Tension/ Compression (C) | | Author- year |
|---|---|---|---|---|---|---|
| | | | | E (GPa) | UTS (MPa) | |
| Sn3.9Ag0.6Cu | | Pull tester[1] *Acoustic wave*[2] | 0.02 - | 7.5(C) *52* | | Vianco 2005 |
| Sn3Ag0.5Cu | Slow cooled Rapidly cooled | | 0.1 0.1 | | 35 70 | Kim 2002 |
| Sn3Ag0.5Cu | Air cooled | Pull tester | 0.147 | | 50 | Zhu 2007 |
| Sn3Ag0.5Cu | Reflowed solder array | Pull tester | 1 | | 100 | Darveaux 2006 |
| Sn-3.5Ag | | | 1 | | 60 | Plumbridge 1999 |
| Sn3Ag0.5Cu | | Pull tester | 1.2 | | 71.7 | Kaminishi 2004 |
| Sn3Ag0.5Cu | | Drop Impact | 50 | 7 (C) | 130(C) | Wong 2008 |
| SnAg1.3Cu0.5Ni | | Pull tester | 100 | | 22(Yield) | Meier 2010 |
| Sn3Ag0.5Cu | | Split Hopkinson Pressure Bar | 1200 | 33(C) | 162 | Qin 2010 |
| Sn1Ag0.5Cu Sn3Ag0.5Cu | | Split Hopkinson Pressure Bar | 1240 | | 160(C) | Jenq 2009 |
| Sn3.8Ag0.7Cu | Water quench | Split Hopkinson Pressure Bar | 3000 | | 195 (C) | Siviour 2005 |
| Sn1Ag0.5Cu Sn3Ag0.5Cu | - | Ultrasonic stress wave propagation | - | 47 53 | | Suh 2007 |
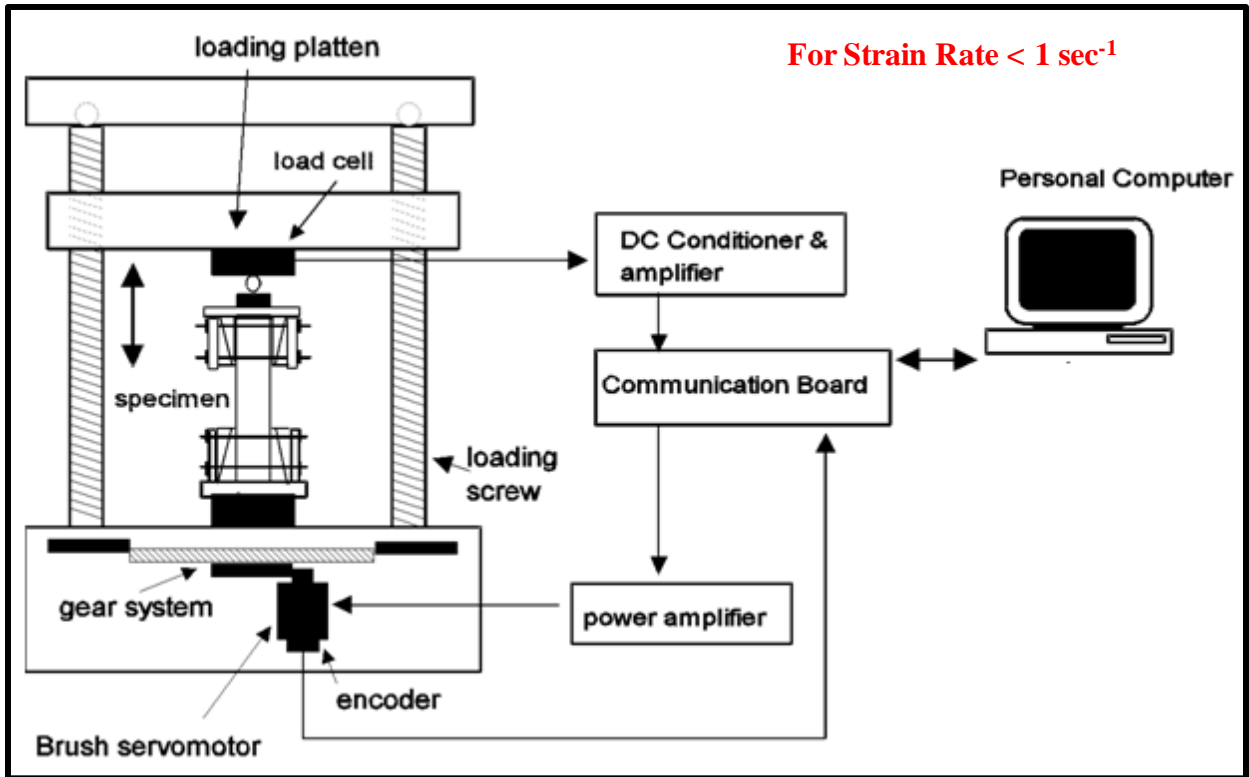
Figure 2.2: Screw driven Tensile Tester Schematic

[source: http://faculty.engineering.asu.edu/cement/research-themes/applications-of-structural-mechanics-to-strain-rate-effects-in-materials-biomechanics-electrical-power-distribution-systems-aerospace-and-structural-steel/retrofit/]
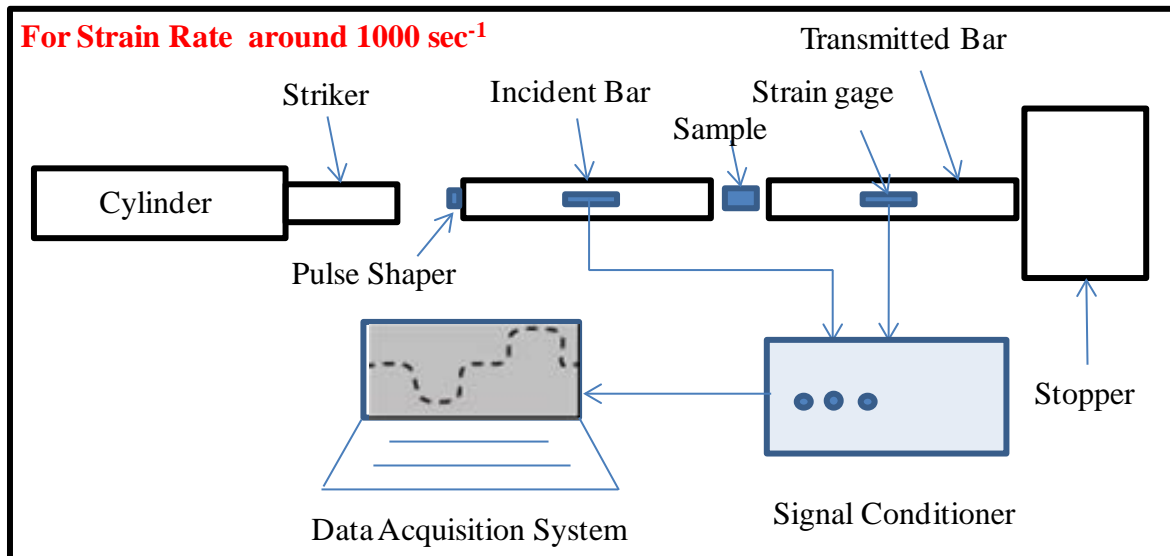


Figure 2.3: Typical Split Hopkinson Pressure Bar for very high strain rate material testing

## 2.4 Aging Effects of Lead-free SAC Alloys

Previously, authors have studied the microstructure, mechanical response and failure behavior of leadfree solder alloys when subjected to elevated isothermal aging and/or thermal cycling [Ding 2007, Hsuan 2007, Darveaux 2005, Pang 2004, Xiao 2004] and also effects of room temperature aging on lead-free solder alloys properties [Zhang 2009, Darveaux 2005, Pang 2004, Chuang 2002, Lee 2002, Tsui 2002, Coyle 2000] at low strain rate events (<1 per sec). But the high strain rate properties of leadfree alloys at elevated isothermal aging and room temperature aging are scarce.

Previously, author Zhang [2009] had done extensive work on the aging behavior of SAC series including SAC105, SAC205, SAC305 and SAC405 solder alloys at low strain rates (0.001 sec$^{-1}$). Mechanical properties of SAC alloys decreases with aging time and temperature. Also, high silver content SAC alloys had better aging resistance (Figure 2.4 to Figure 2.7).
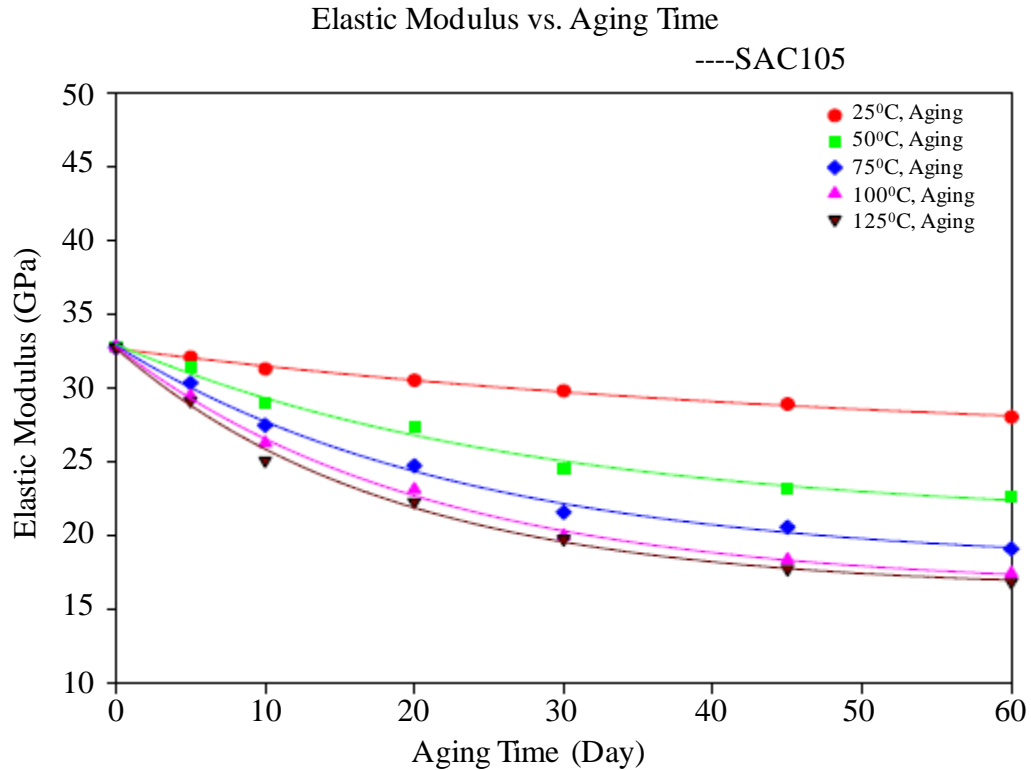


Figure 2.4: Elastic modulus of SAC105 with aging at strain rate 0.001 sec$^{-1}$ (Zhang 2009)
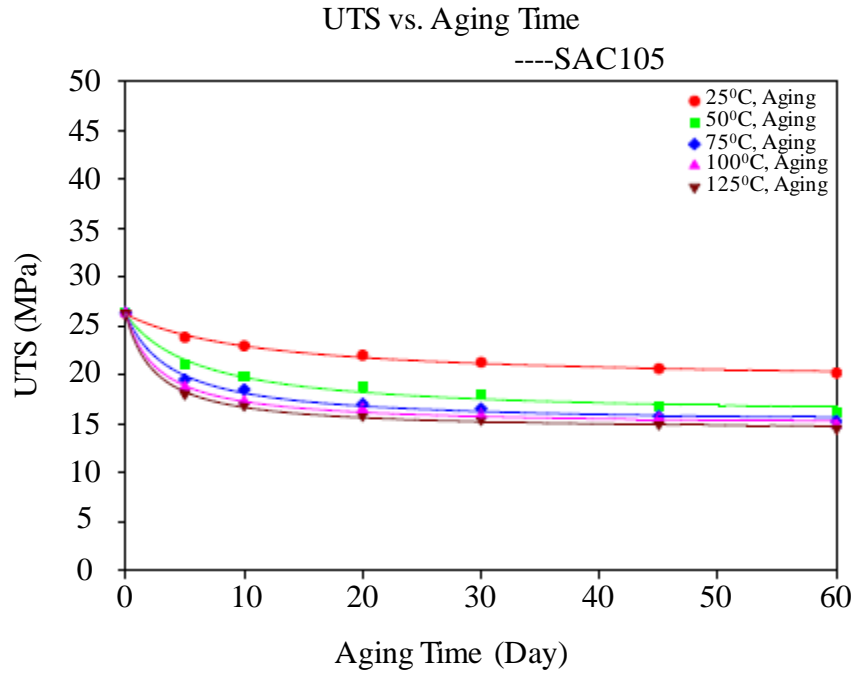
Figure 2.5: Change of UTS of SAC105 with aging at strain rate 0.001 sec$^{-1}$ (Zhang 2009)
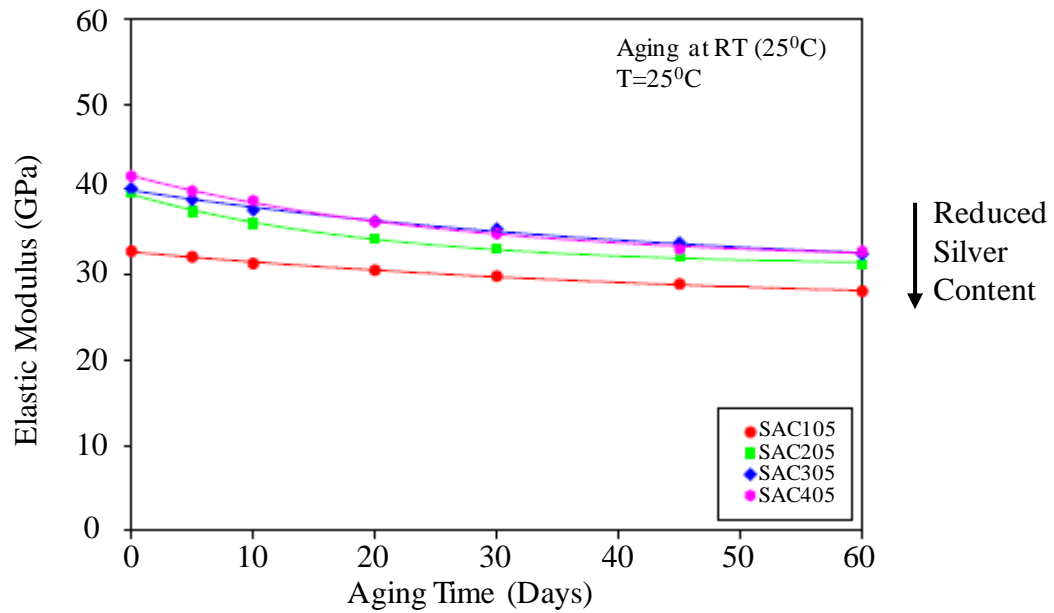


Figure 2.6: Effect of silver content in SAC alloys on the evolution of elastic modulus with aging at strain rate 0.001 sec$^{-1}$ (Zhang 2009)
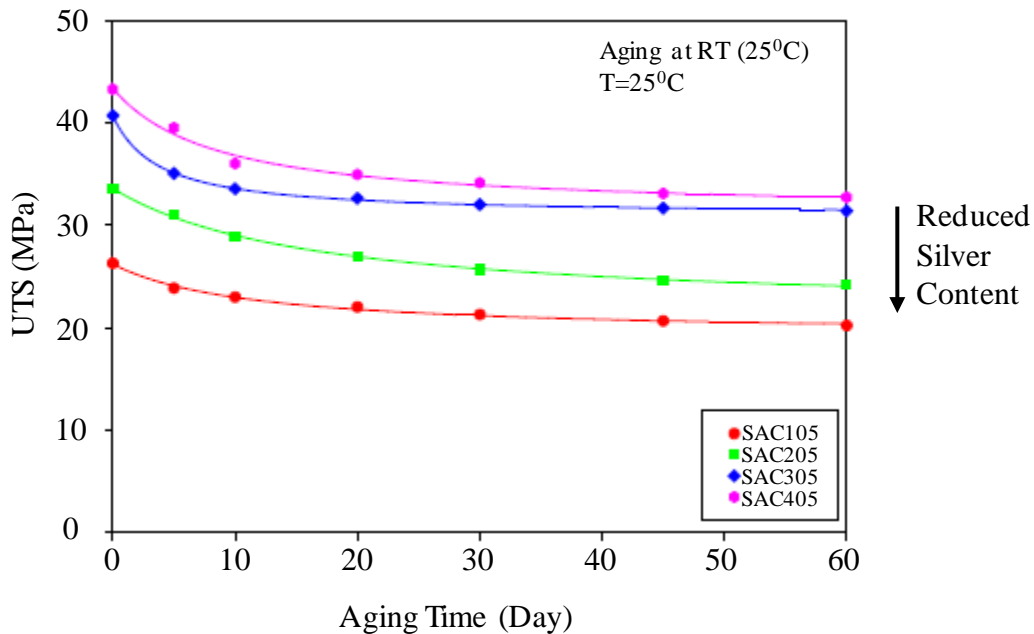
Figure 2.7: Effect of silver content in SAC alloys on the evolution of UTS with aging at strain rate 0.001 sec$^{-1}$ (Zhang 2009)

Author Zhang claims that the microstructure coarsening to be the fundamental reason behind the mechanical property deterioration of solder alloys. Due to aging, grain size and phase structure increases leading to the reduction of tensile strength because coarsened grain and second phase particle lose their effectiveness in blocking dislocation movement due to lesser grain boundaries and weaker precipitation pinning effect in SAC alloys [Zhang 2009].

## 2.5 Constitutive Models for Tensile Data of SAC solder Alloys

Mechanical properties of solder alloys are required for the application of numerical approach such as finite element method to various aspects of electronic packaging. Uniaxial tensile test based measured data are used to develop constitutive models to describe force-displacement and stress-strain responses and the corresponding material properties and failure thresholds.

Ramberg Osgood's model [Ramberg 1943] can be used to describe non-linear relationship between stress-strain. This mathematical model is suitable for SAC alloys which harden with plastic deformation (strain hardening) showing smooth transition in the elastic-plastic region in stress-strain curve.

$$\varepsilon = \left[\frac{\sigma}{E}\right]_{ElasticStrain} + \left[K\left(\frac{\sigma}{E}\right)^n\right]_{PlasticStrain}$$

(2.1)

Where:

$\varepsilon =$ Strain along the axial direction

$\sigma =$ Stress along the axial direction

$E =$ Elastic modulus

$K$ and $n =$ material constant or shape parameter.

Empirical mathematical model [Zhang 2009] to fit truncated stress-strain curves. In this model, it consists of two functions: a Hooke's Law linear model used for extremely small strains ($\epsilon \ll 0.0001$), and four parameter empirical representation called Weibull model for larger strains.

$$\sigma(\varepsilon) = E\varepsilon \qquad\qquad \varepsilon \leq \varepsilon^*$$

(2.2)

$$\sigma(\varepsilon) = C_0 - C_1 e^{-C_2 \varepsilon^{C_3}} \qquad \varepsilon \geq \varepsilon^*$$

(2.3)

Where $E$ is the initial elastic modulus; $C_0$, $C_1$, $C_2$, $C_3$ are fitting constant to be determined and $\epsilon^*$ is the strain level where these 2 functions intersect. Also, $C_0 =$ UTS.

Another empirical [Cai 2012] model involves 4 parameter dual hyperbolic tangent model which captures elastic and plastic region.

$$\sigma(\varepsilon) = C_1 \tanh(C_2\varepsilon) + C_3 \tanh(C_4\varepsilon)$$

(2.4)

Where,

$C_1$, $C_2$, $C_3$, $C_4$ are the material constants to be determined. For this model, when considering extreme small strain situation the effective modulus (E) = $C_1$ $C_2$ + $C_3$ $C_4$. When considering large strain, the ultimate tensile strength (UTS) = $C_1$ + $C_3$.

## 2.6 Digital Image Correlation Application for Drop/Shock

The Digital Image Correlation (DIC) method involves in tracking of geometric points before and after deformation on the region of interest coated with random speckle patterns that enables full field displacement and their derivatives measurement. Previous studies have shown that the size, consistency and density of the speckle pattern affect the accuracy of the method [Zhou 2001, Amondio 2003, Srinivasan 2005]. DIC is method is preferred over strain gage which measure strain only at discrete location on the test specimen. This method is also advantageous because it has reduced sample preparation time and lower costs.

The DIC has been extensively used in the electronic industry for wide range of applications. This method has become popular in the thermal area of electronic packaging and it is fairly new in the field of drop and shock. Previously, various authors have used DIC method to measure full-field displacement and their gradients in electronic assemblies subjected to drop and shock [Lall 2007[b], 2008[a,b], Miller 2007, Park 2007a,b, 2008], [Scheijgrond 2005] measurement of velocity, rotation, bending on portable products subjected to shock test. Damping ratio on the surface of the board [Peterson 2008].

## 2.7 Finite Element Analysis (FEA) for Drop/Shock Tests

During a drop/shock event, it is very difficult to measure displacement and their gradients across the board-joint interface using experimental techniques such as strain gages. Previously,

researchers have investigated the transient dynamic behavior of boards and product levels using various simulation approaches. Prediction of board transient dynamic behavior using smeared property models [Lall 2004, 2005], Conventional shell with Timoshenko-beam Element Model and the Continuum Shell with Timoshenko-Beam Element Model [Lall 2006a,b, 2007a-e, 2008ad], using equivalent layer models [Gu 2005], Implicit transient analysis with Input-G Method [Luan 2004]. [Yeh 2004] used an implicit solver by translating the input acceleration pulse into effective support excitation load on the test vehicle. Implicit global models [Irving 2004, Pitaressi 2004], and global-local sub-models [Tee 2003, Wong 2003, Zhu 2001, 2003, 2004]. Application of FEA for drop/shock event with crack growth is highly challenging.

### 2.7.1   Crack Growth in Finite Element Analysis

Conventional finite element analysis does not support crack propagation in the model. The governing equations in numerical approach such as FEA are partial differential equations which is incompatible to solve cracks. The spatial derivative needed for these partial differential equations to make sense does not exist on crack tip or surface. There are few approaches available in commercial platforms to simulate crack growth in FEA such as Stress Intensity Factor (SIF) based upon fracture mechanics (FM), extended finite element method (X-FEM) by Belytschko and Cohesive Zone Modeling approach (CZM).

*Fracture mechanics approach:* This method involves in the estimation of stress intensity factor near the crack tip. Three distinct modes of crack propagation exist as shown in Figure 2.8. A tensile stress field gives rise to mode-1, the opening crack propagation mode which is the most dominant crack mode across the solder joint and PCB interface during drop test.
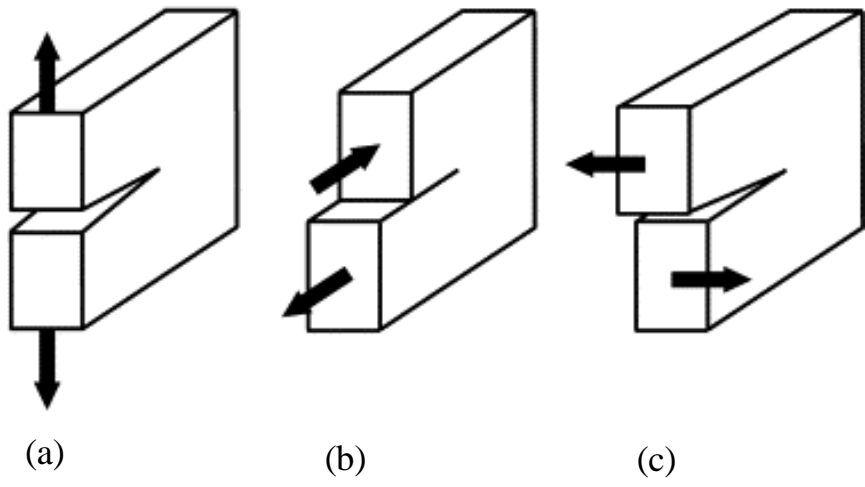
Figure 2.8: The three modes of crack propagation (a) Opening mode (b) Sliding mode (c) Tearing mode
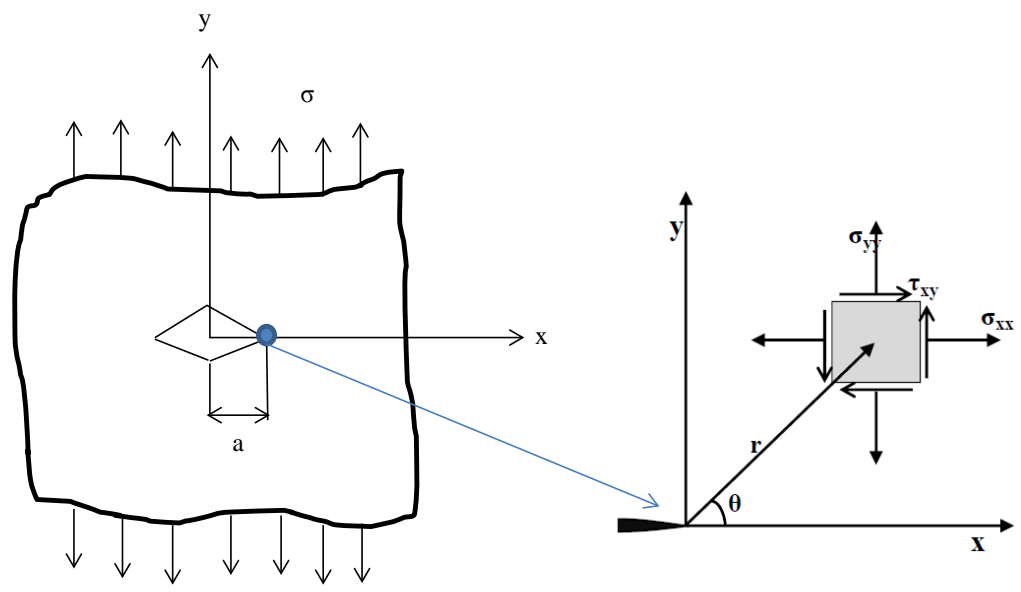


Figure 2.9: Mode 1 Crack Model

For the plate shown in Figure 2.9, stress intensity factor is given by,

$$K_I = \sigma \sqrt{\pi a}$$

(2.5)

And the stress field near the crack tip is,

$$\sigma_{xx} = \frac{K_I}{\sqrt{2\pi r}} \cos\left(\frac{\theta}{2}\right)\left[1 - \sin\left(\frac{\theta}{2}\right)\sin\left(\frac{3\theta}{2}\right)\right]$$

(2.6)

$$\sigma_{yy} = \frac{K_I}{\sqrt{2\pi r}} \cos\left(\frac{\theta}{2}\right)\left[1 + \sin\left(\frac{\theta}{2}\right)\sin\left(\frac{3\theta}{2}\right)\right]$$

(2.7)

$$\tau_{xy} = \frac{K_I}{\sqrt{2\pi r}} \cos\left(\frac{\theta}{2}\right)\sin\left(\frac{\theta}{2}\right)\sin\left(\frac{3\theta}{2}\right)$$

(2.8)

Failure occurs when $K_I = K_{IC}$. In this case, $K_I$ is the driving force for fracture and $K_{IC}$ is a measure of material resistance. Previously, SIF approaches has been implemented to solve crack growth problem in drop/shock events [Xu 2008, Suh 2007].

*Cohesive Zone Modeling (CZM) approach:* This method is primarily intended for bonded interfaces where the interface thickness is negligibly small. In such cases it may be straightforward to express the constitutive response of the cohesive layer directly in terms of traction versus separation. If the interface layer has a finite thickness and macroscopic properties (such as stiffness and strength) of the interface layer material are available, then it may be more appropriate to model the response using conventional material models [Abaqus2009[a]]. Previously, authors have used cohesive zone models to study the failure across solder joint interface in drop/shock events [Lall 2007[e], 2009].

*Extended Finite Element Method (X-FEM):* This method was originally introduced by Belytschko and Black to solve the problems associated with crack growth with minimum

33

remeshing [Belytschko 1999]. In this method, a discontinuous enrichment function has been added to the standard approximation function using partition of unity. In XFEM, cracks can propagate along arbitrary solution dependent path with no requirement for mesh topology [Abaqus2009[b]]. The near tip asymptotic singularity is not needed but only the displacement jump across a cracked element is considered. Previously, authors have implemented XFEM approach to simulate crack in the drop/shock event of portable electronics [Lall 2010, Cadge 2011].

# Chapter 3

## Effect of High Strain-Rate on Mechanical Properties of SAC Lead-free Alloys

### 3.1 Overview

Electronics may experience high strain rates when subjected to high g-loads of shock and vibration. Material and damage behavior of electronic materials at high strain rates typical of shock and vibration is scarce. Previously studies have shown that second-level interconnects have a high propensity for failure under shock and vibration loads in fine pitch electronics. Exposure to shock and vibration is common in a variety of consumer environments such as automotive and portable electronics. The low strain-rate properties of commonly used SnAgCu solders, including Sn1Ag0.5Cu and Sn3Ag0.5Cu, have been found to evolve with time after prolonged exposure to high temperatures. High strain rate properties of lead-free solder alloys in the strain-rate range of 1-100 sec$^{-1}$ are scarce.

Previous attempts at characterizing the high strain rates properties have focused on the use of the Split Hopkinson Pressure Bar (SHPB), which enables measurements of strain rates in the neighborhood of 1000 per sec. In this chapter, a new test-technique developed by the author has been presented for measurement of material constitutive behavior. The instrument enables attaining strain rates in the neighborhood of 1 to 100 per sec. An impact hammer has been used in conjunction with digital image correlation (DIC) and high-speed video for measurement of material constitutive behavior of lead-free SAC alloys in the strain rate range of 1-100sec$^{-1}$.

Thin-bar samples have been fabricated by reflowing solder in glass tubes using reflow profiles typical of lead-free assemblies. Bar sample thickness has been selected to be in the neighborhood of typical heights of solder interconnects in fine-pitch electronics. Tests are conducted at strain rates 10, 35, 50 and 75 per sec. High speed cameras operating at 75,000 fps have been used in conjunction with digital image correlation for the measurement of full-field strain during the test. Constancy of cross-head velocity has been demonstrated during the test from the unloaded state to the specimen failure. SAC105 and SAC305 specimen have been subjected to various lengths of aging temperatures, aging times (0-2 months) and strain rates. Rate independent material AL7075-T6 has been used as a bench mark experiments at various strain rates in the range of 1-100 per sec. Solder alloy constitutive behavior has been measured for SAC105, SAC305 solders. The experimental data has been fit to the Non-linear Ramberg-Osgood model which is available in Abaqus. The model has been used to predict the time independent solder specimen behavior subjected to high strain rate tensile test. Non-linear Ramberg-Osgood model's parameters for the solder alloys were extracted from experimentation and implemented in the finite element analysis for full-field strain correlation between DIC and simulation.

## 3.2 Specimen Preparation Set-Up

Figure 3.1 shows specimen preparation setup where solder test specimens were formed in high precision rectangular cross section glass tubes using a vacuum suction process. The solder specimens were first melted in quartz crucible using a solder pot maintained around $240^0$C. One end of the high precision glass tube is placed inside the rubber tube connected to suction pump. The other end is inserted into the quartz crucible. The molten solder rises in the glass tube by suction pressure applied from the pump. The suction force is regulated through a control knob on the vacuum line so that only a desired amount of solder is drawn into the tube. The glass tube has

then been removed from the crucible and water quenching is employed to cool the specimen and they are then sent through a reflow oven to re-melt the solder in the tube by subjecting it to the user defined temperature profile. Thermocouples are attached to the glass tubes and monitored continuously using a radio-frequency KIC temperature profiling system to ensure that the samples are formed using the desired temperature profile (same as commercial solder joints). Figure 3.2 illustrates the reflow temperature profile implemented in this work for SAC solder specimens. The final solidified solder samples are removed by gently breaking the glass tubes using vice. The specimens are examined by X-ray imaging to ensure that the sample is free from void, indentation or premature crack in the gage length as shown in Figure 3.3 and Figure 3.4. Uniaxial samples were formed with nominal dimensions of $40\times5\times0.5\text{mm}^3$. The thickness of 0.5mm was chosen to match the height of typical BGA solder balls. Also, for the elevated thermal aging, specimens were stored inside the aging oven immediately after the specimen preparation in order to avoid any possible room temperature aging.
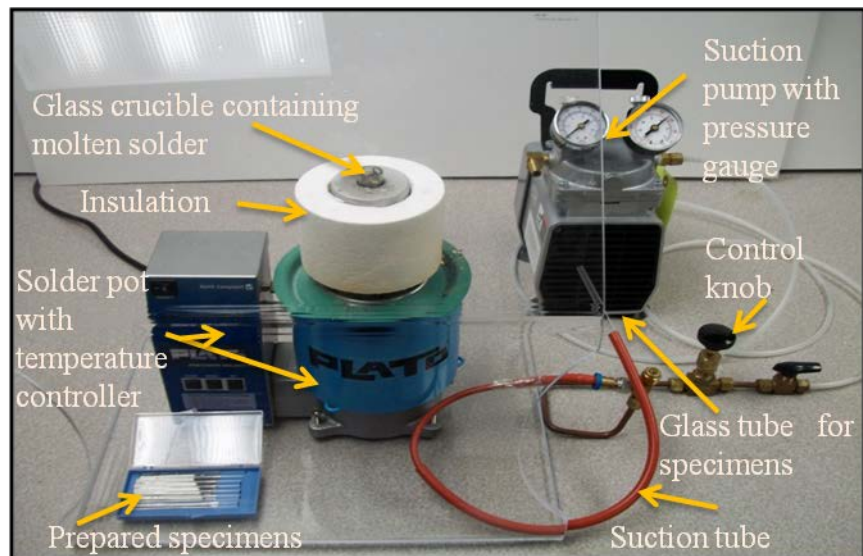


Figure 3.1:  Specimen Preparation Setup

37
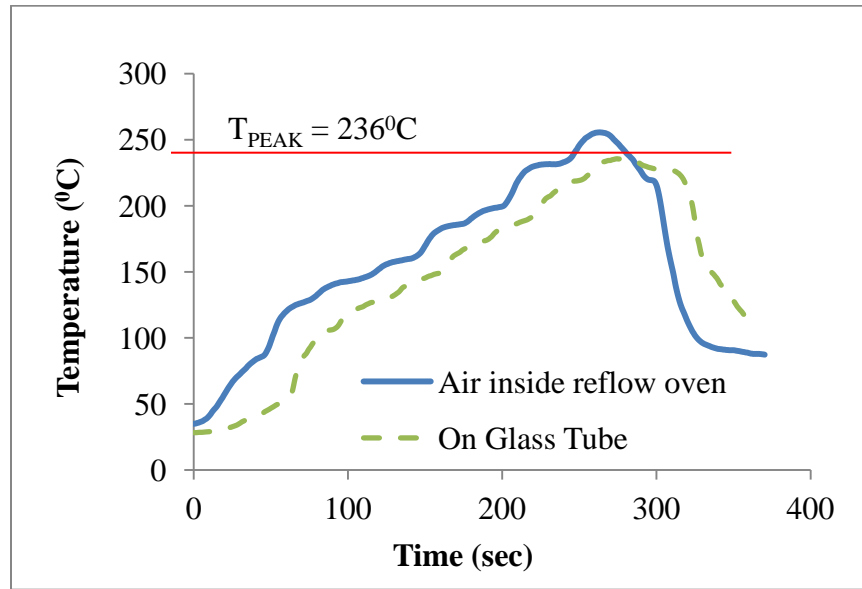
Figure 3.2: Solder Reflow (RF) Temperature Profile (SAC)
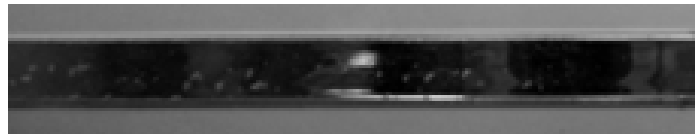


Figure 3.3: Specimen inside glass tube



Figure 3.4: X-ray inspection

## 3.3 Experimental Set-Up

A motion-control impact-hammer has been used to conduct a high-strain rate test at high velocity. Slip-joint has been incorporated in the load train to allow the cross-head to attain a constant high-velocity prior to loading the specimen. The load frame incorporates a piezoelectric load-cell and a linear voltage displacement transducer. In addition, the specimen is speckle coated and deformation captured with two high-speed video cameras. The force data is captured with high-speed data acquisition system at 5 million samples per sec. The crosshead deformation history has been captured with image tracking software for computation of cross-head displacement and cross-head velocity. The high mass of the impact hammer along with the slip-joint enables the cross-head to maintain a constant high velocity during the entire pull-test. The constant velocity during the pull testing provides evidence of elimination of the possible inertial effects experienced in high speed pull testers under dynamic loading conditions. The slipjoint enables the cross-head to attain the desired velocity prior to any specimen deformation during the test. At time $t > 0$, the slip-joint undergoes downward direction due to externally applied load. The slip-joint continues to move keeping the specimen stationary till the slip-joint reaches the maximum extended length. The crosshead pulls the specimen at constant velocity after the slip-joint reaches the maximum length and engages the specimen. Figure 3.5 shows the experimental layout from the top view.
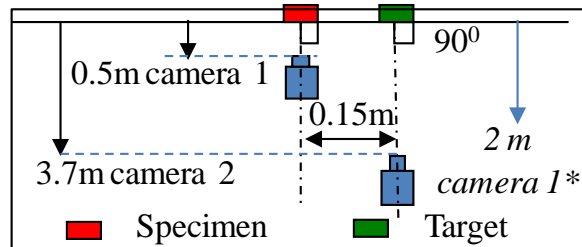


Figure 3.5: Camera configuration for capturing specimen deformation at high strain-rate

**Point A (Fixed)**

**Point B (Moving)**

camera 1 (a)

Datum

0.120m

**Point 1 (Fixed)**

**Point 2 (Moving) Variable weight**

**Contact**

0.89m

**Point 3 (Moving)**

camera 2 (b)

Force sensor

Speckled solder joint

Gauge length 0.040m

Full rod extension 0.0254m

$T_0 = 0$ sec (At rest)

$T_1 > T_0$ (zero specimen elongation up to complete slip joint extension)

$T_2 > T_1$ (specimen pulled at constant high velocity)

View from camera1* (c)
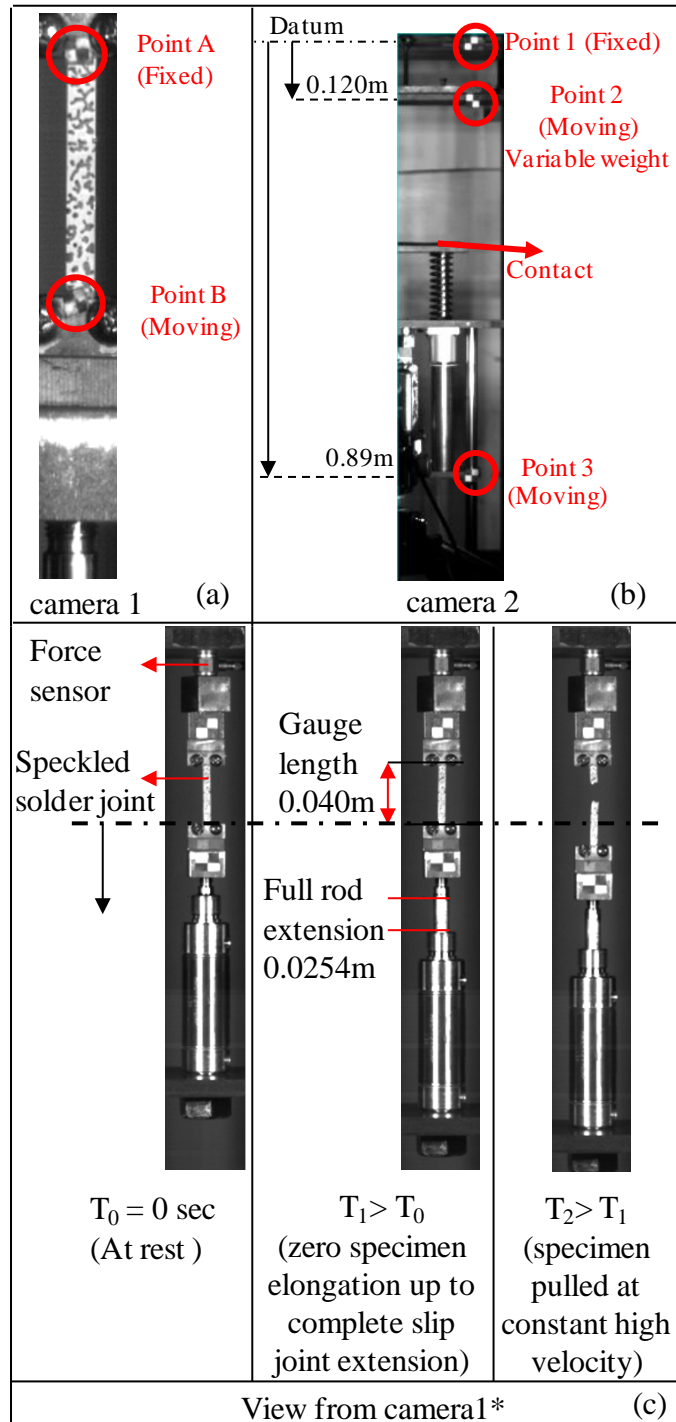
Figure 3.6: (a) High speed camera-1 monitoring cross-head motion. (b) High speed camera-2 monitoring targets. (c) Specimen configuration with a slip joint

40
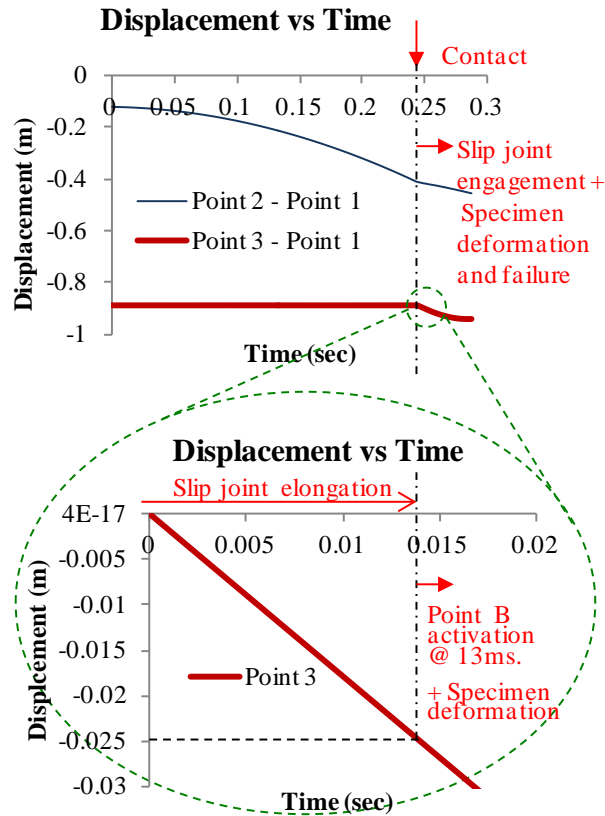
Figure 3.7: Dynamic input loading time-history (Using targets (1, 2, and 3)) *camera 2*
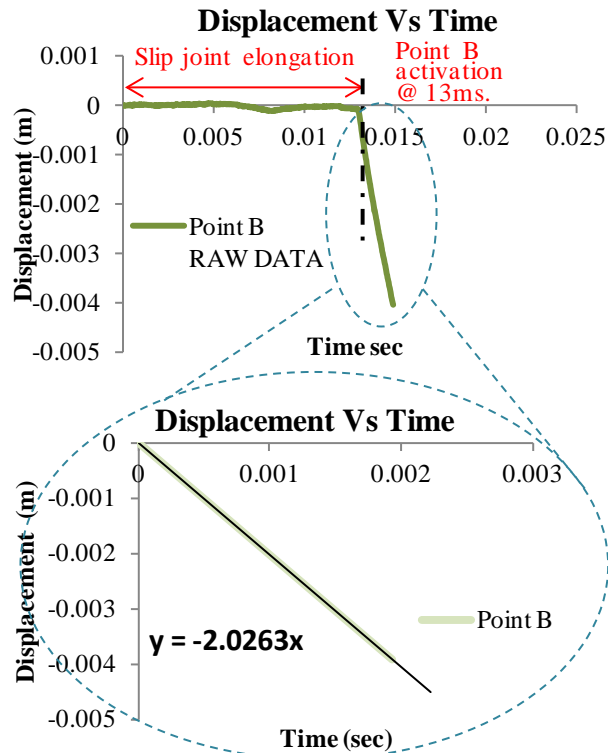


Figure 3.8: Specimen deformation (using targets (A, B)) *camera 1*

41

### 3.3.1 Description of Dynamic Input Loading with Slip-joint to Yield Constant High Velocity Crosshead Motion

Three target locations, termed as points, have been used to monitor the complete tensile testing event. Point 1 is fixed to the test frame and serves as a reference. Point 2 is attached to the impact hammer and point 3 is attached to the bottom crosshead through the slip-joint as shown in Figure 3.6 (b). All the 3 targets are mounted such that they are in the same plane with respect to the lens of the camera 2 (Figure 3.5). The motion of the impact hammer causes the motion of point 2 which in turn causes the motion of point 3 when point 2 reaches the "metal-contact" region. Motion of point 3 causes the motion of the bottom crosshead located at point B (Figure 3.6 (a)) through the slip-joint mechanism.

The initial 0.005m displacement of the cross head at point B is considered for strain and strain rate computation since all the specimens have shown almost or complete failure within this range. Figure 3.7 shows the relative motion of point 2 and point 3 with respect to point 1 for complete pull test event. Also, Figure 3.7 in green circled region shows the time at when specimen starts elongating after when point 3 crosses 0.0254m or 1 inch (rigid body motion) due to slip joint engagement. Figure 3.8 top plot shows the relative motion of point B (bottom crosshead) with respect to point A (top cross head). Figure 3.8 bottom plot shows the displacement as a function of time during specimen deformation. It should be noted that from both the figures (Figure 3.7 and Figure 3.8) time at which specimen starts deforming remain consistent. Also, in Figure 3.8, relative displacement of point B with respect to point A is highly linear for the raw data. Therefore, the current experimental setup is suitable to conduct high strain rate (quasi-static) material testing.

**Input mass = 14.061kg**
**Drop height = 0.296m**
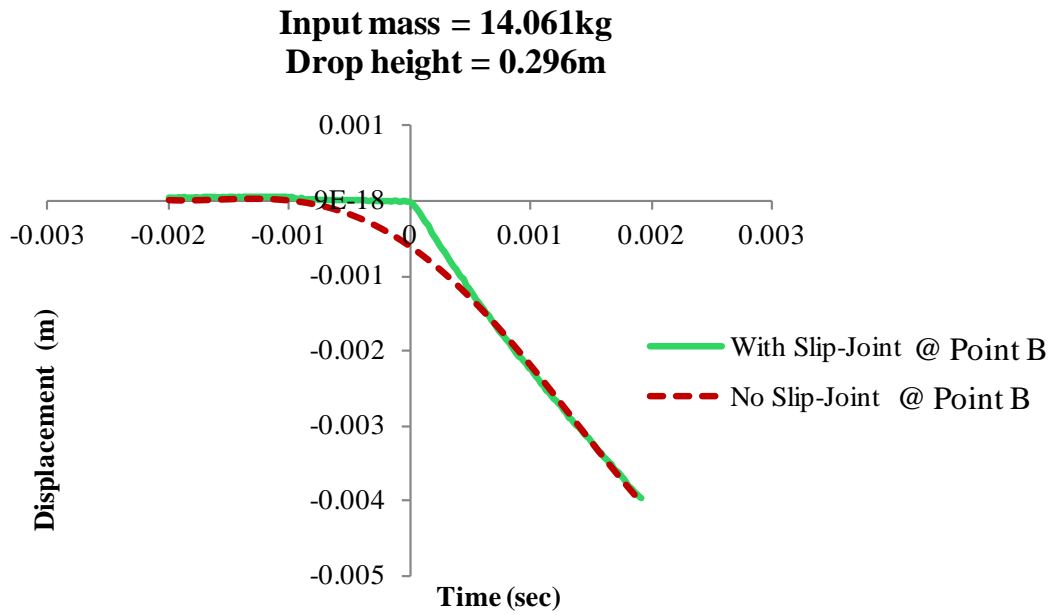


Figure 3.9: Bottom cross head displacement time history with and without slip joint mechanism

## 3.4 Input loading rate repeatability

Random variation in test conditions can produce variations in the measured material response and reduce the accuracy of the measured data. Figure 3.10 (a) and Figure 3.10 (b) shows the measured repeatability of the measured displacement of the impact hammer and the specimen deformation after slip joint engagement for 2 different loading rates.
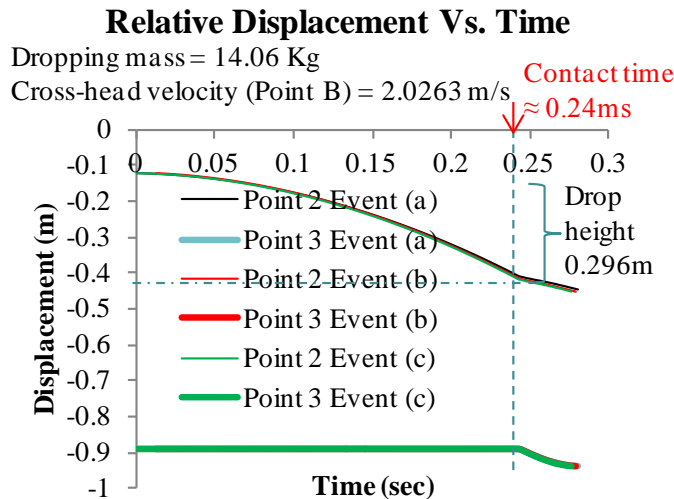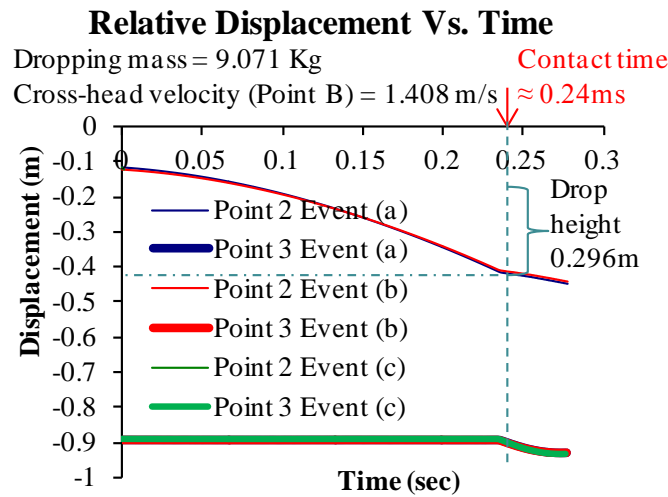




Figure 3.10: (a), (b) Repeatability of the test method

## 3.5 Mathematical Relationship between Relative Cross-head Velocity, Strain-rate and Gage Length

The relationships between strain rate and crosshead velocity can be represented by a straight line (Figure 3.11, Figure 3.12). The slope of the strain rate versus crosshead velocity curve is mathematically represented by:

$$m = \frac{\dot{\varepsilon}}{V} = \frac{1}{L_0} \tag{3.1}$$

Where, m (meter$^{-1}$) is the slope of the strain rate versus cross-head velocity, $\dot{\varepsilon}$ is the specimen strain-rate (sec$^{-1}$), V is the relative cross-head velocity (meter.sec$^{-1}$), and $L_0$ is the gage length (meters)
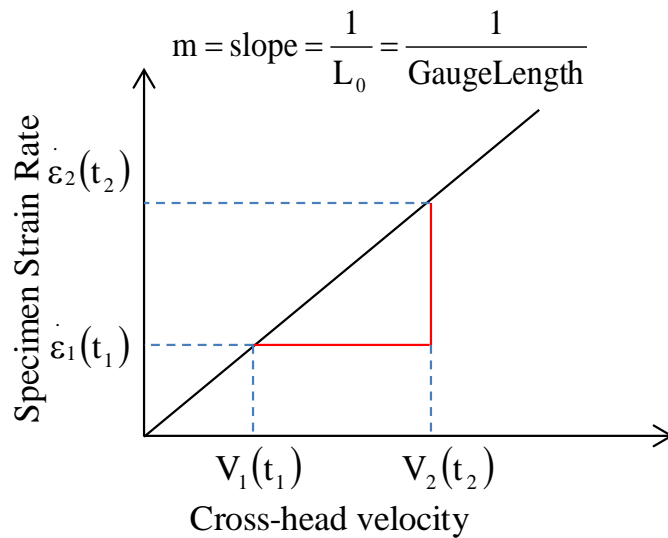


Figure 3.11: Strain-rate as a function of cross-head velocity with inverse of the slope being gage length

45

Equation (3.1) can be represented as follows for deformation measured over two different time-frames of $t_1$ and $t_2$ in which the specimen deformation of $\Delta L_1$ and $\Delta L_2$ is encountered respectively.

$$m = \frac{\dfrac{1}{t_2}\left(\dfrac{\Delta L_2}{L_0}\right) - \dfrac{1}{t_1}\left(\dfrac{\Delta L_1}{L_0}\right)}{\left(\dfrac{\Delta L_2}{t_2}\right) - \left(\dfrac{\Delta L_1}{t_1}\right)} \qquad (3.2)$$

Since the crosshead velocity during specimen deformation is constant, as shown in Figure 3.12, thus

$$\left(\frac{\Delta L_2}{t_2}\right) = \left(\frac{\Delta L_1}{t_1}\right) \qquad (3.3)$$

$$m = \frac{1}{L_0} \qquad (3.4)$$
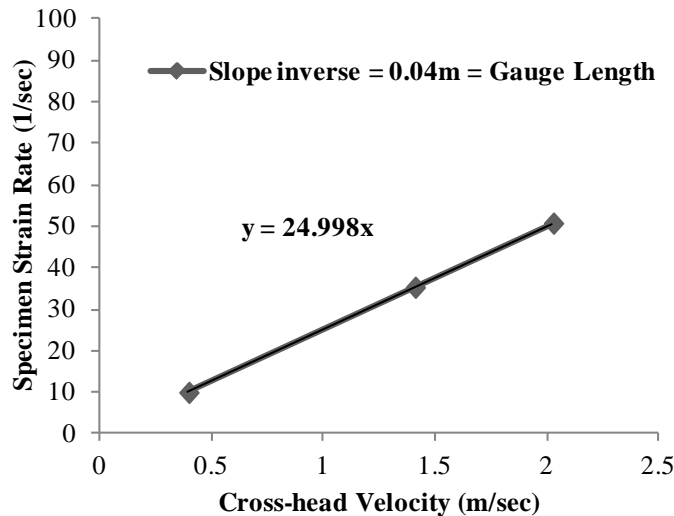


Figure 3.12: Specimen strain rates as a function of relative cross-head velocities tested

Table 3.1: Strain rates Vs cross-head velocities tested

| Gauge Length =0.04m | |
| --- | --- |
| Cross-head velocity (m/s) | Strain Rate (1/sec) |
| 0.395 | 9.88 |
| 1.408 | 35.20 |
| 2.0263 | 50.65 |
| 1.51 (*gauge length 20mm*) | 75.50 |

From equation (3.1), specimen strain-rate and the cross-head velocity are linearly related for the uniaxial tensile test. Thus, one can measure the strain rate experienced by the specimen if the gauge length of the specimen is known along with the corresponding cross-head velocity. Above equation eliminates the usage of strain gage or other strain measuring techniques to monitor the strain rate during specimen deformation. It should be noted that strain rate remain identical at all the location within the specimen gage length up to the onset of necking and additional displacements will be localized in necked regions. Also, for the practical application, one should also consider the Saint Venant's principle i.e., strain rate distribution will be same throughout the gage length sufficiently removed from the point of load application.

### 3.6 Hooke's Law to Represent the Elastic Portion of the High Strain Rate Deformation

From Hooke's Law, stress and strain are linearly related as follows:

$$\sigma = E\varepsilon \tag{3.5}$$

$$\frac{P}{A_0} = E\left(\frac{\Delta x}{L_0}\right) \tag{3.6}$$

$$\left(\frac{P}{\Delta t}\right)\cdot\frac{1}{A_0} = \frac{E}{L_0}\cdot\left(\frac{\Delta x}{\Delta t}\right) \tag{3.7}$$

Where $\Delta x$ is the specimen deformation, E is the elastic modulus, $\Delta t$ is the time of deformation, P is the force applied on the specimen, and $A_o$ is the original cross-sectional area of the specimen.

$$\left(\frac{\dot{P}}{A_0}\right) = E\cdot\left(\frac{V}{L_0}\right) \tag{3.8}$$

The elastic modulus is then calculated from the following relationship:

$$E = \frac{\dot{P}L_0}{A_0 V} \tag{3.9}$$

The gage length and initial cross-sectional area are known at beginning of the test. The crosshead velocity and the load rate are measured during the test.

$$\dot{\varepsilon} = \frac{V}{L_0} \tag{3.10}$$

$$\dot{\sigma} = \frac{d(\sigma)}{dt} = \frac{1}{A_0}\frac{d(P)}{dt} \tag{3.11}$$

$$E = \frac{\dot{\sigma}}{\dot{\varepsilon}} \tag{3.12}$$

**3.7 Benchmark Experiment**

AL7075-T6 alloy (mainly Al composition, 5 to 6% Zn, 2 to 2.5% Mg, 1.2 to 1.6% Cu and <0.5% others) is a strain rate independent material over a wide range of strain rates (0.03 to 560 per sec) [Meyer 1994]. Elastic modulus of this material is approximately 71.7GPa. In the current work, AL7075-T6 has been used as the bench mark experiment in order to validate the test-setup. Tests were conducted at four different strain rates (within 1-100 per sec). AL7075-T6 specimen dimension used is a shown in Figure 3.13. Figure 3.14 shows typical measured raw data of force-time with foot correction. For the high strain-rate based stress-strain data for both Aluminum and SAC solder alloys, the force (also displacement) zero has been corrected by extending the initial straight portion of force-time curve to zero load and measuring load from that point. This foot correction is commonly employed in tensile testing data [Han 1992]. Dynamic input loading mass and the corresponding drop height for 3 different constant high strain rate cases have been provided in Table 3.2. For all four s train rate cases tested AL7075-T6 specimens responding accurately i.e. the elastic modulus for these 4 cases were close to the actual elastic modulus of the same material (Figure 3.15).
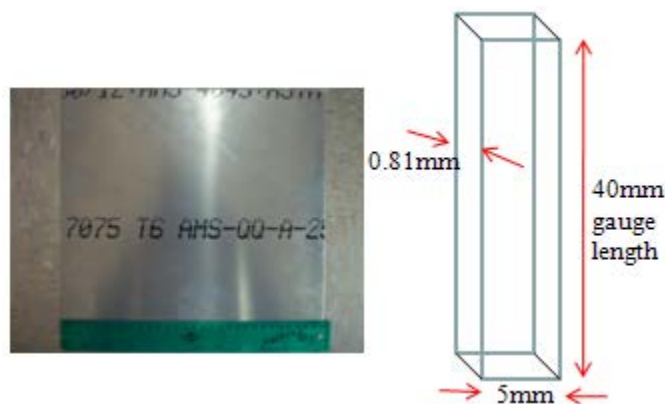


Figure 3.13: Benchmark problem using AL7075-T6 material
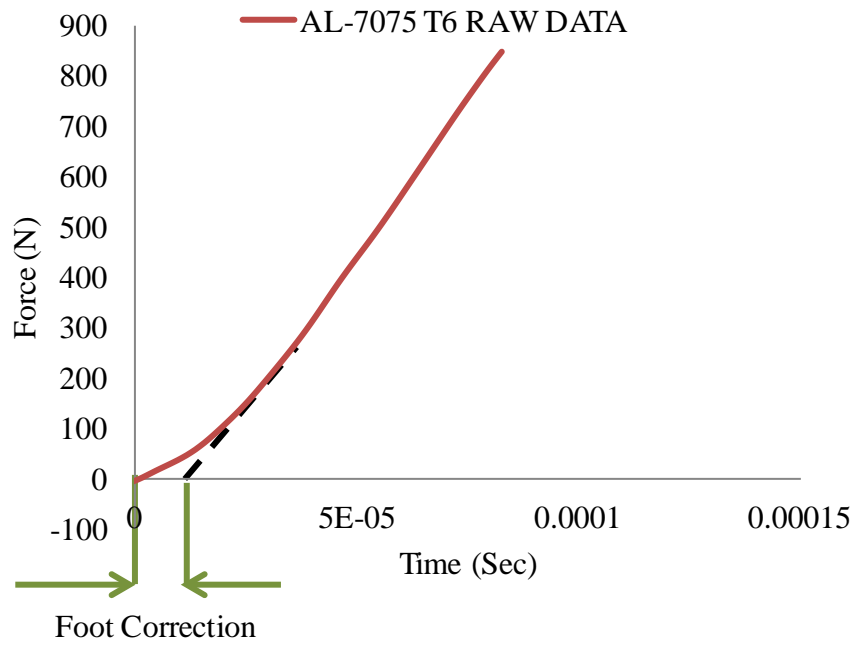
(a)
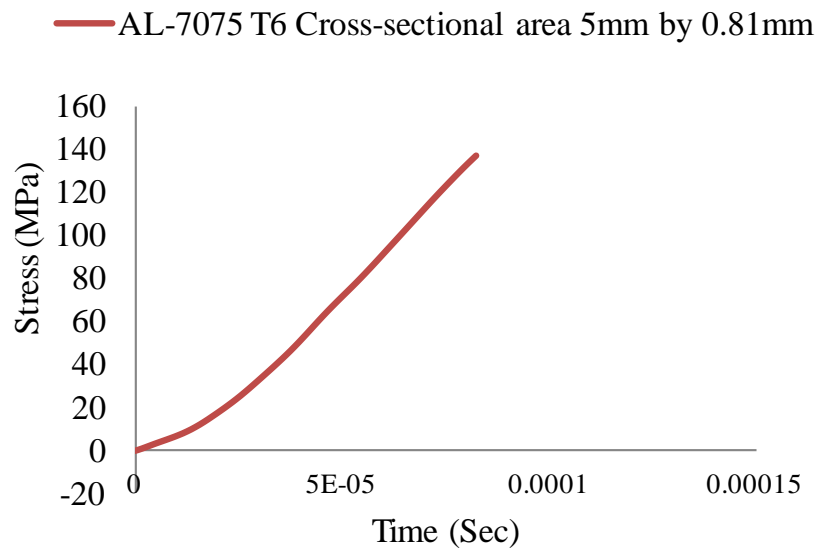


(b)

Figure 3.14: (a) Force-Time demonstrating the foot correction (b) corresponding Stress-Time
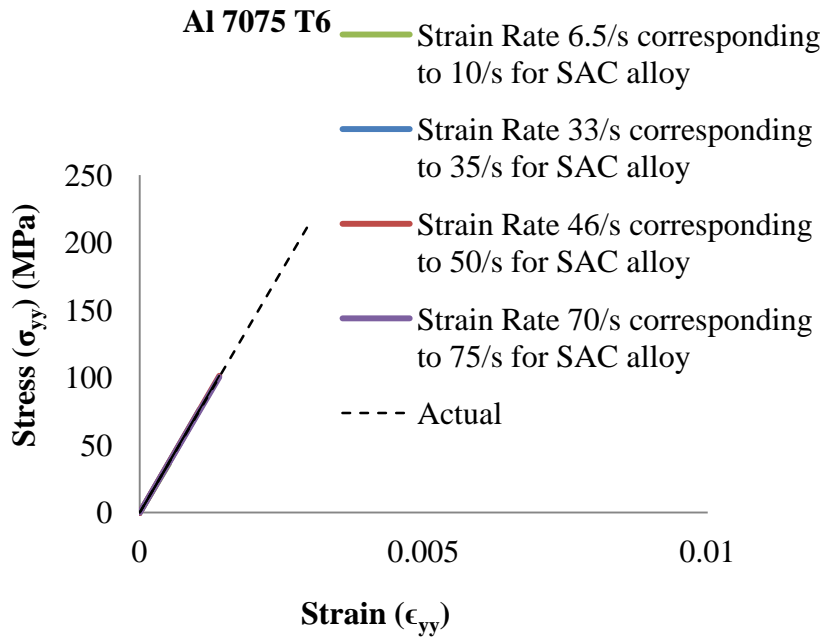
Figure 3.15: Stress-strain behavior of AL7075-T6 within the elastic limit for strain rate between 1 to 100 $sec^{-1}$

Table 3.2: Test cases

| Hammer Mass (Kg) | Drop Height (m) | $\dot{\varepsilon}_{AL}$ (per sec) | $\dot{\varepsilon}_{SAC}$ (per sec) |
|---|---|---|---|
| 11.340 | 0.110 | 6.5 | 9.88 |
| 9.071 | 0.296 | 33.0 | 35.20 |
| 14.061 | 0.296 | 46.0 | 50.65 |
| 13.607<br><br>*Two additional Bungee loops added to set Gauge length 20mm.* | 0.296 | 70.0 | 75.50 |

## 3.8    High Strain Rate Material Data

Uniaxial specimen 40mm long, 5mm wide, and 0.5mm thick were formed for the SAC solder alloys using the methods described earlier in the paper. The samples were aged at temperatures of T = 25°C, 50°C, 75°C, 100°C and  125°C for periods of 1 day, 30 days and 60 days. Reflow profile of the solder specimen were kept similar to actual solder interconnects and the sample thickness chosen to be similar to the height of typical solder joint, with similar microstructure in each planar cross-section. Specimens for each alloy were prepared in batches followed by subjecting them to a specific set of aging conditions (aging temperature and aging time) and high strain-rate test. The procedure was followed to reduce variability in aging conditions due to wait time after completion of specimen formation, aging and prior to high strain rate test. Data measured from multiple samples was then averaged to obtain the nominal material response at the test condition.

Table 3.3 provides the aging test matrix for the stress-strain tests. Figure 3.17 shows the typical high strain rate stress-strain data for SAC lead-free solder alloys. Time to failure (time for complete specimen rupture) can be accurately measured using high speed cameras since the force data is a continuous signal captured using high speed data acquisition system. Figure 3.18 to Figure 3.32 shows the stress strain plot for 1-day aged at 25C, 1-day aged at 50C, 1-day aged at 75C, 1-day aged at 100C, 1-day aged at 125C,  30 days aged at 25C, 30 days aged at 50C, 30 days aged at 75C, 30 days aged at 100C, 30 days aged at 125C, 60 days aged at 25C, 60 days aged at 50C, 60 days aged at 75C, 60 days aged at 100C, and 60 days aged at 125C respectively for both SAC105 and SAC305 specimens at 4 different strain rates (1-100 per sec).  Table 3.5 to Table 3.34 shows numerical values of the elastic modulus and ultimate tensile strength (UTS) for each of the tested cases.  Pristine samples exhibit a higher elastic modulus and ultimate tensile

strength compared to the elevated temperature aged samples in each case. Samples exposed to 60

days of isothermal aging exhibited the lowest elastic modulus and ultimate tensile strength of all

the cases tested. Also, special case where rate of cooling effects (reflowed Vs water quench) on

material properties of SAC Alloys were determined for1 Day Aging at 25C.

Table 3.3: Aging Test Matrix for the Stress-Strain Tests

| Aging (days) | Aging Temperatures | |
|---|---|---|
| | $25^0$C, $50^0$C, $75^0$C, $100^0$C, $125^0$C | |
| | SAC105 | SAC305 |
| 1 | X | X |
| 30 | X | X |
| 60 | X | X |
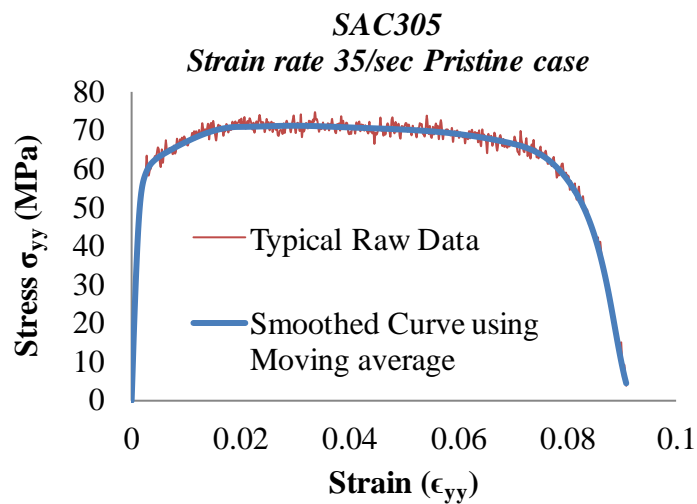


Figure 3.16: Typical raw stress-strain curve for high strain rate test case and corresponding smoothed curve using moving average method
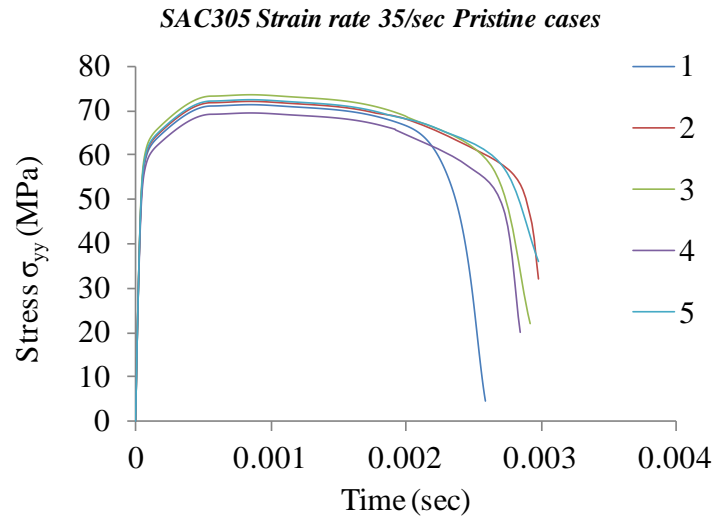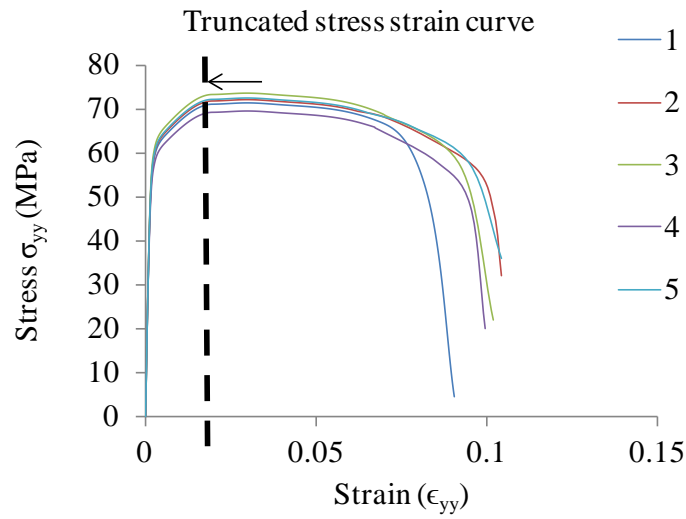
Figure 3.17: (a) Typical high strain rate stress-strain data set for SAC alloys and (b) the corresponding stress-time data set

Table 3.4 Pristine SAC305 strain rate 35 sec$^{-1}$ data set with corresponding average and standard deviation values

| Case | E (GPa) | UTS (MPa) | Standard deviation (S) |
|---|---|---|---|
| 1 | 42.10 | 70.50 | |
| 2 | 41.65 | 71.10 | $s = \left( \dfrac{1}{n-1} \sum\limits_{i=1}^{n} (x_i - \bar{x})^2 \right)^{\frac{1}{2}}$ |
| 3 | 42.50 | 73.10 | |
| 4 | 42.05 | 68.60 | Where, $\bar{x} = \dfrac{1}{n} \sum\limits_{i=1}^{n} x_i$ |
| 5 | 42.15 | 71.70 | |
| **Average** | **42.09** | **71.00** | |
| Standard deviation | **0.303** | **1.652** | |

### 3.8.1 Strain Rate Effects on High Strain Rate Data of SAC Solder Alloys
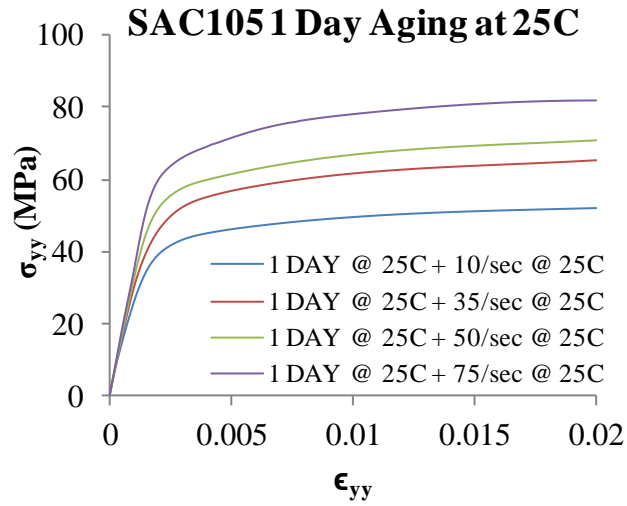


(a)
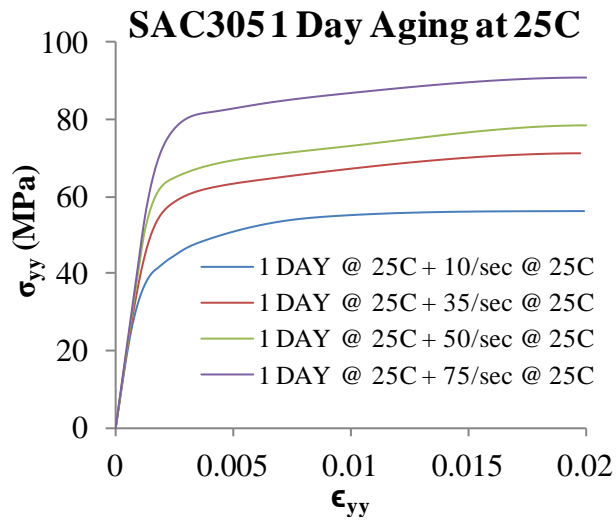


(b)

Figure 3.18: (a), (b) Stress vs. Strain for 1-day room temperature (25C) aged SAC105 and SAC305 alloys respectively

Table 3.5: Material properties of SAC105 1DAY (RF) at $25^0$C

| Strain Rate (per sec) | E (GPa) | UTS (MPa) |
|---|---|---|
| 10 | 32.50 | 52.00 |
| 35 | 33.70 | 65.20 |
| 50 | 34.20 | 71.00 |
| 75 | 36.00 | 81.80 |

Table 3.6: Material properties of SAC305 1DAY (RF) at $25^0$C

| Strain Rate (per sec) | E (GPa) | UTS (MPa) |
|---|---|---|
| 10 | 40.20 | 55.90 |
| 35 | 42.09 | 71.00 |
| 50 | 43.06 | 78.30 |
| 75 | 45.00 | 91.00 |

Figure 3.19: (a), (b) Stress vs. Strain for 1-day elevated temperature (50C) aged SAC105 and SAC305 alloys respectively

Table 3.7: Material properties of SAC105 1DAY (RF) at $50^0$C

| Strain Rate (per sec) | E (GPa) | UTS (MPa) |
|---|---|---|
| 10 | 32.00 | 50.00 |
| 35 | 33.20 | 63.20 |
| 50 | 33.70 | 69.00 |
| 75 | 35.50 | 79.80 |

Table 3.8: Material properties of SAC305 1DAY (RF) at $50^0$C

| Strain Rate (per sec) | E (GPa) | UTS (MPa) |
|---|---|---|
| 10 | 39.80 | 54.60 |
| 35 | 41.71 | 69.50 |
| 50 | 42.69 | 76.90 |
| 75 | 44.62 | 89.50 |

(a)



(b)

Figure 3.20: (a), (b) Stress vs. Strain for 1-day elevated temperature (75C) aged SAC105 and SAC305 alloys respectively

Table 3.9: Material properties of SAC105 1DAY (RF) at 75$^0$C

| Strain Rate (per sec) | E (GPa) | UTS (MPa) |
|---|---|---|
| 10 | 31.70 | 49.00 |
| 35 | 32.90 | 62.20 |
| 50 | 33.40 | 68.00 |
| 75 | 35.20 | 78.80 |

Table 3.10: Material properties of SAC305 1DAY (RF) at 75$^0$C

| Strain Rate (per sec) | E (GPa) | UTS (MPa) |
|---|---|---|
| 10 | 39.45 | 53.00 |
| 35 | 41.35 | 67.60 |
| 50 | 42.30 | 75.50 |
| 75 | 44.25 | 87.80 |

(a)



(b)

Figure 3.21: (a), (b) Stress vs. Strain for 1-day elevated temperature (100C) aged SAC105 and SAC305 alloys respectively

Table 3.11: Material properties of SAC105 1DAY (RF) at $100^0$C

| Strain Rate (per sec) | E (GPa) | UTS (MPa) |
|---|---|---|
| 10 | 31.40 | 48.40 |
| 35 | 32.60 | 61.60 |
| 50 | 33.10 | 67.40 |
| 75 | 34.90 | 78.20 |

Table 3.12: Material properties of SAC305 1DAY (RF) at $100^0$C

| Strain Rate (per sec) | E (GPa) | UTS (MPa) |
|---|---|---|
| 10 | 39.00 | 51.00 |
| 35 | 40.85 | 66.00 |
| 50 | 41.85 | 74.00 |
| 75 | 43.80 | 85.90 |

(a)



(b)

Figure 3.22 (a), (b) Stress vs. Strain for 1-day elevated temperature (125C) aged SAC105 and SAC305 alloys respectively

Table 3.13: Material properties of SAC105 1DAY (RF) at $125^0$C

| Strain Rate (per sec) | E (GPa) | UTS (MPa) |
|---|---|---|
| 10 | 31.30 | 48.00 |
| 35 | 32.50 | 61.20 |
| 50 | 33.00 | 67.00 |
| 75 | 34.80 | 77.80 |

Table 3.14: Material properties of SAC105 1DAY (RF) at $125^0$C

| Strain Rate (per sec) | E (GPa) | UTS (MPa) |
|---|---|---|
| 10 | 38.70 | 50.00 |
| 35 | 40.60 | 65.00 |
| 50 | 41.56 | 72.80 |
| 75 | 43.50 | 85.00 |
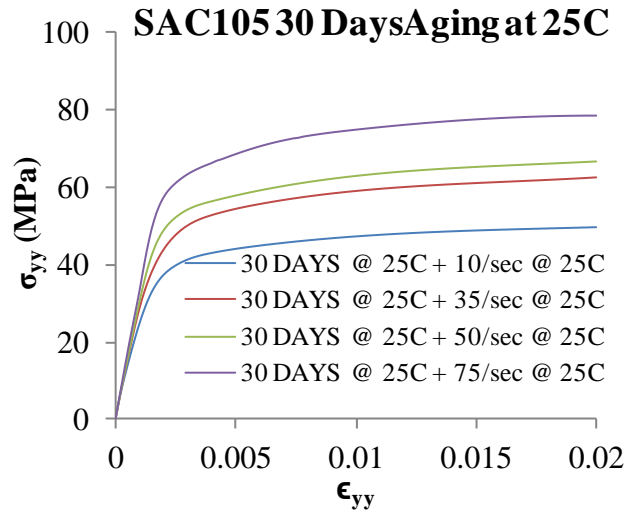
(a)
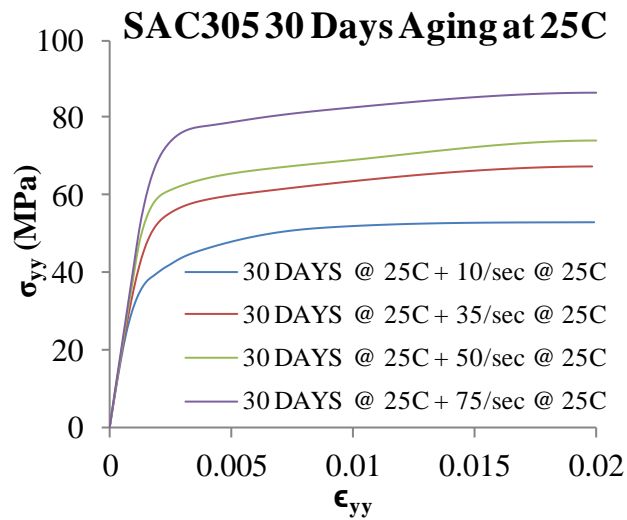


(b)

Figure 3.23: (a), (b) Stress vs. Strain for 30-days room temperature (25C) aged SAC105 and SAC305 alloys respectively

Table 3.15: Material properties of SAC105 30days (RF) at $25^0$C

| Strain Rate (per sec) | E (GPa) | UTS (MPa) |
|---|---|---|
| 10 | 31.60 | 49.80 |
| 35 | 32.85 | 62.50 |
| 50 | 33.27 | 66.75 |
| 75 | 35.00 | 78.20 |

Table 3.16: Material properties of SAC305 30days (RF) at $25^0$C

| Strain Rate (per sec) | E (GPa) | UTS (MPa) |
|---|---|---|
| 10 | 38.90 | 53.00 |
| 35 | 40.75 | 67.50 |
| 50 | 41.75 | 74.20 |
| 75 | 43.50 | 86.25 |
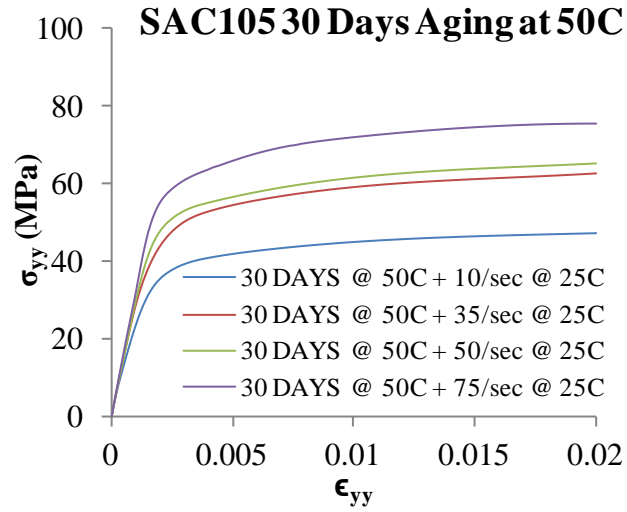
(a)
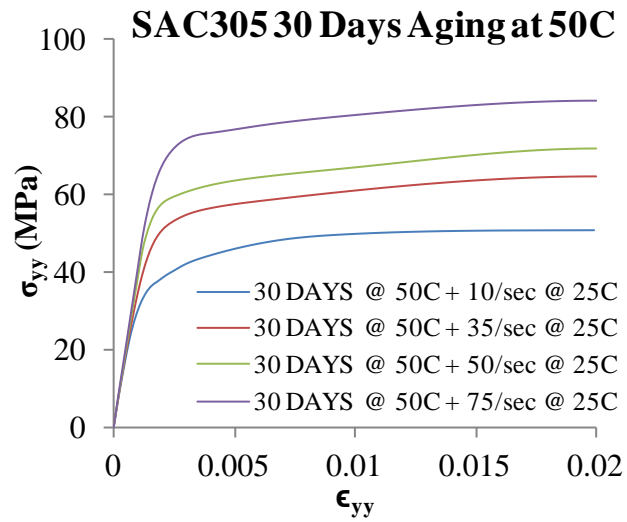


(b)

Figure 3.24: (a), (b) Stress vs. Strain for 30-days elevated temperature (50C) aged SAC105 and SAC305 alloys respectively

Table 3.17: Material properties of SAC105 30days (RF) at $50^0$C

| Strain Rate (per sec) | E (GPa) | UTS (MPa) |
|---|---|---|
| 10 | 30.75 | 47.40 |
| 35 | 31.90 | 60.00 |
| 50 | 32.50 | 65.30 |
| 75 | 34.00 | 75.70 |

Table 3.18: Material properties of SAC305 30days (RF) at $50^0$C

| Strain Rate (per sec) | E (GPa) | UTS (MPa) |
|---|---|---|
| 10 | 38.00 | 50.75 |
| 35 | 39.90 | 64.90 |
| 50 | 41.00 | 72.00 |
| 75 | 42.70 | 84.25 |
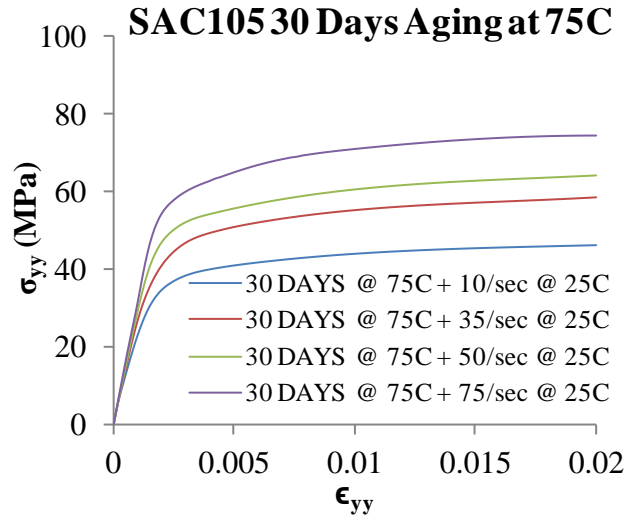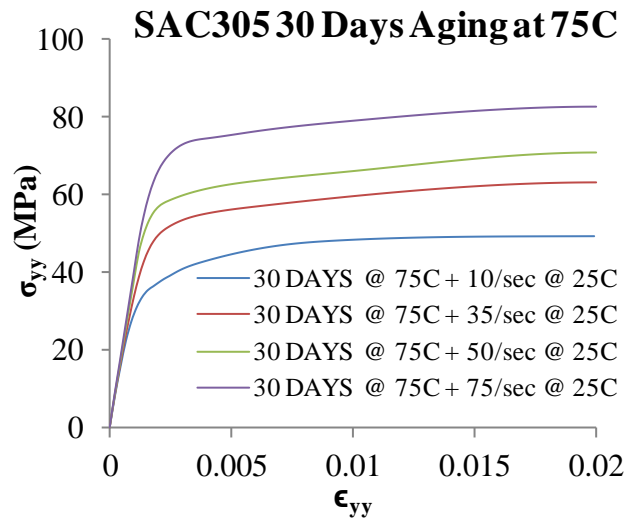
Figure 3.25: (a), (b) Stress vs. Strain for 30-days elevated temperature (75C) aged SAC105 and SAC305 alloys respectively

Table 3.19: Material properties of SAC105 30days (RF) at $75^0$C

| Strain Rate | E | UTS |
|---|---|---|
| (per sec) | (GPa) | (MPa) |
| 10 | 30.25 | 46.40 |
| 35 | 31.30 | 58.60 |
| 50 | 31.95 | 64.40 |
| 75 | 33.50 | 74.50 |

Table 3.20: Material properties of SAC305 30days (RF) at $75^0$C

| Strain Rate | E | UTS |
|---|---|---|
| (per sec) | (GPa) | (MPa) |
| 10 | 37.40 | 49.20 |
| 35 | 39.40 | 63.25 |
| 50 | 40.50 | 70.85 |
| 75 | 42.25 | 82.70 |
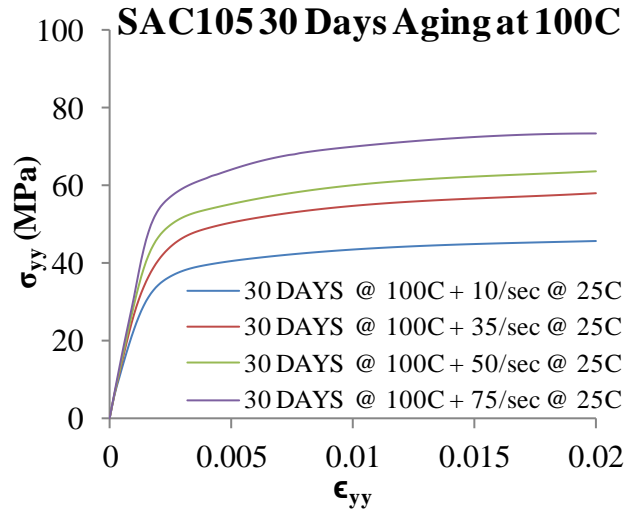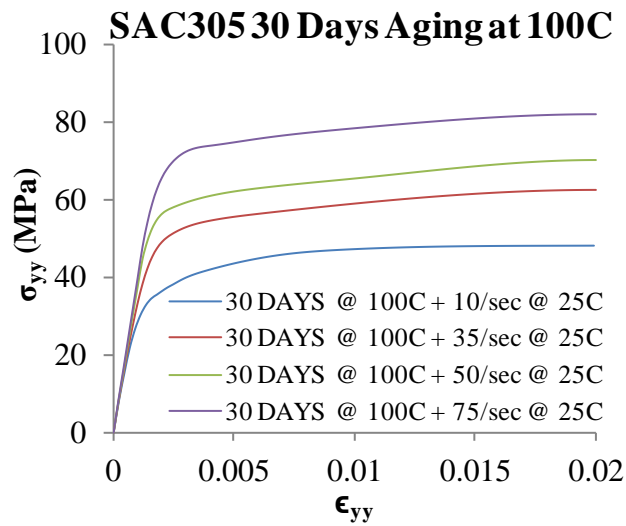
Figure 3.26: (a), (b) Stress vs. Strain for 30-days elevated temperature (100C) aged SAC105 and SAC305 alloys respectively

Table 3.21: Material properties of SAC105 30days (RF) at $100^0$C

| Strain Rate (per sec) | E (GPa) | UTS (MPa) |
|---|---|---|
| 10 | 29.87 | 45.60 |
| 35 | 30.95 | 58.00 |
| 50 | 31.55 | 63.80 |
| 75 | 33.00 | 73.70 |

Table 3.22: Material properties of SAC305 30days (RF) at $100^0$C

| Strain Rate (per sec) | E (GPa) | UTS (MPa) |
|---|---|---|
| 10 | 37.10 | 48.10 |
| 35 | 39.05 | 62.25 |
| 50 | 40.15 | 69.90 |
| 75 | 41.95 | 81.55 |
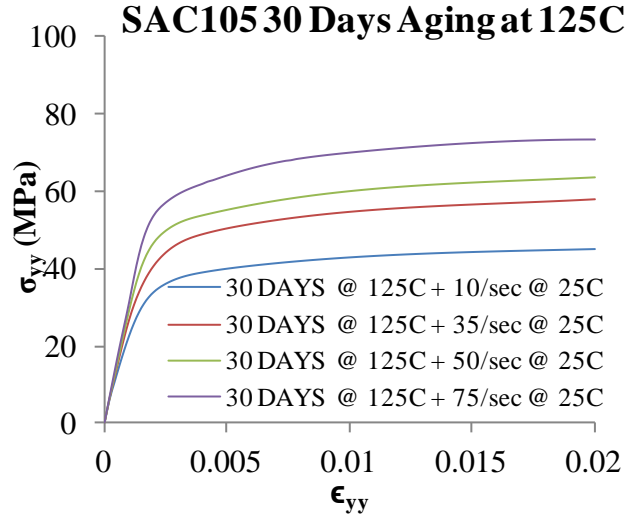
(a)
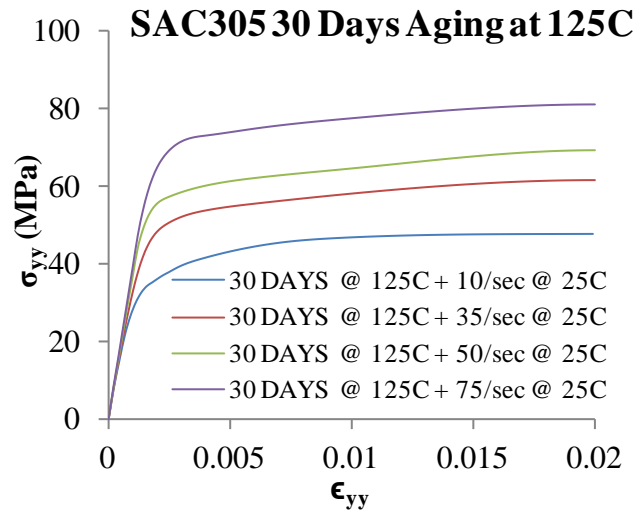


(b)

Figure 3.27: (a), (b) Stress vs. Strain for 30-days elevated temperature (125C) aged SAC105 and SAC305 alloys respectively

Table 3.23: Material properties of SAC105 30days (RF) at $125^0$C

| Strain Rate (per sec) | E (GPa) | UTS (MPa) |
|---|---|---|
| 10 | 29.70 | 45.20 |
| 35 | 30.80 | 57.50 |
| 50 | 31.35 | 63.50 |
| 75 | 32.95 | 73.20 |

Table 3.24: Material properties of SAC305 30days (RF) at $125^0$C

| Strain Rate (per sec) | E (GPa) | UTS (MPa) |
|---|---|---|
| 10 | 36.85 | 47.40 |
| 35 | 38.80 | 61.50 |
| 50 | 39.90 | 69.25 |
| 75 | 41.70 | 80.75 |
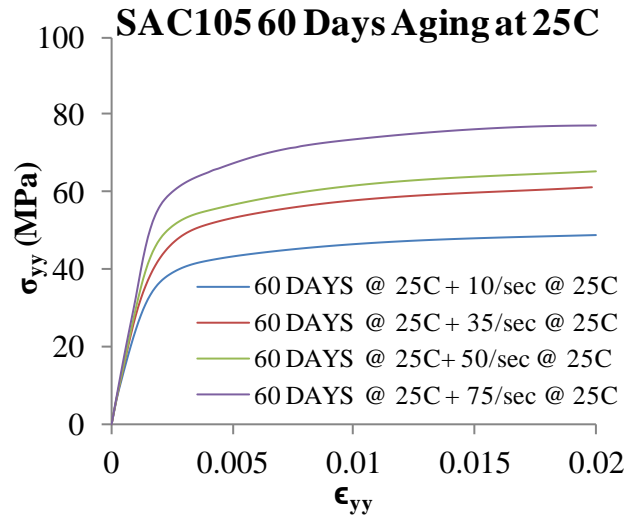
(a)
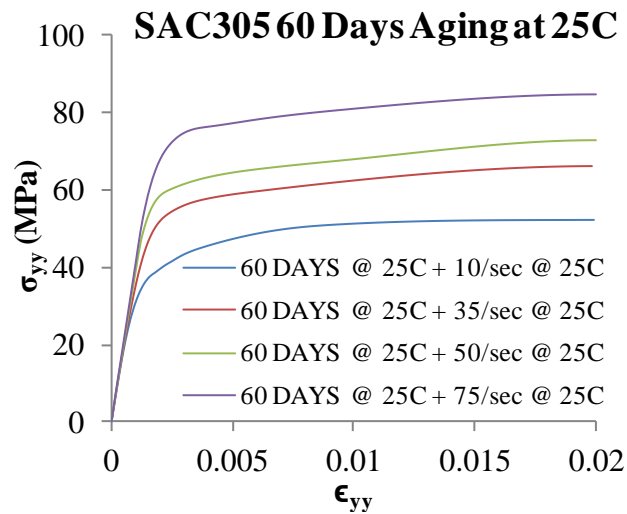


(b)

Figure 3.28: (a), (b) Stress vs. Strain for 60-days room temperature (25C) aged SAC105 and SAC305 alloys respectively

Table 3.25: Material properties of SAC105 60days (RF) at $25^0$C

| Strain Rate | E | UTS |
|---|---|---|
| (per sec) | (GPa) | (MPa) |
| 10 | 31.33 | 48.93 |
| 35 | 32.49 | 61.35 |
| 50 | 32.97 | 65.10 |
| 75 | 34.70 | 76.97 |

Table 3.26: Material properties of SAC305 60days (RF) at $25^0$C

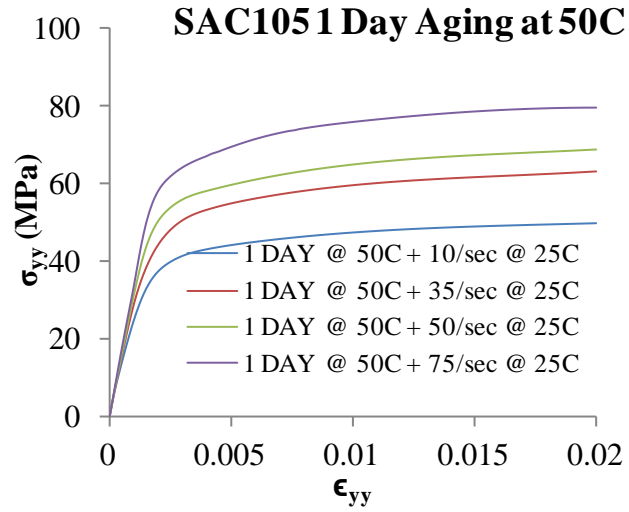| Strain Rate | E | UTS |
|---|---|---|
| (per sec) | (GPa) | (MPa) |
| 10 | 38.51 | 52.20 |
| 35 | 40.32 | 66.17 |
| 50 | 41.25 | 72.98 |
| 75 | 43.11 | 84.81 |
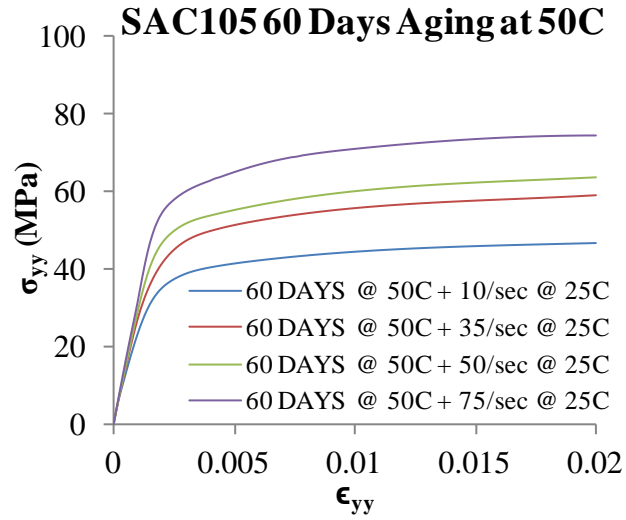
(a)
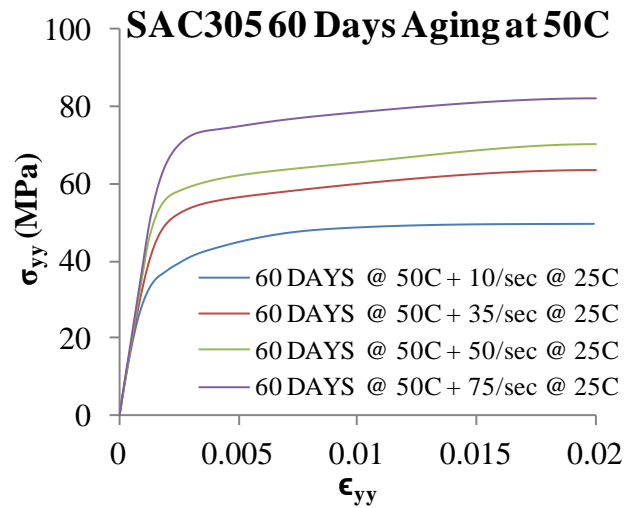


(b)

Figure 3.29: (a), (b) Stress vs. Strain for 60-days elevated temperature (50C) aged SAC105 and SAC305 alloys respectively

Table 3.27: Material properties of SAC105 60days (RF) at $50^0$C

| Strain Rate (per sec) | E (GPa) | UTS (MPa) |
|---|---|---|
| 10 | 30.38 | 46.80 |
| 35 | 31.53 | 59.16 |
| 50 | 32.00 | 63.74 |
| 75 | 33.70 | 74.70 |

Table 3.28: Material properties of SAC305 60days (RF) at $50^0$C

| Strain Rate (per sec) | E (GPa) | UTS (MPa) |
|---|---|---|
| 10 | 37.48 | 49.35 |
| 35 | 39.28 | 63.31 |
| 50 | 40.19 | 70.34 |
| 75 | 42.04 | 81.93 |
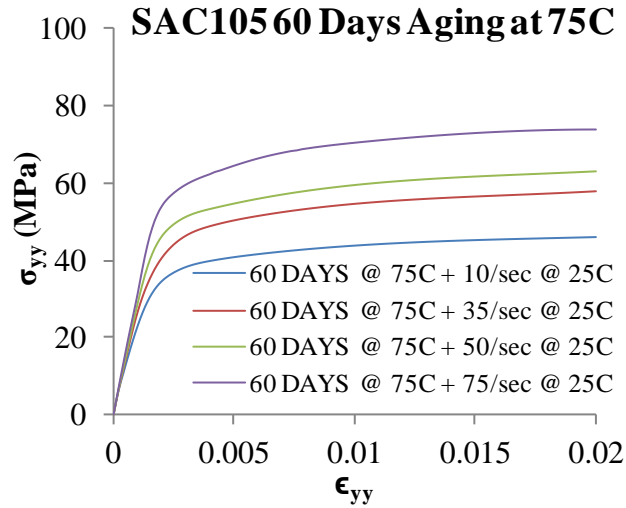
(a)
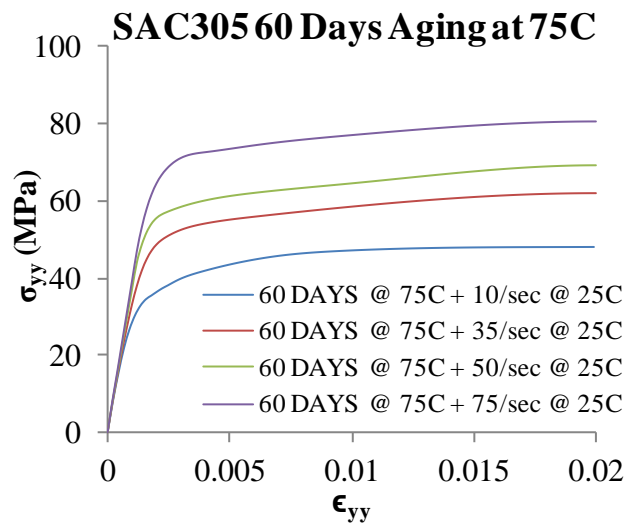


(b)

Figure 3.30: (a), (b) Stress vs. Strain for 60-days elevated temperature (75C) aged SAC105 and SAC305 alloys respectively

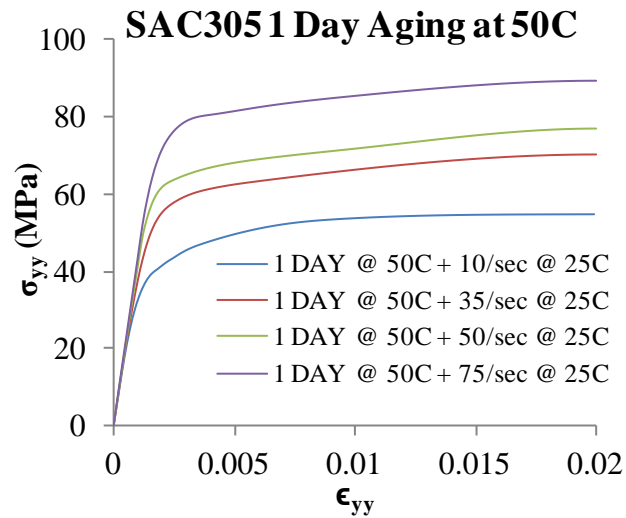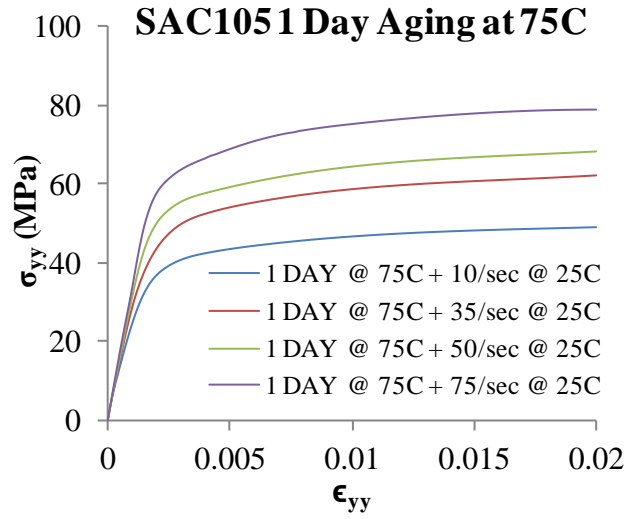Table 3.29: Material properties of SAC105 60days (RF) at $75^0$C

| Strain Rate (per sec) | E (GPa) | UTS (MPa) |
|:---:|:---:|:---:|
| 10 | 29.90 | 45.74 |
| 35 | 31.00 | 58.00 |
| 50 | 31.50 | 63.00 |
| 75 | 33.20 | 73.56 |

Table 3.30: Material properties of SAC305 60days (RF) at $75^0$C

| Strain Rate (per sec) | E (GPa) | UTS (MPa) |
|:---:|:---:|:---:|
| 10 | 36.97 | 47.93 |
| 35 | 38.76 | 61.88 |
| 50 | 39.67 | 69.02 |
| 75 | 41.51 | 80.49 |
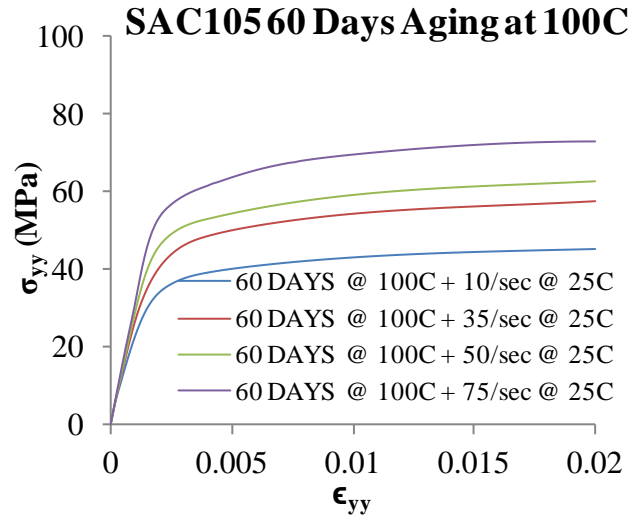
(a)
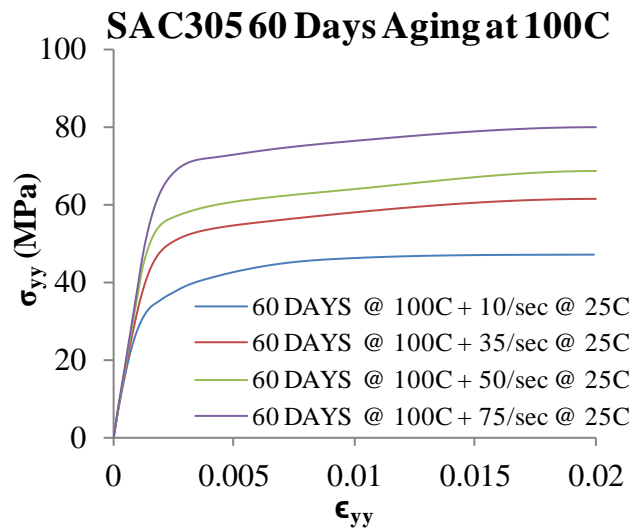


(b)

Figure 3.31: (a), (b) Stress vs. Strain for 60-days elevated temperature (100C) aged SAC105 and SAC305 alloys respectively

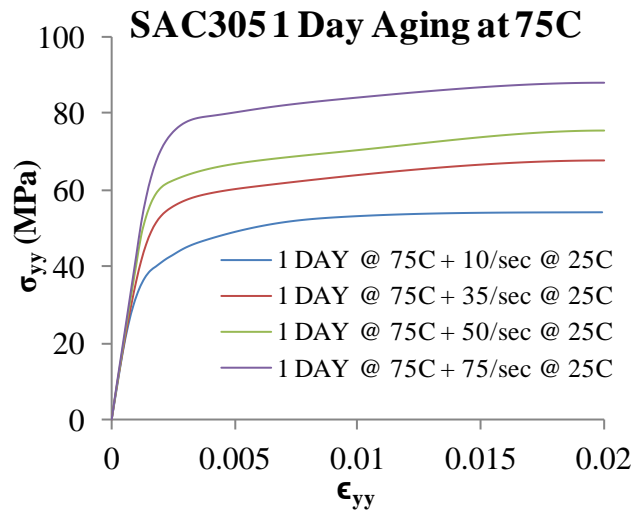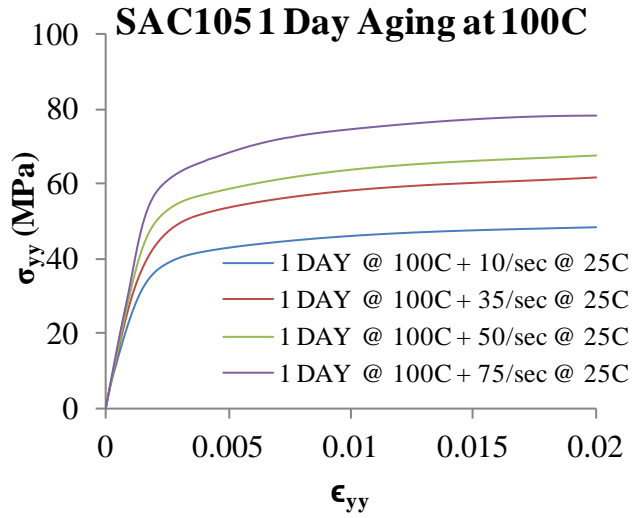Table 3.31: Material properties of SAC105 60days (RF) at $100^0$C

| Strain Rate (per sec) | E (GPa) | UTS (MPa) |
|---|---|---|
| 10 | 29.60 | 45.20 |
| 35 | 30.70 | 57.40 |
| 50 | 31.15 | 62.60 |
| 75 | 32.90 | 72.90 |

Table 3.32: Material properties of SAC305 60days (RF) at $100^0$C

| Strain Rate (per sec) | E (GPa) | UTS (MPa) |
|---|---|---|
| 10 | 36.71 | 47.21 |
| 35 | 38.50 | 61.17 |
| 50 | 39.41 | 68.36 |
| 75 | 41.25 | 79.77 |
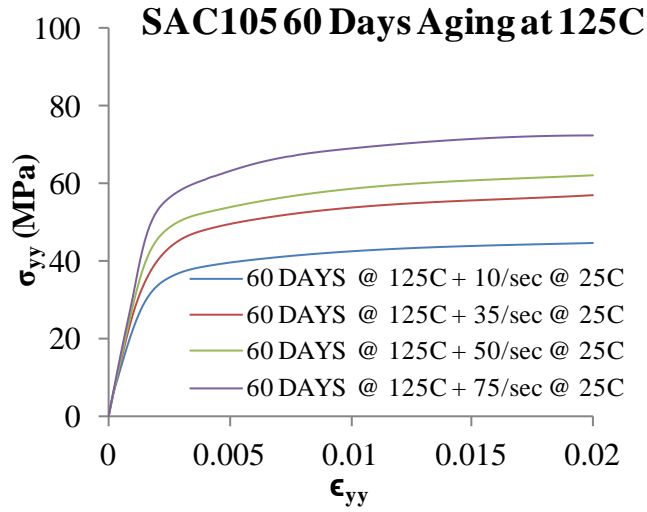
(a)
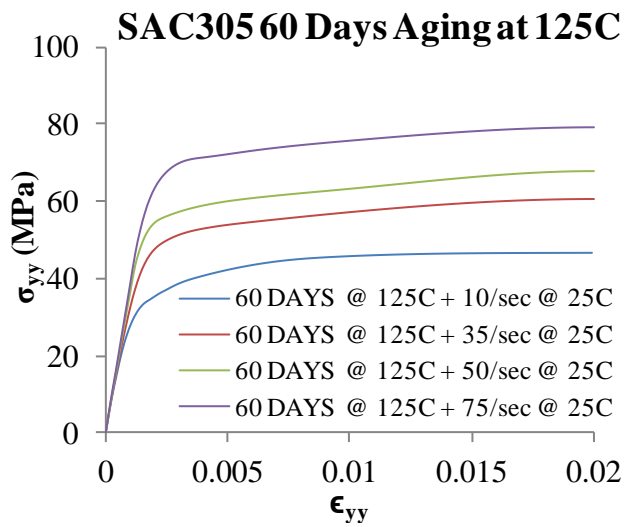


(b)

Figure 3.32: (a), (b) Stress vs. Strain for 60-days elevated temperature (125C) aged SAC105 and SAC305 alloys respectively

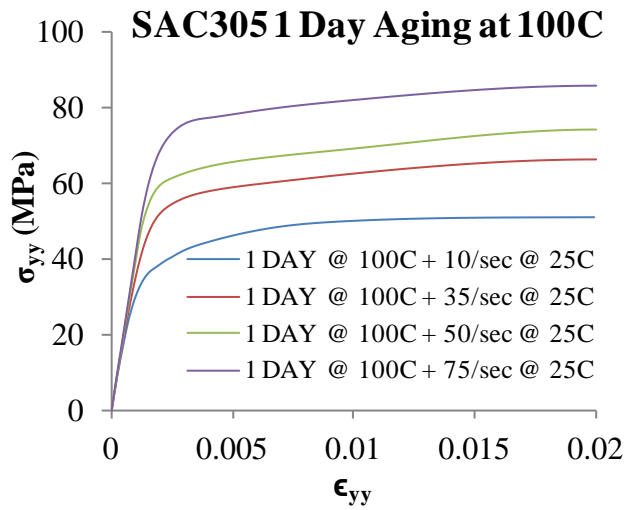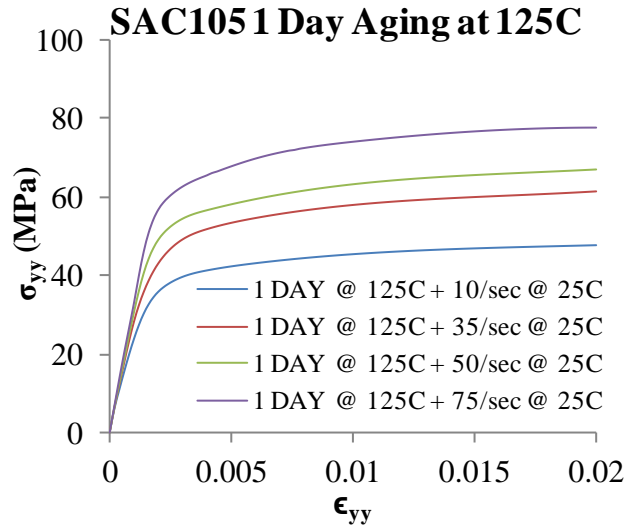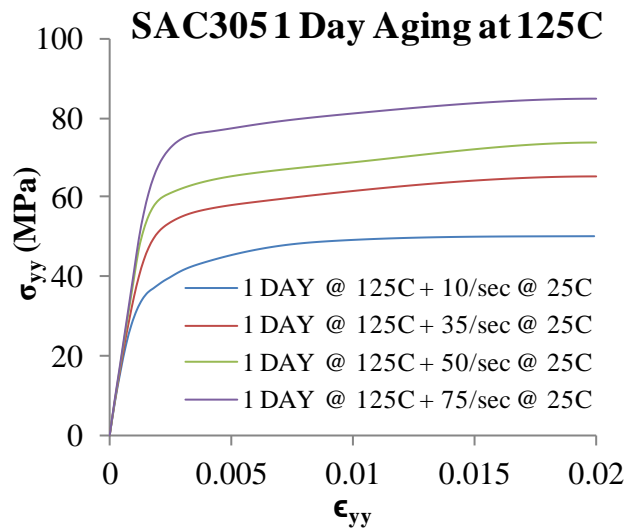Table 3.33: Material properties of SAC105 60days (RF) at $125^0$C

| Strain Rate | E | UTS |
|---|---|---|
| (per sec) | (GPa) | (MPa) |
| 10 | 29.44 | 44.69 |
| 35 | 30.57 | 56.98 |
| 50 | 31.01 | 62.38 |
| 75 | 32.70 | 72.43 |

Table 3.34: Material properties of SAC305 60days (RF) at $125^0$C

| Strain Rate | E | UTS |
|---|---|---|
| (per sec) | (GPa) | (MPa) |
| 10 | 36.46 | 46.50 |
| 35 | 38.25 | 60.45 |
| 50 | 39.15 | 67.70 |
| 75 | 40.98 | 79.05 |

**3.8.2 Aging Effects on High Strain Rate Date of SAC Solder Alloys**



(a)



(b)



(c)



(d)
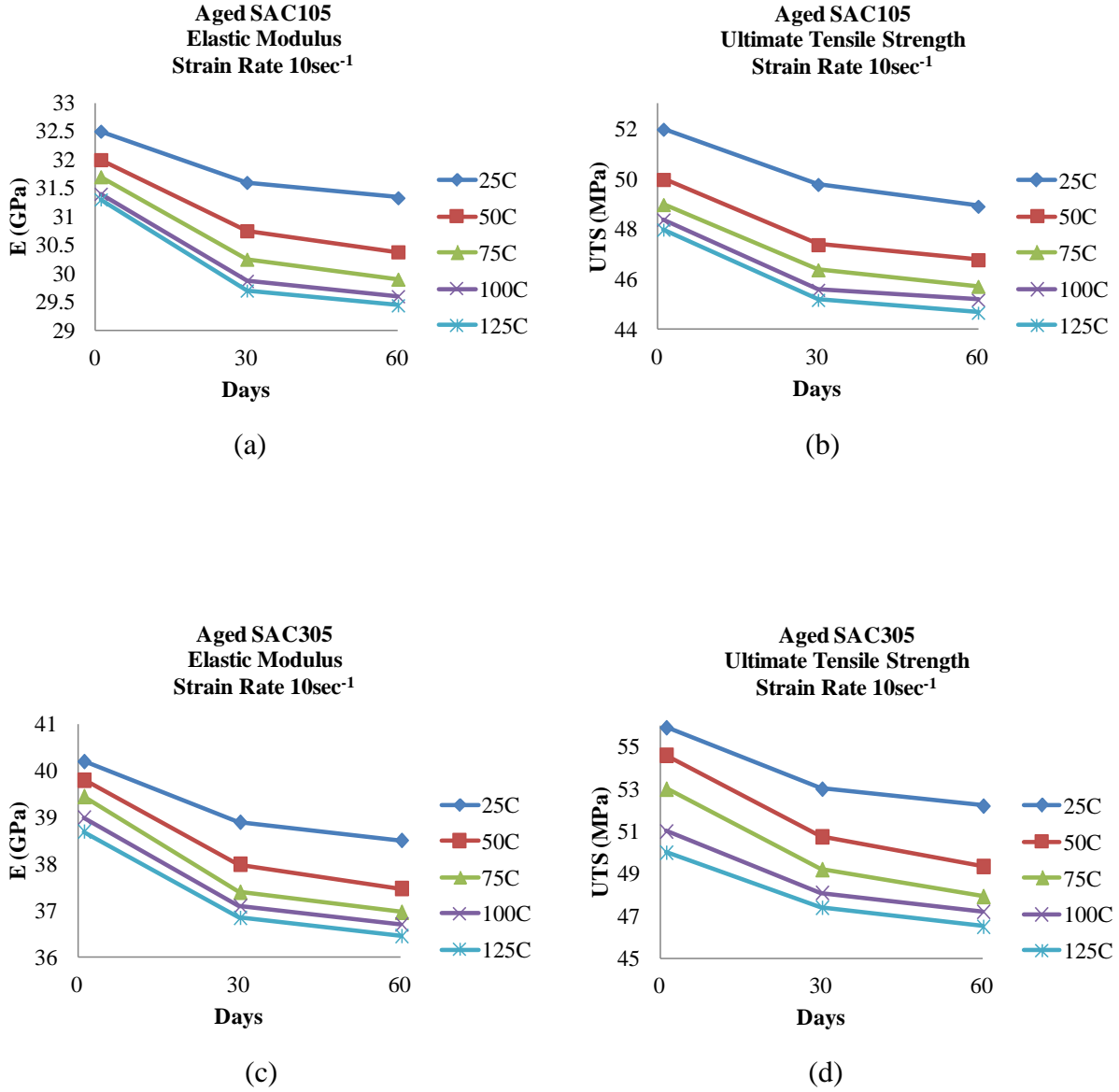
Figure 3.33:  Aging and temperature effects on the material properties of SAC105 and SAC305 solder alloys at strain rate 10 sec$^{-1}$

Table 3.35: Percentage reduction in the material properties of the aged SAC105 w.r.t pristine SAC105 at strain rate 10 sec$^{-1}$

| | Aged SAC105 tested at strain rate 10 sec$^{-1}$ | | | | | | | | | |
| | Elastic Modulus (% reduction) | | | | | UTS (% reduction) | | | | |
| Aging | 25C | 50C | 75C | 100C | 125C | 25C | 50C | 75C | 100C | 125C |
|---|---|---|---|---|---|---|---|---|---|---|
| 1 day | Pristine | 1.54 | 2.46 | 3.38 | 3.69 | Pristine | 3.85 | 5.77 | 6.92 | 7.69 |
| 30 days | 2.77 | 5.38 | 6.92 | 8.09 | 8.62 | 4.23 | 8.85 | 10.77 | 12.31 | 13.08 |
| 60 days | 3.60 | 6.52 | 8.00 | 8.92 | 9.42 | 5.90 | 10.00 | 12.04 | 13.08 | 14.06 |

Table 3.36: Percentage reduction of the material properties of the aged SAC305 w.r.t pristine SAC305 at strain rate 10 sec$^{-1}$

| | Aged SAC305 tested at strain rate 10 sec$^{-1}$ | | | | | | | | | |
| | Elastic Modulus (% reduction) | | | | | UTS (% reduction) | | | | |
| Aging | 25C | 50C | 75C | 100C | 125C | 25C | 50C | 75C | 100C | 125C |
|---|---|---|---|---|---|---|---|---|---|---|
| 1 day | Pristine | 0.96 | 1.87 | 2.99 | 3.73 | Pristine | 2.32 | 5.19 | 8.77 | 10.55 |
| 30 days | 3.23 | 5.47 | 6.97 | 7.71 | 8.33 | 5.19 | 9.21 | 11.99 | 13.95 | 15.20 |
| 60 days | 4.20 | 6.77 | 8.03 | 8.69 | 9.30 | 6.62 | 11.72 | 14.26 | 15.55 | 16.82 |
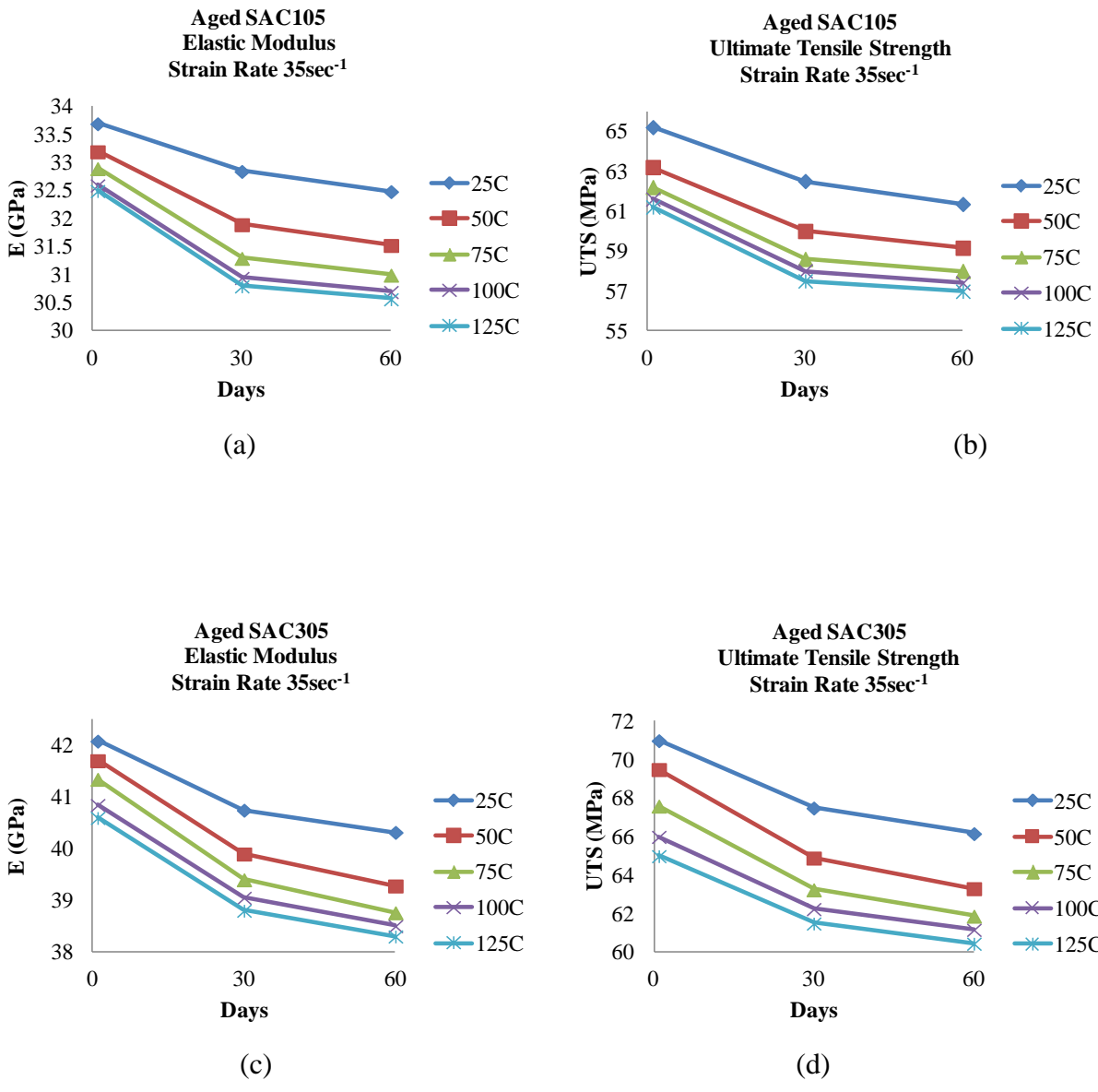
Figure 3.34: Aging and temperature effects on the material properties of SAC105 and SAC305 solder alloys at strain rate 35 sec^{-1}

Table 3.37: Percentage reduction in the material properties of the aged SAC105 w.r.t pristine SAC105 at strain rate 35 sec$^{-1}$

| | Aged SAC105 tested at strain rate 35 sec$^{-1}$ | | | | | | | | | |
| | Elastic Modulus (% reduction) | | | | | UTS (% reduction) | | | | |
| Aging | 25C | 50C | 75C | 100C | 125C | 25C | 50C | 75C | 100C | 125C |
|---|---|---|---|---|---|---|---|---|---|---|
| 1 day | Pristine | 1.48 | 2.37 | 3.26 | 3.56 | Pristine | 3.07 | 4.60 | 5.52 | 6.13 |
| 30 days | 2.52 | 5.34 | 7.12 | 8.16 | 8.61 | 4.114 | 7.98 | 10.12 | 11.04 | 11.81 |
| 60 days | 3.59 | 6.44 | 8.01 | 8.90 | 9.29 | 5.91 | 9.26 | 11.04 | 11.96 | 12.61 |

Table 3.38: Percentage reduction of the material properties of the aged SAC305 w.r.t pristine SAC305 at strain rate 35 sec$^{-1}$

| | Aged SAC305 tested at strain rate 35 sec$^{-1}$ | | | | | | | | | |
| | Elastic Modulus (% reduction) | | | | | UTS (% reduction) | | | | |
| Aging | 25C | 50C | 75C | 100C | 125C | 25C | 50C | 75C | 100C | 125C |
|---|---|---|---|---|---|---|---|---|---|---|
| 1 day | Pristine | 0.90 | 1.76 | 2.95 | 3.54 | Pristine | 2.11 | 4.79 | 7.04 | 8.45 |
| 30 days | 3.18 | 5.20 | 6.39 | 7.22 | 7.82 | 4.93 | 8.59 | 10.92 | 12.32 | 13.38 |
| 60 days | 4.21 | 6.68 | 7.91 | 8.53 | 9.12 | 6.80 | 10.83 | 12.85 | 13.85 | 14.86 |
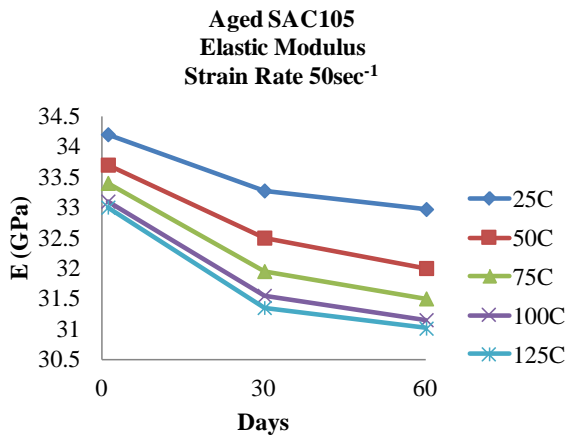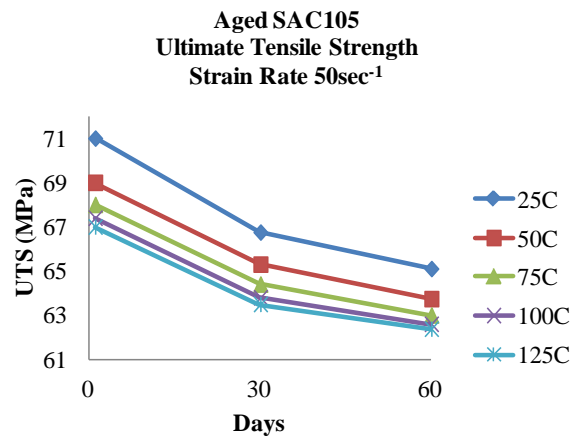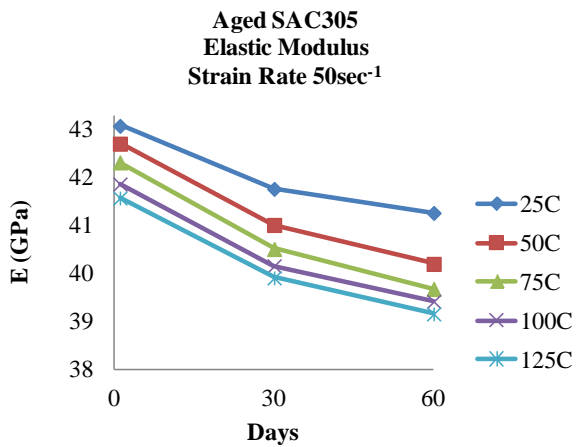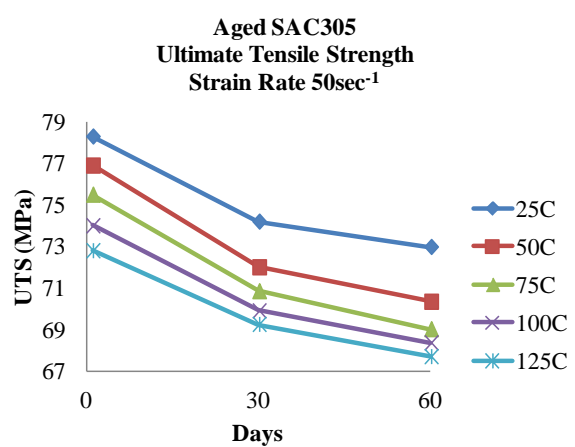
Figure 3.35:  Aging and temperature effects on the material properties of SAC105 and SAC305 solder alloys at strain rate 50 sec$^{-1}$

Table 3.39: Percentage reduction in the material properties of the aged SAC105 w.r.t pristine SAC105 at strain rate 50 sec$^{-1}$

| | Aged SAC105 tested at strain rate 50 sec$^{-1}$ | | | | | | | | | |
| --- | --- | --- | --- | --- | --- | --- | --- | --- | --- | --- |
| | Elastic Modulus (% reduction) | | | | | UTS (% reduction) | | | | |
| Aging | 25C | 50C | 75C | 100C | 125C | 25C | 50C | 75C | 100C | 125C |
| 1 day | Pristine | 1.46 | 2.34 | 3.22 | 3.51 | Pristine | 2.82 | 4.22 | 5.07 | 5.63 |
| 30 days | 2.72 | 4.97 | 6.58 | 7.75 | 8.33 | 5.99 | 8.03 | 9.30 | 10.14 | 10.56 |
| 60 days | 3.59 | 6.43 | 7.90 | 8.92 | 9.33 | 8.31 | 10.22 | 11.27 | 11.83 | 12.14 |

Table 3.40: Percentage reduction of the material properties of the aged SAC305 w.r.t pristine SAC305 at strain rate 50 sec$^{-1}$

| | Aged SAC305 tested at strain rate 50 sec$^{-1}$ | | | | | | | | | |
| --- | --- | --- | --- | --- | --- | --- | --- | --- | --- | --- |
| | Elastic Modulus (% reduction) | | | | | UTS (% reduction) | | | | |
| Aging | 25C | 50C | 75C | 100C | 125C | 25C | 50C | 75C | 100C | 125C |
| 1 day | Pristine | 0.86 | 1.76 | 2.81 | 3.48 | Pristine | 1.79 | 3.56 | 5.49 | 7.02 |
| 30 days | 3.04 | 4.78 | 5.95 | 6.76 | 7.34 | 5.24 | 8.05 | 9.51 | 1073 | 11.56 |
| 60 days | 4.20 | 6.67 | 7.87 | 8.48 | 9.08 | 6.80 | 10.17 | 11.85 | 12.70 | 13.54 |
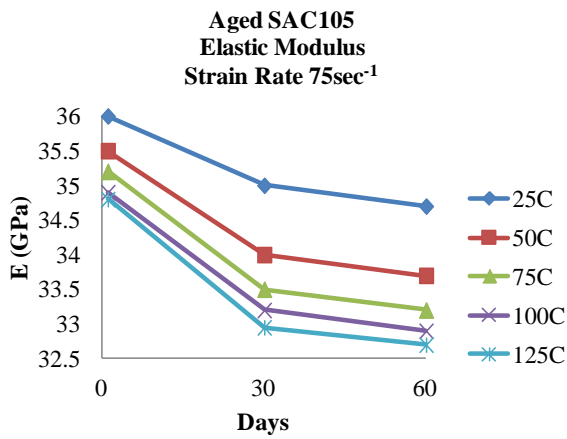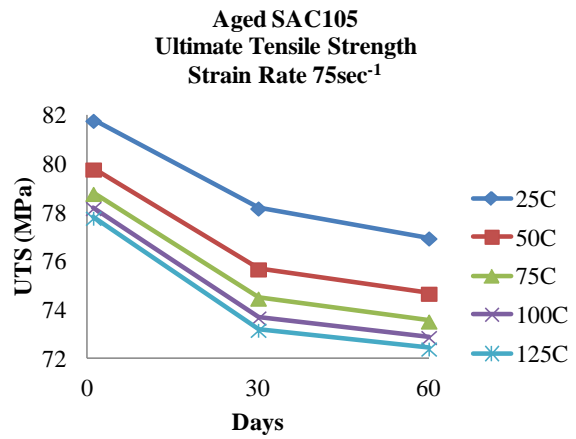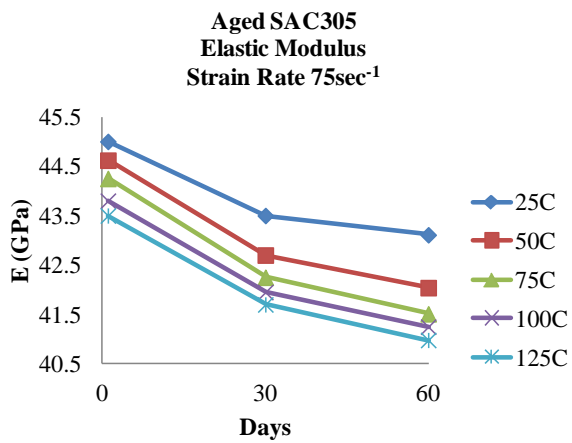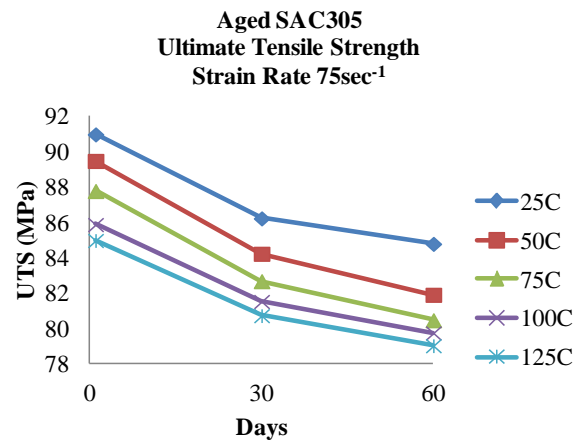
Figure 3.36: Aging and temperature effects on the material properties of SAC105 and SAC305 solder alloys at strain rate 75 sec^{-1}

Table 3.41: Percentage reduction in the material properties of the aged SAC105 w.r.t pristine SAC105 at strain rate 75 sec$^{-1}$

| | Aged SAC105 tested at strain rate 75 sec$^{-1}$ | | | | | | | | | |
| | Elastic Modulus (% reduction) | | | | | UTS (% reduction) | | | | |
| Aging | 25C | 50C | 75C | 100C | 125C | 25C | 50C | 75C | 100C | 125C |
|---|---|---|---|---|---|---|---|---|---|---|
| 1 day | Pristine | 1.39 | 2.22 | 3.06 | 3.33 | Pristine | 2.44 | 3.67 | 4.40 | 4.89 |
| 30 days | 2.78 | 5.56 | 6.94 | 8.33 | 8.47 | 4.40 | 7.46 | 8.92 | 9.90 | 10.51 |
| 60 days | 3.61 | 6.39 | 7.78 | 8.61 | 9.17 | 5.90 | 8.68 | 10.07 | 10.90 | 11.45 |

Table 3.42: Percentage reduction of the material properties of the aged SAC305 w.r.t pristine SAC305 at strain rate 75 sec$^{-1}$

| | Aged SAC305 tested at strain rate 75 sec$^{-1}$ | | | | | | | | | |
| | Elastic Modulus (% reduction) | | | | | UTS (% reduction) | | | | |
| Aging | 25C | 50C | 75C | 100C | 125C | 25C | 50C | 75C | 100C | 125C |
|---|---|---|---|---|---|---|---|---|---|---|
| 1 day | Pristine | 0.84 | 1.67 | 2.67 | 3.33 | Pristine | 1.65 | 3.52 | 5.60 | 6.59 |
| 30 days | 3.33 | 5.11 | 6.12 | 6.78 | 7.33 | 5.21 | 7.42 | 9.12 | 10.38 | 11.26 |
| 60 days | 43.11 | 6.58 | 7.76 | 8.34 | 8.93 | 6.80 | 9.97 | 11.55 | 12.34 | 13.13 |

Following conclusion can be drawn from high strain rate test data set:

*Effect of Strain Rate*

Material properties for both lead free solder alloys show sensitivity to strain rates. Pristine SAC105 tested at high strain rates in the neighborhood of 1-100 sec$^{-1}$ exhibits (a) an average increase of 5.28 percent in the elastic modulus and (b) an average increase of 45.48 percent in the ultimate tensile strength with the increase in strain rate. Pristine SAC305 tested at high strain rates in the range of 1-100 sec$^{-1}$ exhibits (a) an increase of 7.34 percent in the elastic modulus and (b) an increase of 53.73 percent in the UTS as the strain rate increases.

*Effect of Aging Duration*

Material properties for both lead free solder alloys exhibit sensitivity to the aging duration at temperatures of 25°C, 50°C, 75°C, 100°C, and 125°C. For RT aged SAC105 for 1 day to 60 days, the elastic modulus (E) drops on by 3.6 percent on average and UTS drops by 5.9 percent on average, at strain rates of 1-100sec$^{-1}$. However, for 125°C aged SAC105 for 1 day to 60 days, the elastic modulus (E) drops on by 5.9 percent on average and UTS drops by 6.9 percent on average, at strain rates of 1-100sec$^{-1}$. For RT aged SAC305 for 1 day to 60 days, the elastic modulus (E) drops on by 4.2 percent on average and UTS drops by 6.8 percent on average, at strain rates of 1-100sec$^{-1}$. However, for 125°C aged SAC305 for 1 day to 60 days, the elastic modulus (E) drops on by 5.6 percent on average and UTS drops by 7 percent on average, at strain rates of 1-100sec$^{-1}$.

*Effect of Exposure to Elevated Temperature*

Material properties for both SAC105 and SAC305 lead free solder alloys are sensitive to the aging temperatures for a given period of time. Properties degrade nonlinearly under exposure to temperatures between 25°C to 125°C for times of 1 day to 60 days. Pristine samples show a

higher mechanical strength when compared to the elevated temperature aged samples in each case. Samples exposed to 60 days of constant temperature aging shows the lowest mechanical strength of all the cases tested.

### 3.9 Effect of Rate of Specimen Cooling

Test specimens were also subjected to water quenching to determine the effect of specimen cooling rate on the material properties of lead free solder alloys. Figure 3.38 (a), (b), shows the stress strain plots for water quenched specimens which were then subjected to 1days room temperature (25C) aging conditions. On average water quenched elastic modulus (E) $E_{105}$ is 9.7% greater than reflowed $E_{105}$. On average water quenched ultimate tensile strength (UTS) $UTS_{105}$ is 19.5% greater than reflowed $UTS_{105}$. On average water quenched $E_{305}$ is 11% greater than reflowed $E_{305}$. On average water quenched $UTS_{305}$ is 22% greater than reflowed $U_{305}$.
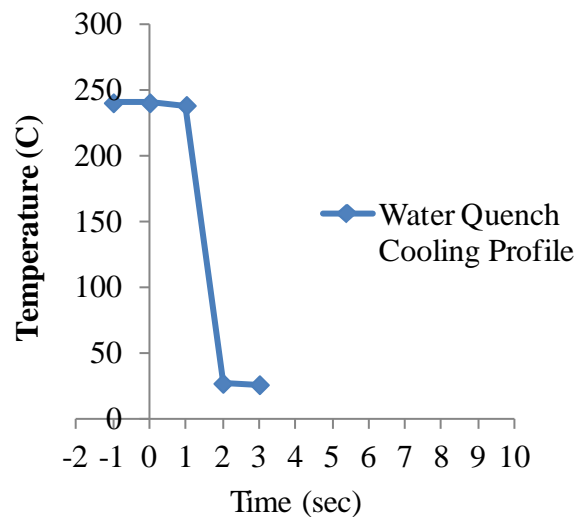


Figure 3.37: Water quench profile
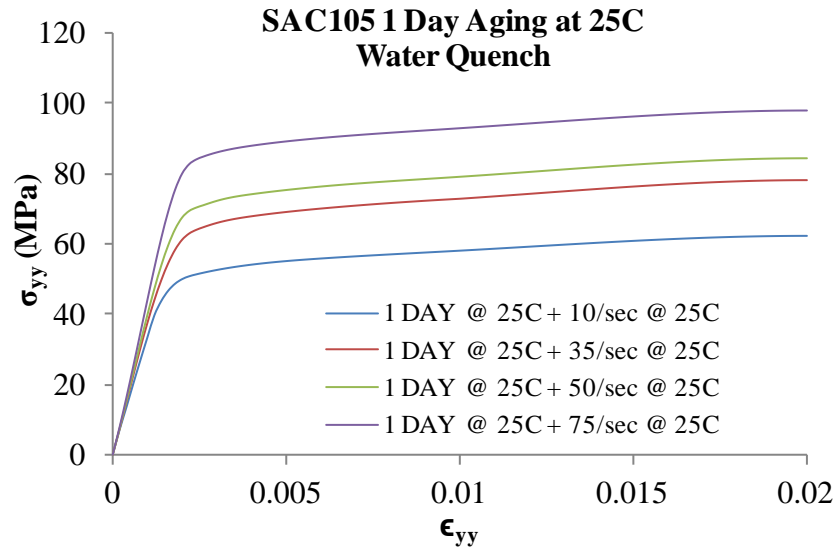
(a)
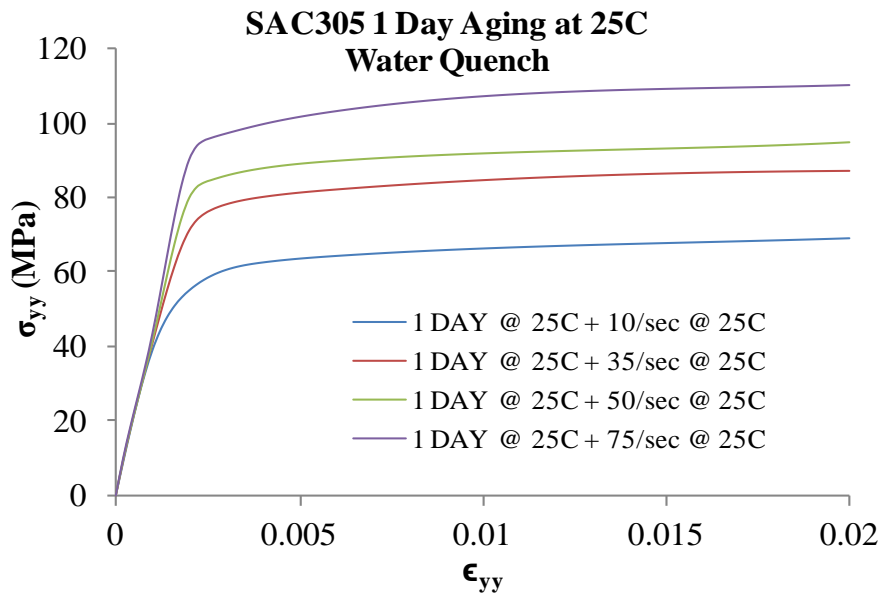


(b)

Figure 3.38: (a), (b) Stress vs. Strain for 1days room temperature (25C) aged SAC105 and SAC305 (*water quenched*) alloys respectively

Table 3.43: Material properties of SAC105 1day (water quenched) at $25^0$C

| Strain Rate (per sec) | E (GPa) | UTS (MPa) |
|---|---|---|
| 10 | 35.65 | 62.10 |
| 35 | 36.97 | 77.90 |
| 50 | 37.52 | 84.50 |
| 75 | 39.49 | 97.70 |

Table 3.44: Material properties of SAC305 1days (water quenched) at $25^0$C

| Strain Rate (per sec) | E (GPa) | UTS (MPa) |
|---|---|---|
| 10 | 44.62 | 69.00 |
| 35 | 46.71 | 87.00 |
| 50 | 47.59 | 95.00 |
| 75 | 49.70 | 110.00 |

### 3.10    Ramberg-Osgood's Nonlinear Model

Ramberg-Osgood's model [Ramberg 1943] has been used to describe non-linear relationship between stress-strain. This mathematical model is suitable for SAC alloys which harden with plastic deformation (strain hardening) showing smooth transition in the elastic-plastic region in stress-strain curve.

$$\varepsilon = \left[ \frac{\sigma}{E} \right]_e + \left[ K \left( \frac{\sigma}{E} \right)^n \right]_p \tag{3.13}$$

Where $\varepsilon$ is the strain along the axial direction of the sample, $\sigma$ is the stress along the axial direction of the sample, E is the Elastic modulus, K and n are the material constants or shape parameter. The subscripts 'e' and 'p' correspond to the elastic and plastic portions of the deformation.

*Approach for Estimation of the Ramberg-Osgood Parameters (closed-form)*

Equation (3.13) can be written in dimensionless form as follows:

$$\alpha = \frac{\varepsilon}{\sigma_1} E \tag{3.14}$$

$$\varphi = \frac{\sigma}{\sigma_1} \tag{3.15}$$

Where, $\alpha$ and $\varphi$ are dimensionless variables, $\sigma_1$ is the secant yield strength. Multiply both sides of the equation (3.13) by $\left( \dfrac{E}{\sigma_1} \right)$:

$$\left( \frac{E\varepsilon}{\sigma_1} \right) = \frac{E}{\sigma_1} \left[ \frac{\sigma}{E} \right] + \left[ K \frac{E}{\sigma_1} \left( \frac{\sigma}{E} \right)^n \right] \tag{3.16}$$

From equation (3.14) and (3.15):

$$\alpha = \varphi + \left[ K \frac{\sigma}{\sigma_1} \left( \frac{\sigma}{E} \right)^{n-1} \right] \tag{3.17}$$

$$\alpha = \varphi + \left[ K\varphi \left( \frac{\sigma}{E} \right)^{n-1} \right] \tag{3.18}$$

From equation (15), substitute for $\sigma = \varphi\sigma_1$, in equation (3.18):

$$\alpha = \varphi + \left[ K\varphi \left( \frac{\varphi\sigma_1}{E} \right)^{n-1} \right] \tag{3.19}$$

$$\alpha = \varphi + \left[ K\varphi^n \left( \frac{\sigma_1}{E} \right)^{n-1} \right] \tag{3.20}$$

The abscissa of the secant yield strength for stress-strain curve in Figure 3.39 is given by modifying equation (3.13), and substituting $\sigma = \sigma_1$ :

$$\varepsilon_1 = \frac{\sigma_1}{m_1 E} = \frac{\sigma_1}{E} + K \left( \frac{\sigma_1}{E} \right)^n \tag{3.21}$$

Where $m_1 E = \dfrac{\sigma_1}{\varepsilon_1}$ as shown in Figure 3.39.
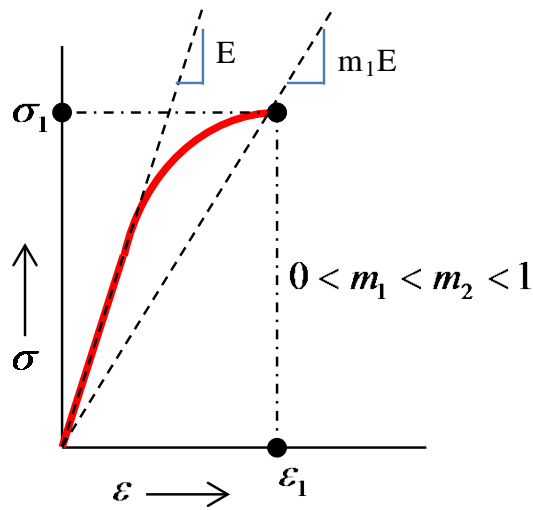


Figure 3.39: Determination of secant yield strength

Multiplying equation (3.21) by $\dfrac{E}{\sigma_1}$

$$\frac{1}{m_1} = 1 + K\left(\frac{\sigma_1}{E}\right)^{n-1} \qquad (3.22)$$

Rearranging the terms:

$$K = \left(\frac{1-m_1}{m_1}\right)\left(\frac{\sigma_1}{E}\right)^{1-n} \qquad (3.23)$$

Substitute K in equation 3.20,

$$\alpha = \varphi + \left[\left(\frac{1-m_1}{m_1}\right)\left(\frac{\sigma_1}{E}\right)^{1-n}\varphi^n\left(\frac{\sigma_1}{E}\right)^{n-1}\right] \qquad (3.24)$$

$$\alpha = \varphi + \left(\frac{1-m_1}{m_1}\right)\varphi^n \qquad (3.25)$$
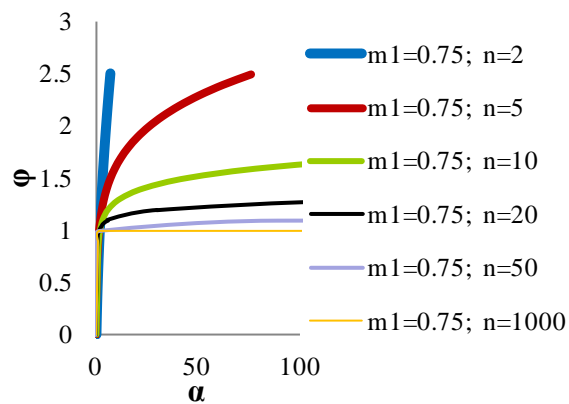


Figure 3.40: Family of curves for different values o f n and m1=0.75

99

Related stress-strain curves that may be described by equation (3.25) are characterized by having the same value n. Figure 3.40 shows family of curves for different values of n and m1=0.75. The stress deviation curve has been obtained by plotting stress against the difference between the measured strain and elastic strain according to Hooke's Law:

$$d = \varepsilon - \frac{\sigma}{E}$$ (3.26)

$$d = \frac{\sigma}{E} + \left[ K \left( \frac{\sigma}{E} \right)^n \right] - \frac{\sigma}{E} = K \left( \frac{\sigma}{E} \right)^n$$ (3.27)

Taking the log of both sides,

$$\log(d) = \log(K) + n \log \left( \frac{\sigma}{E} \right)$$ (3.28)

The value of $m_1$ has been chosen such that the secant yield strength, $\sigma_1$ would approximate the yield strength for 0.2 percent offset strain ($\sigma_{0.2}$). Thus, equation (3.26) can be written as:

$$0.002 = \varepsilon - \frac{\sigma_1}{E}$$ (3.29)

Substitute for $\varepsilon = \left( \frac{\sigma_1}{m_1 E} \right)$

$$0.002 = \frac{\sigma_1}{m_1 E} - \frac{\sigma_1}{E}$$ (3.30)

The parameter $m_1$ has been solved for using the equation:

$$\frac{1}{m_1} = \frac{0.002}{\left( \frac{\sigma_1}{E} \right)} + 1 = \frac{0.002}{\left( \frac{\sigma_{0.2}}{E} \right)} + 1$$ (3.31)

The shape parameter "n" has been derived by using second secant yield strength "σ2" corresponding to a second secant modulus $m_2 E$:

$$\varepsilon_2 = \frac{\sigma_2}{m_2 E} = \frac{\sigma_2}{E} + K\left(\frac{\sigma_2}{E}\right)^n \tag{3.32}$$

$$\frac{1}{m_2} = 1 + K\left(\frac{\sigma_2}{E}\right)^{n-1} \tag{3.33}$$

The equations for K and n gives:

$$K = \left(\frac{1-m_2}{m_2}\right)\left(\frac{\sigma_2}{E}\right)^{1-n} \tag{3.34}$$

$$n = 1 + \frac{\log_{10}\left(\frac{m_2}{m_1} \times \frac{(1-m_1)}{(1-m_2)}\right)}{\log_{10}\left(\frac{\sigma_1}{\sigma_2}\right)} \tag{3.35}$$

Figure 3.41 shows the Ramberg-Osgood's non-linear model fitted to the stress strain curve for the pristine SAC305 alloys (representative case). This model provides a good fit for stress strain curve for the uniaxially tested SAC alloys which experiences hardening during plastic deformation. This model is simple to implement with only 3 parameters to describe the complete curve (E, k and n). These experimentally derived parameters can be implemented in the commercial finite element codes to model the SAC alloy based solder interconnect in the PCBs subjected to high strain rates events such as drop and shock tests, vibration tests.
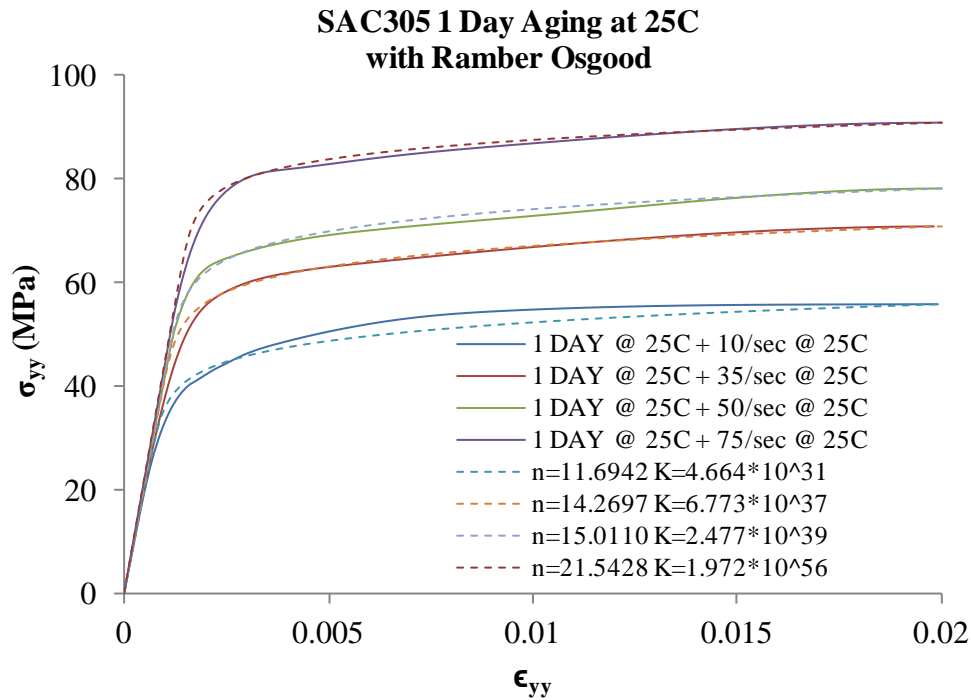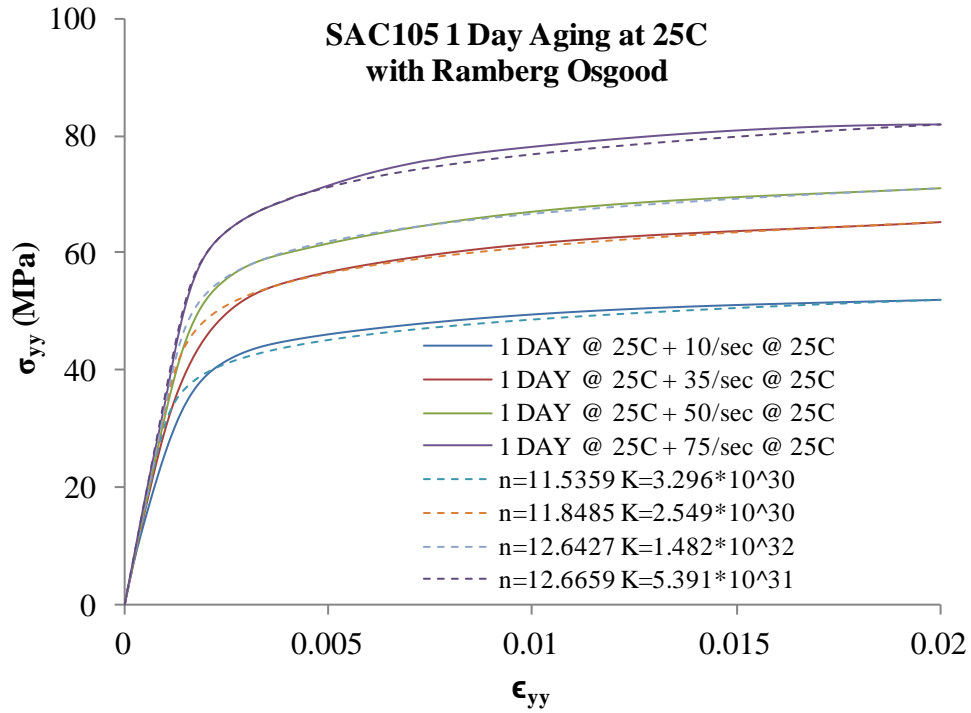
Figure 3.41: Ramberg 0sgood's model for the high strain rate based stress-strain curve for SAC105 and SAC305 alloys.

### 3.10.1 Regression Analysis for the Ramberg-Osgood's Parameters

Regression analysis is performed on the high strain rate data set to extract the shape parameters n and K and compared with the closed form solution method described in the previous section. The co-efficient of determination $R^2$ is compared for both methods for the representative case SAC105solder alloy as shown in Figure 3.42.

**Regression Analysis**
**SAC105 1 Day Aging at 25C**
**with Ramberg Osgood Parameters**

—— 1 DAY @ 25C + 35/sec @ 25C

--- Closed form model E=33.7GPa n=11.8485
K=2.549*10^30 (R-square 0.995)

····· CASE 1 Regression fit E=32.27GPa n=11.94
K=2.55*10^30 (R-square=0.995)

-·-·- CASE 2 Regression fit E=33.7GPa n=12.81
K=1*10^33 (R-square=0.9972)
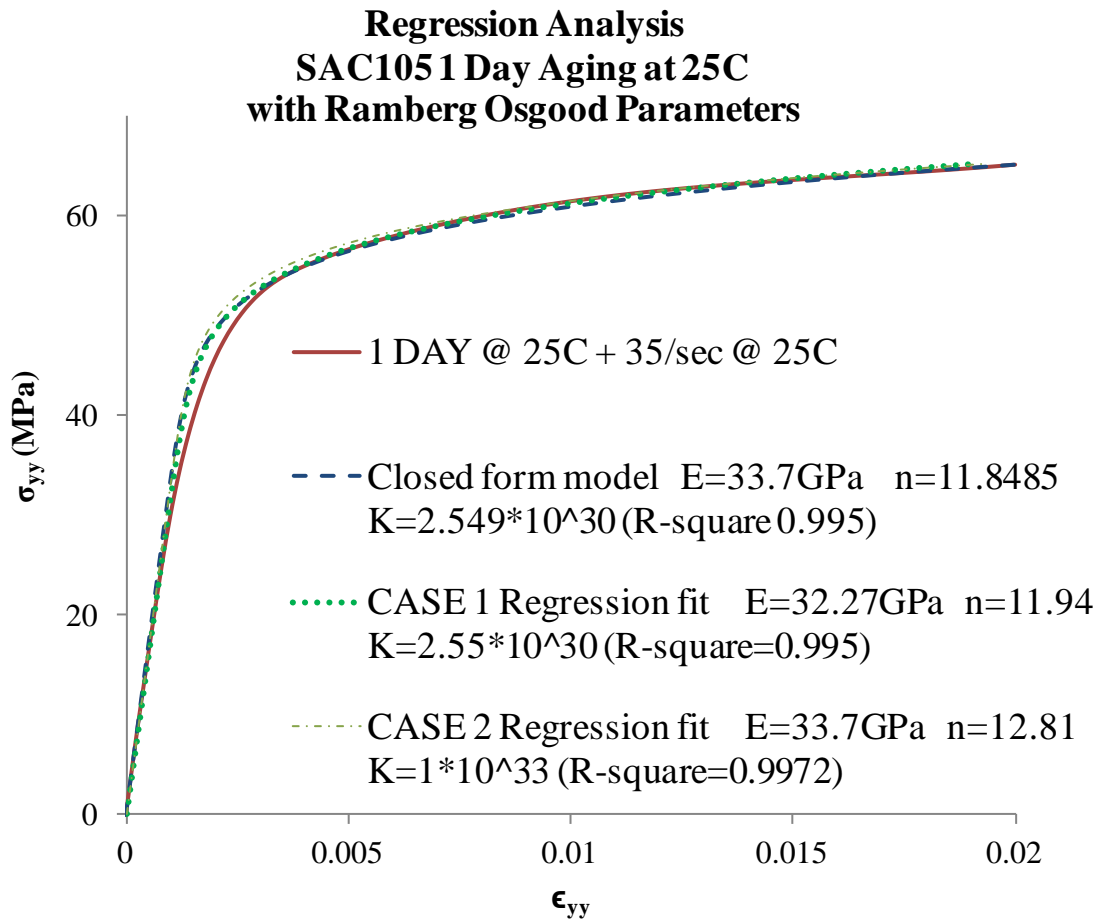
Figure 3.42: Regression Analysis for the high strain rate data of pristine SAC105 tested at strain rate 35sec$^{-1}$

Table 3.45: Regression Analysis for the stress-strain data

(SAC105 1 day aged at 25 C + 35/sec at 25C)

| Closed Form Method R-Square =0.995 | Regression Fit R-Square =0.9972 (Case 2) |
|---|---|
| E=33.7GPa | E=33.7 GPa |
| n=11.8485 | n=12.81 |
| K=2.549E+30 | K=1E+33 |

## 3.11    Digital Image Correlation

Digital image correlation (DIC) technique is used to measure full-field deformation and the derivative of deformation on the axially loaded test specimen. Displacement field quantities are obtained by tracking a geometric point before and after deformation. The tracking is achieved using digital image processing of speckle pattern on the specimen surface. Principle of 2D-DIC is as shown in Figure 3.43. Correlation function implemented in this work is sum of squared difference (SSD),
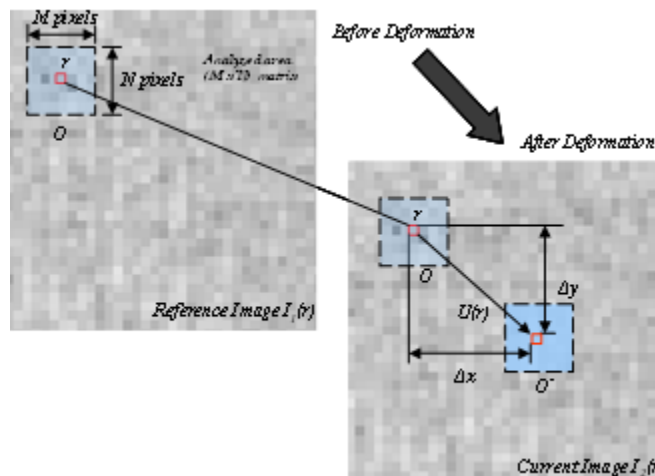


Figure 3.43: 2D- DIC principle

$$C(x, y, u, v) = \sum_{i,j=-\frac{n}{2}}^{\frac{n}{2}} \left(I(x+i, y+j) - I^*(x+u+i, y+v+j)\right)^2 \qquad (3.36)$$

Where, C is the correlation function (SSD), (x, y) are the pixel co-ordinates in the reference image, (u, v) are the displacements, n is the subset size, $I = I1(r)$ = image before deformation, $I^*=$ I2(r) =image after deformation.
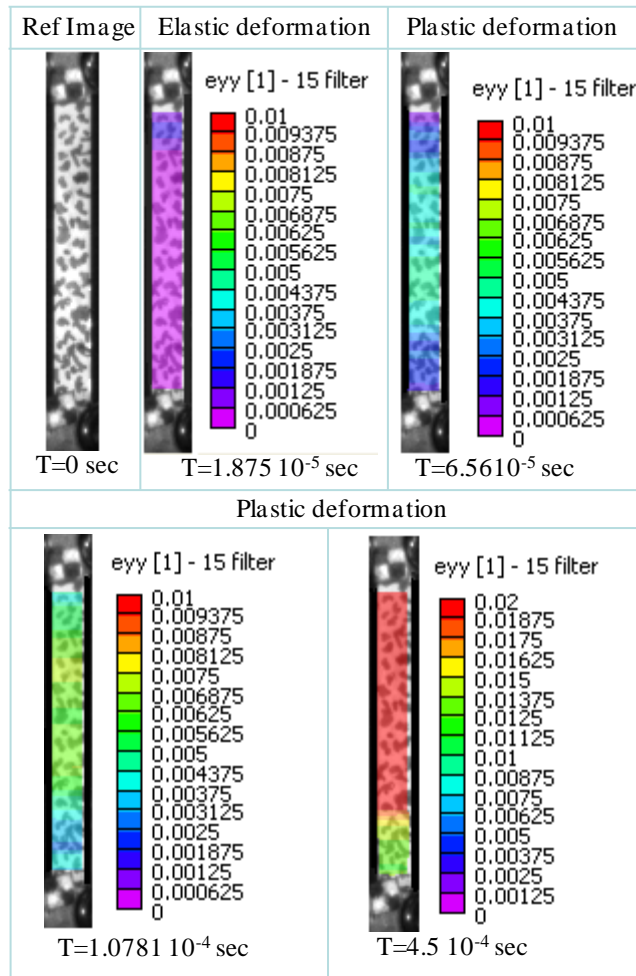


Figure 3.44: Full field axial strain contour of SAC305 (1 DAY @ 25C + 50/s @ 25C) at different time steps

Figure 3.44 provides the full-field strain contour along the axial direction for SAC305 (1day @ 25C + 50/sec @ 25C) test specimen. Cross-head based strain measurement is an average strain value experienced by the entire specimen within the gauge length. However, DIC as mentioned earlier is a full-field strain measurement technique which provides more detail about the specimen deformation which supersedes the conventional strain measuring technique especially during plastic deformation and necking since strain at each location on the specimen starts to vary significantly.

## 3.12   Finite element analysis

Node based modeling techniques is implemented to model the high strain-rate deformation of the solder in uniaxial test. Experimental data has been used to develop boundary conditions for uniaxial tensile testing model. Figure 3.45 shows, node-based modeling approach to simulate uniaxial tensile test. Quasi-static analysis has been implemented as follows:

$$[K]\{D\}_n = \{R^{ext}\}_n \tag{3.37}$$

Where K is the stiffness matrix, D is the degree of freedom vector, and R is the vector of externally applied loads. Plastic deformation in the tensile specimen is addressed using Ramberg-Osgood nonlinear model by introducing yield strength of the material and defining a new parameter $\beta$.

$$\beta = k\left(\frac{\sigma_0}{E}\right)^{n-1} \tag{3.38}$$

Where, $\sigma_0$ is the yield stress, the parameter $\beta$ is fixed in order to have the yield offset equal to the accepted value of strain of 0.2%.
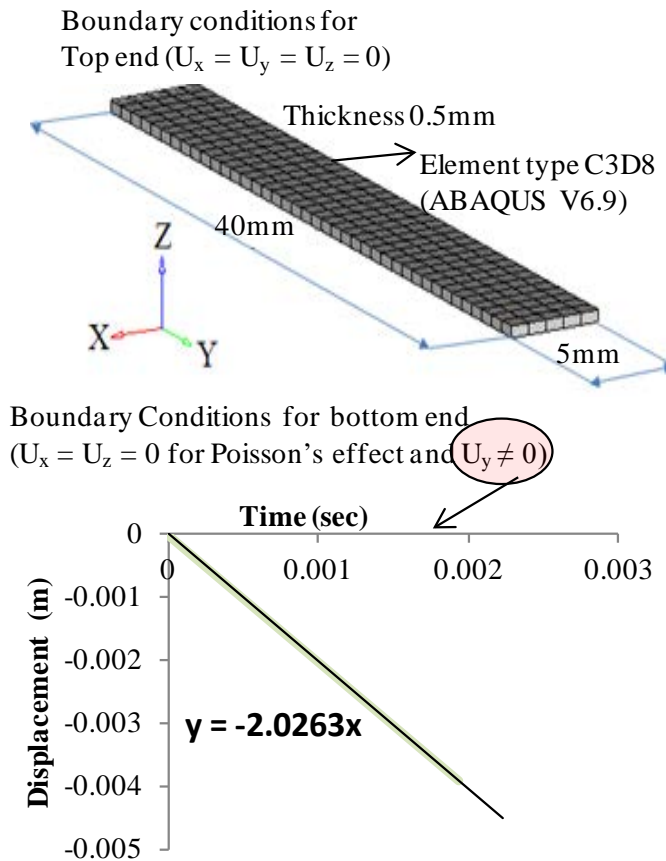
Figure 3.45: Node-based modeling approach

### 3.12.1 Model Validation

Quasi-static strains have been predicted for high strain rate uniaxial tensile test of SAC305 (1 DAY @ 25C + 50/sec @ 25C) using Ramberg-Osgood nonlinear model with shape parameter n=19.62 (Figure 3.41) in abaqusV6.9. Figure 3.46 shows the correlation between simulation based upon Ramberg-Osgood nonlinear plastic deformation model with respect to experimental data for SAC305 1-day aged at 25°C and then tested at 50/sec at 25°C. Figure 3.47 shows the strain contour of the finite element model along specimen pulling direction which correlated reasonably well with DIC which is shown in Figure 3.44.
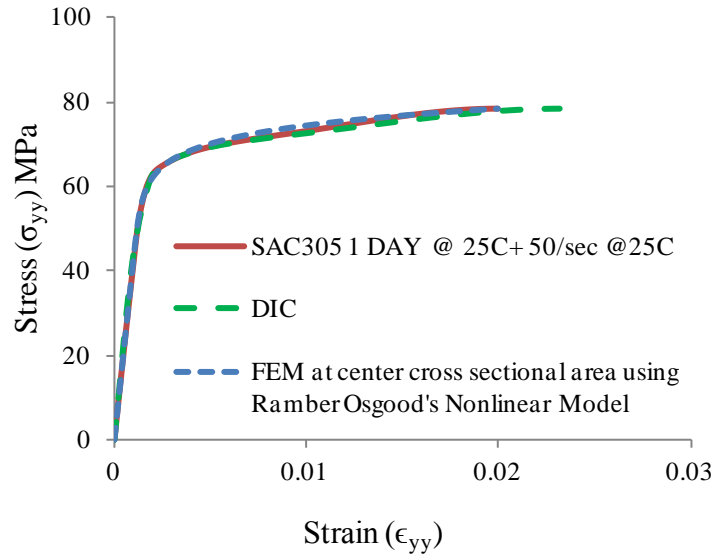
(a)
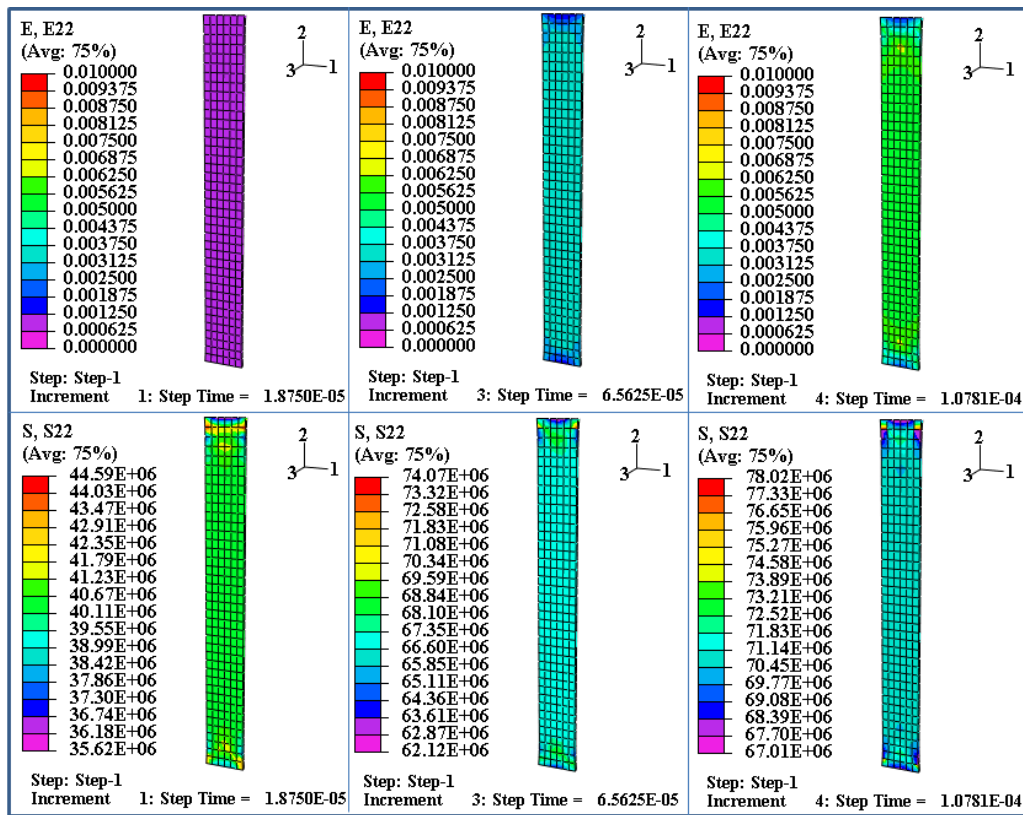


(b)

Figure 3.46: (a) Ramberg Osgood's based simulation vs. experimental Stress-strain data for SAC305 1day @25C+ 50/sec @ 25C (b) Ramberg Osgood's based axial stress-strain contours at discrete time steps
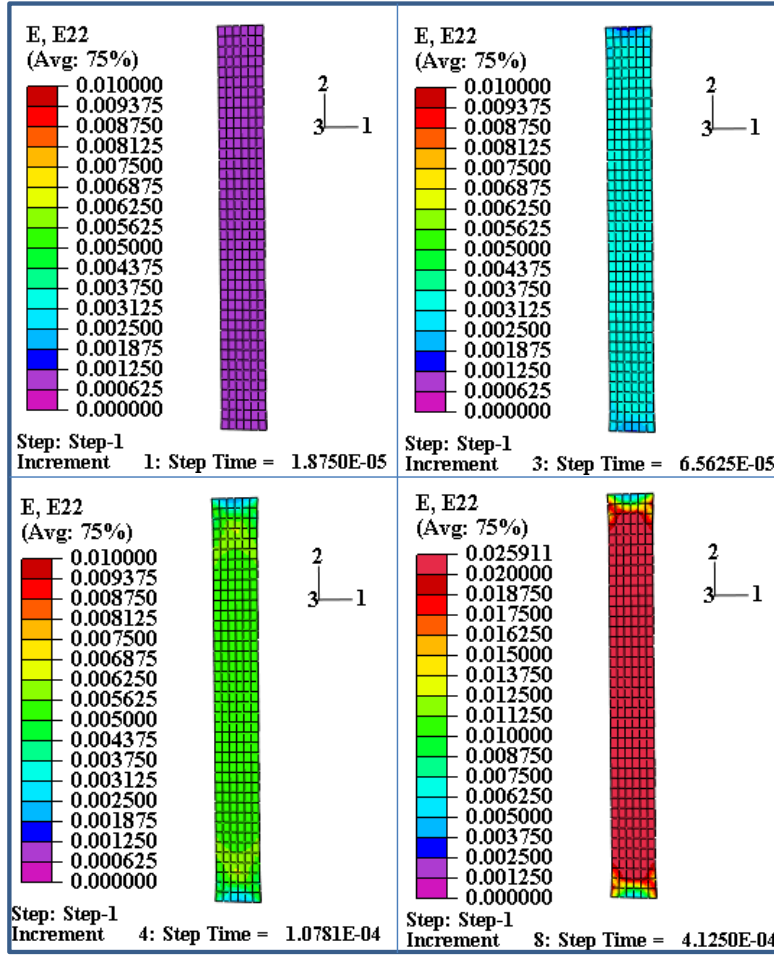
Figure 3.47: Full field axial strain contour of SAC305 (1 DAY @ 25C + 50/sec @ 25C) at different time steps using quasi-static finite element method

# Chapter 4

## Peridynamic-Models using Finite Elements for Leadfree Electronics Subjected to High Strain Rates

### 4.1 Overview

Electronic packages subjected to drop and shock which are high strain rate events have been simulated using alternative theory known as peridynamic theory in the realm of Finite element method. In peridynamics, problems are formulated in terms of integral equation which is a substitute to conventional solid mechanics theory where problems are formulated in terms of partial differential equations. This alternative approach is more potent than conventional finite element method because the integral equations remain valid even at discontinuities which enables to model crack initiation and crack propagation which can occur at multiple locations simultaneously. Previously, Agwai [2008] has demonstrated the use of peridynamic models using EMU code. In this chapter, a peridynamic-theory based drop and shock model has been developed via finite element code using truss elements [Macek 2007]. The method enables the implementation of peridynamic theory in a commercial finite-element platform. Model predictions of peridynamic-models have been validated with experimentation for leadfree solder alloys system.

## 4.2 Peridynamic in Finite Element Framework

Peridynamic theory applies integration scheme rather than differentiation to compute the forces on a material particle. The main objective of this theory is to reformulate mathematical description of solid mechanics so that the same equation is valid on or off a discontinuity such as crack and voids [Silling 2000, 2003, 2005].

Equation of motion is given by

$$\Sigma \vec{F} = m\,\vec{a} \tag{4.1}$$

According to classical continuum mechanics, acceleration of any particle x in the reference configuration at time t is given by

$$\rho \ddot{u}(x,t) = div\sigma + b(x,t) \tag{4.2}$$

Or

$$\frac{\partial \sigma_{XX}}{\partial X} + \frac{\partial \sigma_{XY}}{\partial Y} + \frac{\partial \sigma_{XZ}}{\partial Z} + F_X = \rho \ddot{u}(x,t)_X$$

$$\frac{\partial \sigma_{XY}}{\partial X} + \frac{\partial \sigma_{YY}}{\partial Y} + \frac{\partial \sigma_{YZ}}{\partial Z} + F_Y = \rho \ddot{u}(x,t)_Y \tag{4.3}$$

$$\frac{\partial \sigma_{XZ}}{\partial X} + \frac{\partial \sigma_{YZ}}{\partial Y} + \frac{\partial \sigma_{ZZ}}{\partial Z} + F_Z = \rho \ddot{u}(x,t)_Z$$

Where, Fx, Fy and Fz are body force components per unit volume.

Now,

According to peridynamic theory, acceleration of any particle at x in the reference configuration at time t is given by

$$\rho \ddot{u}(x,t) = \int_{Hx} f(u(x',t) - u(x,t), x'-x)dV_{x'} + b(x,t) \tag{4.4}$$

Where $H_x$ is a peridynamic envelope of radius $\delta$, u is the displacement field vector, b is the prescribed body force density in the reference configuration, and f is the *Pairwise force function* which is equal to force density (per unit volume squared) that x' exerts on x.
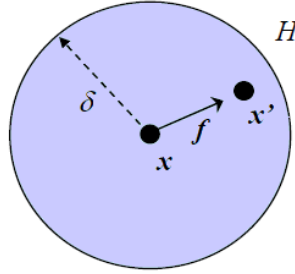


Figure 4.1: Peridynamic body

Relative position of these two particles in reference configuration is given by equation (4.5) with their relative displacements as (4.6).

$$\xi = x' - x \qquad (4.5)$$

$$\eta = u(x', t) - u(x, t) \qquad (4.6)$$

In classical theory, bond extends over finite distance based on the idea of contact forces. But in the case of peridynamic theory, bonds for any given particle do not extend beyond the envelope i.e. particle only interact within the envelope. General form of the bond force for this basic theory is given by

$$f(\eta, \xi) = \frac{\xi + \eta}{|\xi + \eta|} f(y(t), \xi, t) \qquad \forall \xi, \eta \qquad (4.7)$$

Where f is scalar bond force, $\xi + \eta$ represents current relative position vector connecting particles. Peridynamics concept has been implemented in FE code by creating truss elements as mesh with appropriate stiffness properties which represents the peridynamic bonds [Macek 07]. The discretized form of the equation of motion replaces the integral by finite sum as follows

$$\rho \ddot{u}_i^{\,n} = \sum_p f\left(u_p^n - u_i^n, x_p - x_i\right)V_p + b_i^n \qquad (4.8)$$

Where, f is given by (4.7), n is the time step number, and subscript denote the node number, therefore

$$u_i^n = u(x_i, t^n) \qquad (4.9)$$

Where, $V_p$ represents volume of the node p, which for a uniform rectangular grid is simply $\Delta x^\psi$ where $\psi$ is user specified value. The summation is taken over all the nodes p such that $|x_p - x_i| < \delta$. The value of horizon $\delta$ may depend upon the many factors such as nature of the physical problem to be modeled, maximum number of elements which could be possibly created by commercial codes, importance of capturing the complicated cross-sections along boundary in FE model representing the actual physical structure. Multiplying equation (4.8) by $V_i$ leads to equation of motion identical in the form to that of finite element analysis:

$$V_i \rho \ddot{u}_i^{\,n} = \sum_p f(u_p^n - u_i^n, x_p - x_i)V_p V_i + b_i^n V_i \qquad (4.10)$$

$$M \ddot{u}^{\,n} + F_T^n = F_e^n \qquad (4.11)$$

Where M is the lumped mass matrix, $F_e^n$ is the external force vector, and $F_T^n$ is the internal force vector. Each diagonal term of M is $\rho V_i$ and each component of $F_e^n$ is $b_i^n V_i$. Similarly, each component of $F_T^n$ is $\sum_p f(u_p^n - u_i^n, x_p - x_i)V_p V_i$, which is the sum of all the forces from trusses connected to node i. Therefore, creating a truss assembly and providing appropriate stiffness properties for truss elements according to peridynamics theory are the 2 fundamental aspects in order to implement peridynamics in FE code.

## 4.3 Experimental Set-Up

The test specimen has been subjected to controlled high-speed uniaxial tensile test. Figure 4.2 shows the test specimen mounted between the holders and a schematic of 2 high-speed cameras. Figure 4.3 shows the images captured by the high speed cameras from time t = 0 to time t > failure time of the speckle patterned test specimen subjected to high speed uniaxial tensile test.  From these images we note that the rupture occurs closer to centre of the test specimen along cone shaped edge (thickness direction) which forms an angle of approximately 45° to 50° with the original surface of the specimen which in turn indicates that complex state of stress occurs across the failure region of a test material.
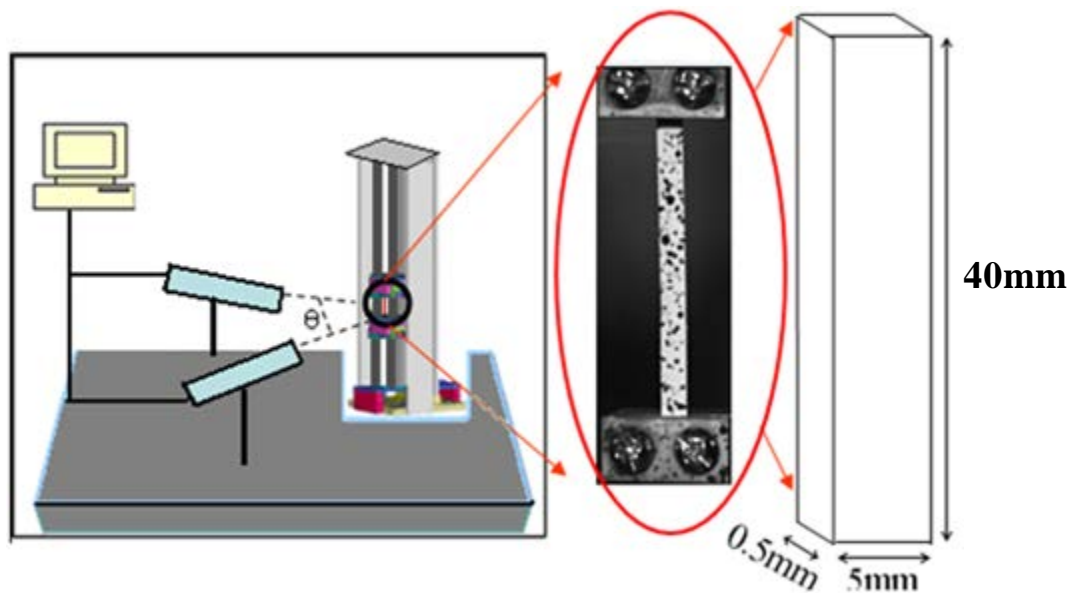


Figure 4.2: High speed uniaxial tensile test for a lead free alloy
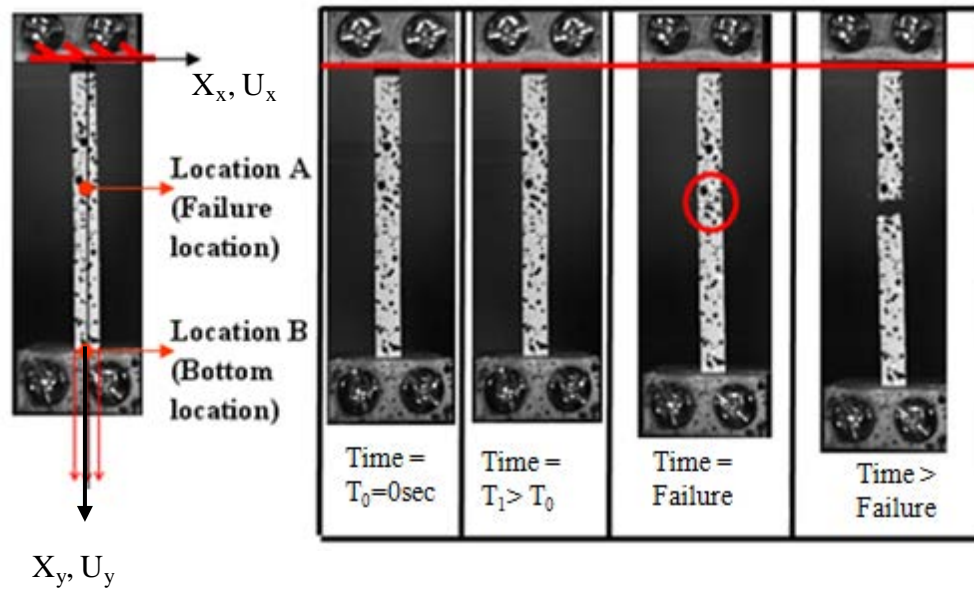
Figure 4.3: Typical images captured by the high speed cameras from time t = 0 to time t > failure time of the speckle patterned test specimen subjected to high speed uniaxial tensile test

3 dimensional digital image correlation (DIC) principle for a truss member is shown in the Figure 4.4. The sub image at time t = 0 is referred as $I_1$ (r) and at time t > 0 is referred as $I_2$ (r) respectively, which are related as follows:

$$I_2(r) = I_1[r - U(r)] \tag{4.12}$$

$$I_1(r) = I_2[r + U(r)] \tag{4.13}$$

Where U(r) is the displacement vector at pixel $r = (x, y, z)^T$.
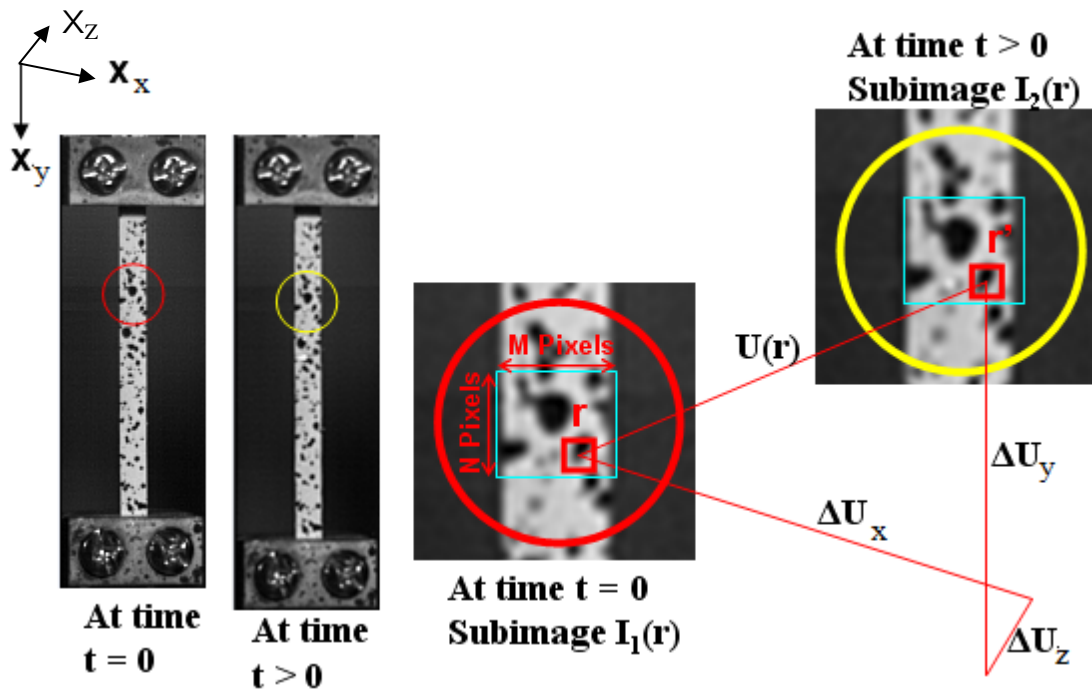


Figure 4.4: 3D-Digital Image Correlation Measurement for a truss member

Figure 4.5 shows the force ($F_Y$) Vs displacement ($U_Y$) curve for test specimen under high strain-rate. Force data is acquired using high-speed force sensors and displacement is computed using DIC technique in conjunction with high speed camera. Stress component ($\sigma_{YY}$) in the test specimen along loaded direction is computed based on the acquired force ($F_Y$) data and original

cross sectional area. Figure 4.6 shows the stress ($\sigma_{YY}$) vs. strain ($\epsilon_{YY}$) curve for the corresponding uniaxial high strain rate tensile test.
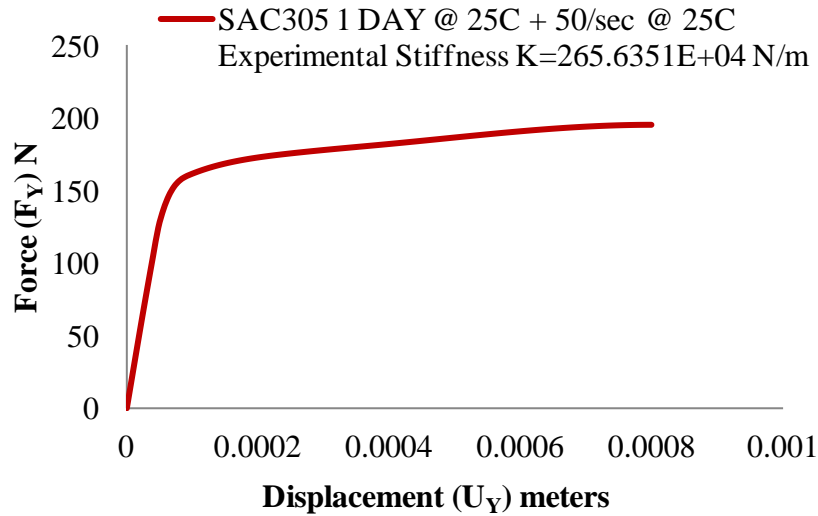


Figure 4.5: Force ($F_Y$) Vs Displacement ($U_Y$) curve for SAC305 1 DAY @25C + 50/sec @ 25C
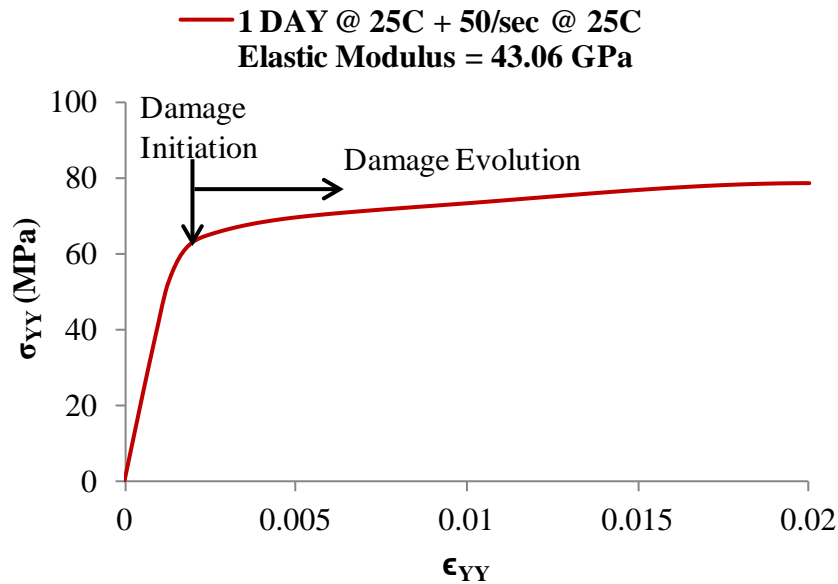


Figure 4.6: Stress Vs Strain curve for SAC305 1 DAY @25C + 50/sec @ 25C

## 4.4 Relationship between Peridynamic and Classic Continuum Mechanics

Consider a large homogeneous body under isotropic extension, now the strain is give by

$$Strain = \varepsilon = \frac{|\xi + \eta| - |\xi|}{|\xi|} = \frac{Bond..Stretch}{Truss..Length} \qquad (4.14)$$

Also,

$$\eta = \varepsilon\xi \qquad (4.15)$$
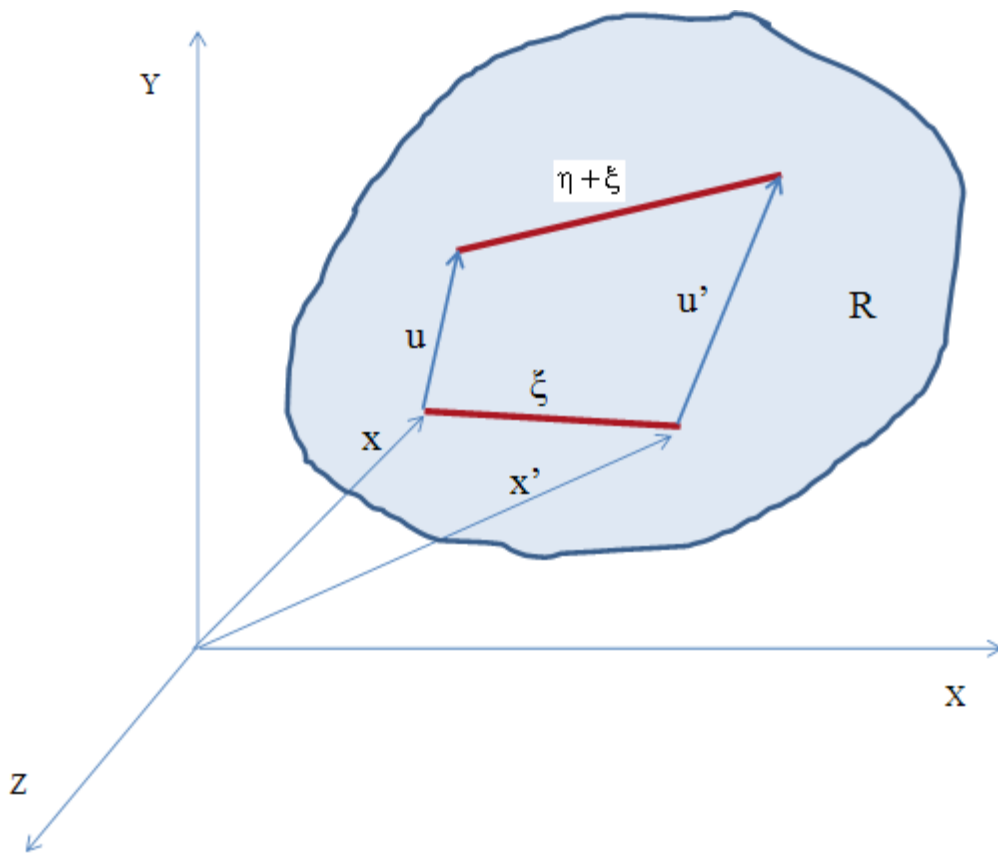


Figure 4.7: Relationships among the variables

Now, pairwise force function is defined as

$$f(\eta,\xi) = \frac{\partial w(\eta,\xi)}{\partial \eta} \qquad (4.16)$$

$$\forall \eta, \xi$$

Where: w=micropotential = Energy in a single bong (Energy per unit volume squared).

$$f = c\varepsilon \tag{4.17}$$

Where c = constant

From equation (4.15) we have

$$f = c\frac{\eta}{\xi} \tag{4.18}$$

Local Strain energy density i.e. energy per unit volume in the body at a given point is

$$W = \frac{1}{2}\int_{H_X} w(\eta,\xi)dV_\xi \tag{4.19}$$

Note; $\frac{1}{2}$ exist because each end point of a bond "owns" only half the energy in the body

Now, from equations 4.15, 4.16 and 4.17 we have

$$W = \frac{1}{2}\int_0^\delta \left(\frac{c\varepsilon^2\xi}{2}\right)dV_\xi \tag{4.20}$$

We know that surface area of the sphere is $4\pi\xi^2$ substituting in 4.20 gives

$$W = \frac{1}{2}\int_0^\delta \left(\frac{c\varepsilon^2\xi}{2}\right).4\pi\xi^2 d\xi \tag{4.21}$$

$$W_{Peridynamics} = \frac{\pi c\varepsilon^2\delta^4}{4} \tag{4.22}$$

Equation 4.22 is required to equal the strain energy density in the classical theory of elasticity for the same material and the same deformation given as

$$W_{ClassicalContinuum} = \frac{9k\varepsilon^2}{2} \tag{4.23}$$

Now combining equations 4.22 and 4.23, we have

$$c = \frac{18k}{\pi\delta^4} \tag{4.24}$$

Where k is the bulk modulus.

**4.5 Peridynamic Model Creation in Commercial Finite Element Plat form**

Peridynamics theory requires creating nodes on concentric circles as shown in Figure 4.8 but for simplicity only uniform rectangular meshes were used for the simulations presented in the work. When we compare rectangular grid generation with respect to circular grid as shown in Figure 4.8, certain percent of nodes get eliminated due to rectangular grid formations which are termed as missing nodes as a result certain degree of accuracy will be lost in the simulation. Firstly, to generate the geometry of the structure a uniform rectangular array of nodes is defined and then trusses are generated by connecting any given node i to any other node p that lies within a sphere of radius $\delta$ centered at node i. Pictorial representation of computation grid with peridynamic envelope is as shown in Figure 4.9. According to the Figure 4.9 trusses of only 2 different lengths can be created, this is done to minimize the number of truss elements suppose to be generated in the commercial FE software.

In order to model the test specimen subjected to uniaxial tensile test '$\delta$' is chosen as $1.4142 \times \Delta x$ where $\Delta x$ represents the rectangular grid spacing as shown in Figure 4.10. Computation time is minimized through coupling peridynamics truss meshes with conventional FEA mesh using embedded nodes and elements which are available in ABAQUS/explicit commercial code [Macek 07]. Element types C3D8R are used as continuum elements. A band of thickness $2\Delta x$ containing conventional continuum elements is defined to overlap the peridynamic trusses. Then these trusses are specified to be embedded in the continuum elements as shown in Figure 4.10. Since the overlap region will become too stiff due to embedded truss elements, elastic modulus and density for the host continuum elements are set to a very small value.
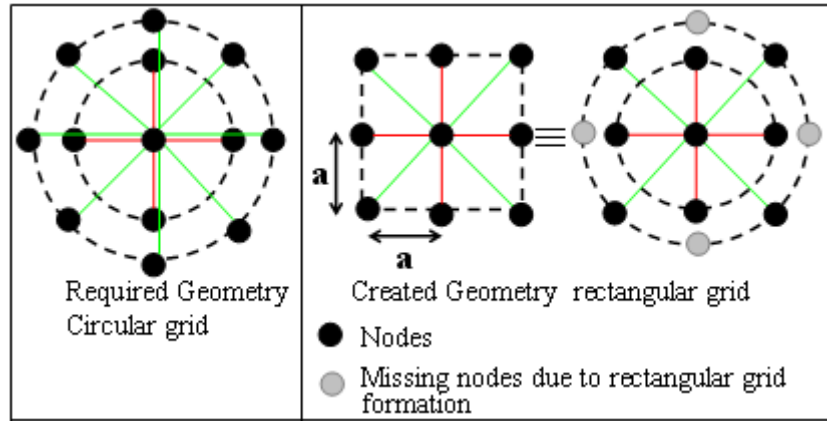
Figure 4.8: Comparison of circular and rectangular grid formation
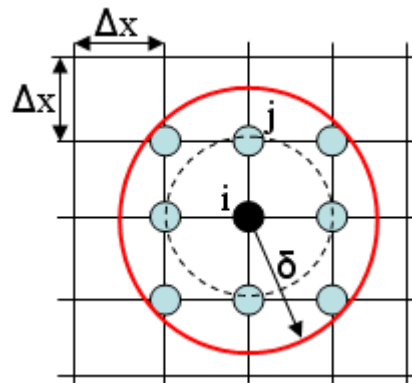


Figure 4.9: Computation grid
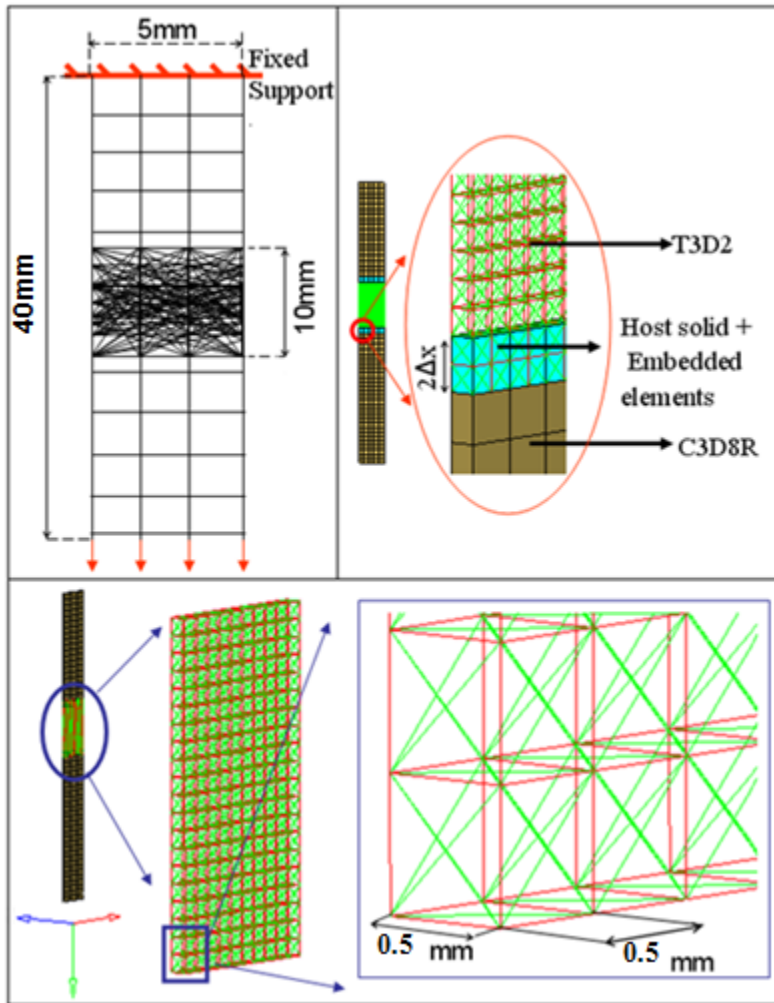
Figure 4.10:  Peridynamics based finite element model (Hybrid model)

In the peridynamics based FE model of the uniaxial tensile test specimen, peridynamic trusses are modeled across the wide central portion of the tensile specimen. This is done to verify the model prediction of the experimental failure region. Boundary conditions are defined via nodes located at the top end of the FE model. Both the translation and rotation d.o.f. of all the nodes located at the top side of the model are constrained in $X_x$, $X_y$ and $X_z$ directions as shown in Figure 4.11.
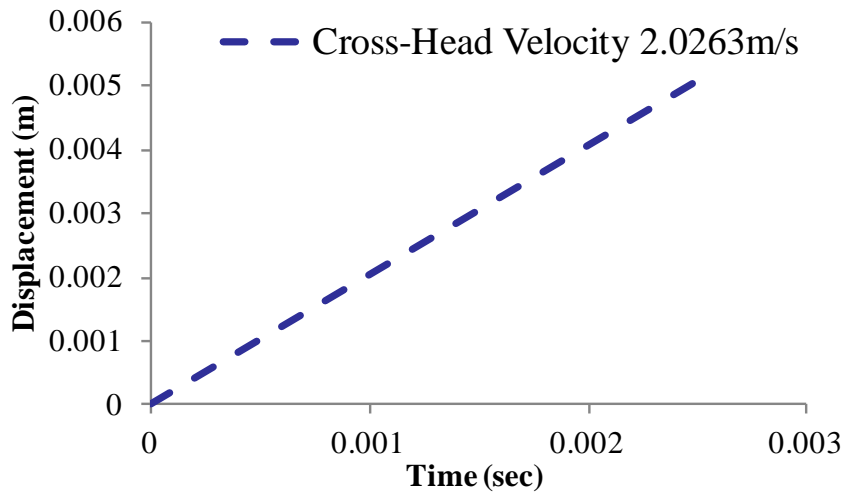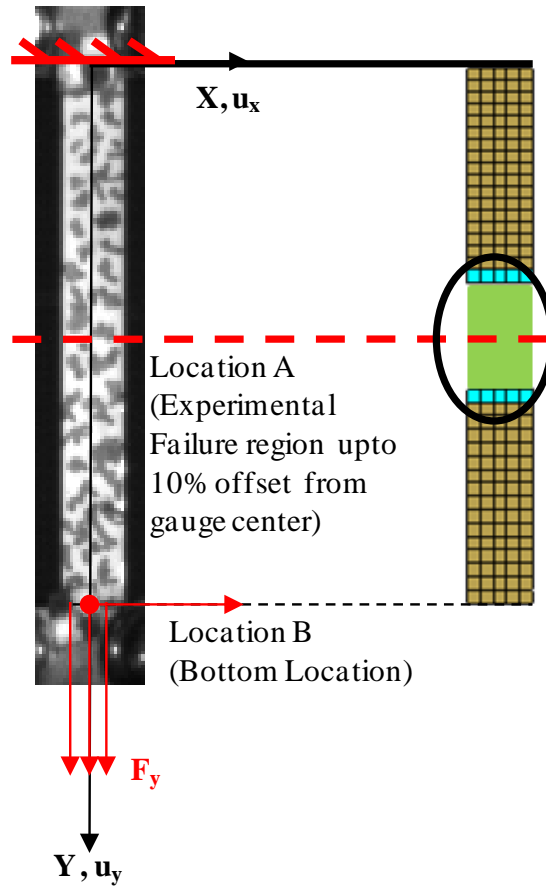
Figure 4.11: Top figure indicates Peridynamics truss region in FE model. Bottom figure indicates displacement data along dropping direction as the input data to the simulation at location B

### 4.5.1 Definition of Section and Material Properties Consistent with Peridynamics Theory

For a uniform rectangular mesh, definition of cross sectional area A and elastic modulus E for trusses are of the form 4.25 and 4.26 respectively [Macek 2007]

$$A_{Peridynamics} = \Delta x^2 m^2 \tag{4.25}$$

Table 4.1 indicates the geometric details of truss elements for modeling uniaxial tensile specimen based on peridynamic approach.

Table 4.1: Geometric details of truss elements

| Truss | $(\Delta x_1)$ Set 1 | $(\Delta x_2)$ Set2 |
|---|---|---|
| Length (L) | 5E-04 m | 7.071E-04 m |
| Cross sectional areas (A) | $A_1 = (5E-4)*(5E-4)= 25E-08m^2$ | $A_2=(5E-4)*(5E-4)= 25E-08m^2$ |

$$E_{Peridynamics} = c \times \Delta x^4 \frac{N}{m^2} \tag{4.26}$$

Where,

$$c = \frac{18}{\Pi} \times \frac{E_{Classic-Continuum}}{3(1-2\upsilon)} \times \frac{1}{\delta^4} \frac{N}{m^6} \tag{4.27}$$

Where, K is the bulk modulus, $\delta$ is the Peridynamic envelope or horizon and has the value of 7.071E-04 m. From Figure 4.6 for SAC305 1 DAY @25C + 50/sec @ 25C we have $E_{ClassicContinuum}$ =43.06 GPa and $\upsilon = 0.25$ (inherent Poisson's ratio for peridynamic theory). Therefore,

$$c = \left( \frac{18}{\Pi} \times \frac{43.06 \times 10^9}{3(1 - 2(0.25))} \times \frac{1}{(7.071 \times 10^{-4})^4} \right) \frac{N}{m^6} \qquad (4.28)$$

Normalization of spring constant 'c' is required if different material particles lie within the peridynamic envelop as follows:

$$c(X) = \frac{c_\infty p_\infty^1}{p^1(X)} \qquad (4.29)$$

Where,

$$P(X) = \frac{\partial}{\partial U} \int_{H_X} f(U, X - x') dV_{x'} \qquad (4.30)$$

thus, $-P(X)\Delta u$ = restoring force (per unit volume) that the particle X experiences if it is displaced incrementally through small vector $\Delta u$ while holding all other points fixed and $c_\infty = c$. In the current modeling approach, test specimen is assumed to be linear, homogeneous and isotropic and hence c will also remain constant. P = symmetric tensor and +ve definite for reasonably behaved materials. It has 3 eigen values $\{P^1, P^2, P^3\}$ and $P^1$ is the largest. $P_\infty$ = Analogous tensor obtained for large homogeneous body and 3 Eigen values $\{P_\infty^1, P_\infty^2, P_\infty^3\}$ with $\{P_\infty^1\}$ is the largest of three. Therefore, we have elastic modulus (E) and corresponding stiffness (K) for two sets of truss elements as shown in Table 4.2. The short range forces are not considered in this simulation since there is no penetration of the one material type into another material type.

Table 4.2: Stiffness of each truss sets based on peridynamic approach

| Truss | Set 1 | Set 2 |
|---|---|---|
| Elastic Modulus (E)<br>$E_{Peridynamics} = c \times \Delta x^4 \dfrac{N}{m^2}$ | $E_1 = 43.06 \text{GPa}$ | $E_2 = 43.06 \text{GPa}$ |
| Stiffness (K)<br>$K = \dfrac{EA}{L} N/m$ | $K_1 = \dfrac{E_1 A_1}{L_1}$<br>$= 2153 \times 10^4 N/m$ | $K_2 = \dfrac{E_2 A_2}{L_2}$<br>$= 1522.4155 \times 10^4 N/m$ |

Finite element model generation will be completed by modifying the elastic modulus of trusses that are within a distance δ of free surface by a normalization factor derived from 4.31. Elastic modulus $E_b(x)$ of an element near a boundary is [Macek 2007]

$$E_b(X) = \frac{p_\infty^1}{p_\infty^1(X)} E_{Peridynamic} \tag{4.31}$$

$$E_b(X) \geq E_{Peridynamic} \tag{4.32}$$

Where $E_b(X)$ is the Elastic modulus near boundary.

Therefore, equation 4.31 can be re-written as

$$E_b(X_i) = \frac{K_{Gauge..Length}}{K_{TRUSS-i}} \times E_i \tag{4.33}$$

Where i = 1, 2 (trusses based on their initial length). Hence, the Elastic modulus has been normalized for trusses of different length. For defining mass for truss element, truss density of bulk-sac305 is used in the simulation instead of setting truss density as zero [Macek 2007] and defining mass of the node via lumped masses as $\rho V_i$.

Failure criteria definition for trusses elements, based upon stress-strain response from Figure 4.13 of SAC305 1 DAY @25C + 50/sec @ 25C test specimen is assumed to be elastic-perfectly plastic [Macek 2007]. From equation 4.14, we have

$$\varepsilon_{PERIDYNAMIC....TRUSS} = \frac{\left|\xi+\eta\right|-\left|\xi\right|}{\left|\xi\right|} = \frac{Bond..Stretch}{Truss..Length} \tag{4.34}$$

Critical Bond Stretch:

$$\Delta L_{CRITICAL} = \varepsilon_{LOCALIZED..FAILURE..REGION} \times Truss..Length \tag{4.35}$$
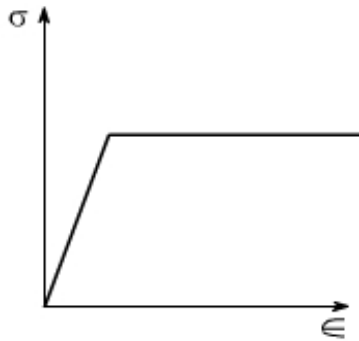


Figure 4.12: Peridynamic trusses modeled as elastic – perfectly plastic
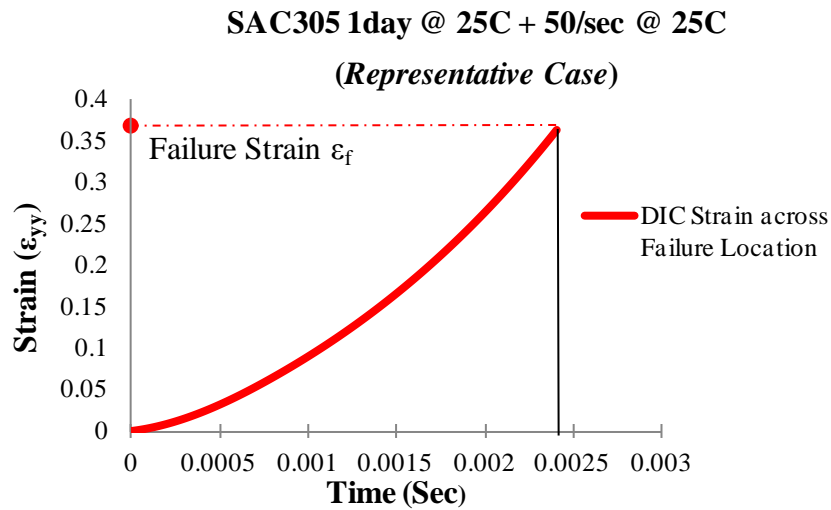


Figure 4.13: Axial Strain values based upon cross head motion and based upon DIC (failure location)

## 4.6 Finite Element Model Peridynamic for High Strain Rate Uniaxial Tensile Test

Figure 4.14 shows the finite element model prediction of the stress field for high-speed uniaxial tensile test specimen at various time steps. Though the axial direction is along y axis, since the trusses has only axial component in Abaqus it is represented as S11. Model predictions have been correlated with high strain rate tension tests. Time to failure and failure mode is accurately captured by FEA based on peridynamic theory and also failure region predicted by FEA is in the vicinity of true failure region (Figure 4.15).
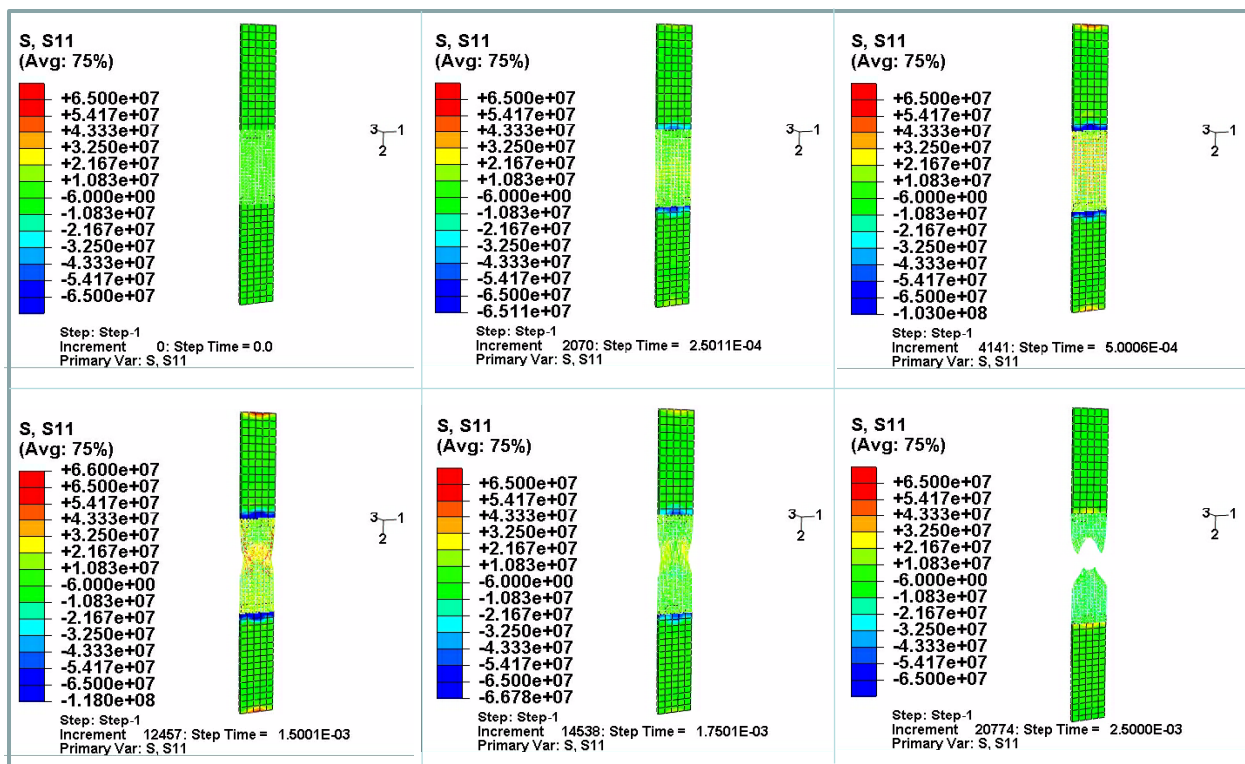


Figure 4.14: Peridynamics based stress field prediction for high-speed uniaxial tensile test at various time steps

| SAC305<br>1 DAY @ 25C + 50/sec @ 25C<br>Complex state of stress near the<br>failure location | Time to failure in sec<br>*(Average failure time<br>2.413E-03 sec)* |
|---|---|
|  | 1.744 E-03 |
|  | 2.42 E-03 |
|  | 2.38E-03 |
|  | 2.56E-03 |
|  | 2.96E-03 |



Step: Step-1
Increment    20774: Step Time =   2.5000E-03
Primary Var: S, S11

Figure 4.15:  Time to failure and failure mode predicted by FEM based on peridynamic theory

## 4.7 Peridynamic Modeling for $0^0$ degree controlled drop test at high G-level

Peridynamic via FEM concept has been extended to model the crack phenomena for printed circuit board assembly subjected to drop impact at high G-levels. Test-board used for experimentation has the dimension 132mm×77mm×1.5mm with one PBGA package located at center of the test board having I/O count of 324 and a pitch of 1mm as shown in Figure 4.16. Detail of the PBGA package architecture is mentioned in the Table 4.3. Test board used in this paper has the unique 4 quadrant continuity design for PBGA package as shown in Figure 4.17. The purpose of this continuity design is to track the in-situ failure location within the package with respect to time as the varying quantity.
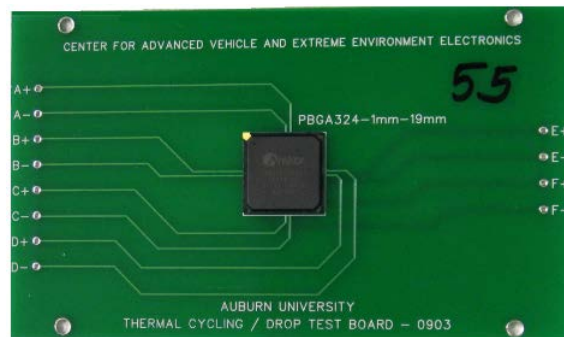


Figure 4.16: PCB (L*B =132* 77mm2 and thickness 1.5mm) and one PBGA-324 package located at centre of the test board
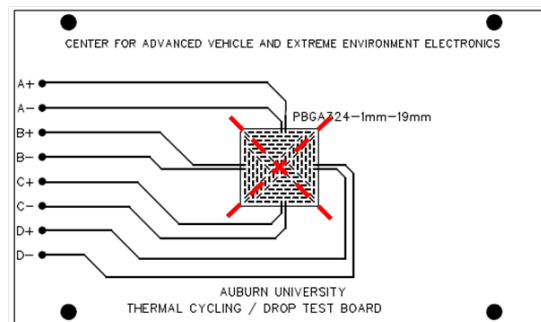


Figure 4.17: Test board showing unique 4 quadrants continuity design for PBGA324 package

130

Table 4.3: Package Architecture of 324 I/O PBGA

|  | 19mm, 324 I/O, PBGA |
| --- | --- |
| Ball Count | 324 |
| Ball pitch (mm) | 1 |
| Die Size (mm) | 7.5 |
| Substrate Thickness (mm) | 0.3 |
| Substrate Pad Type | SMD |
| Ball Diameter (mm) | 0.65 |

The stand-off structure used in this experiment is of 1 inch tall which is taller than the normal stand-off used during JEDEC 0° drop test. The tall stand-off structure ensures free oscillation of PCB without hitting the base (rigid surface) during high G-level tests. Relative movement of the stand-off is also monitored during the actual drop test with single high speed camera to ensure the rigidity of the standoff as shown in Figure 4.18. Also, Figure 4.19 shows the 2 high speed cameras monitoring the drop test of the test board for 3D analysis. Test board was dropped on the impact surface and the corresponding measured acceleration curve is as shown in the Figure 4.20. The peak G value is found to be 12500g's which is will well above JEDEC shock pulse of 1500g's for 0.5ms duration. This high G test will ensure the corresponding board to failure in single drop event.
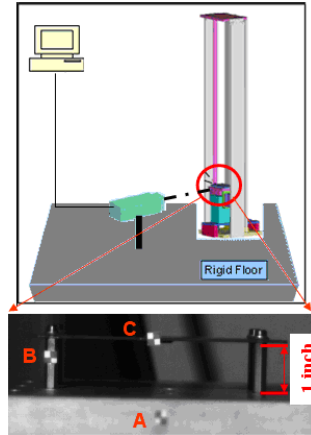
Figure 4.18: Test board with targets A, B, C to measure relative displacements
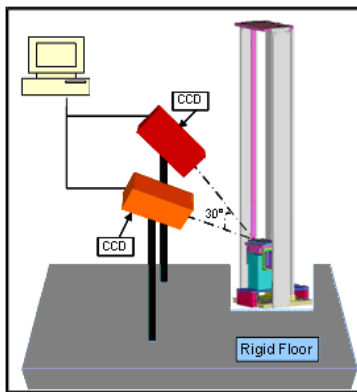


Figure 4.19: 0°-degree drop test setup
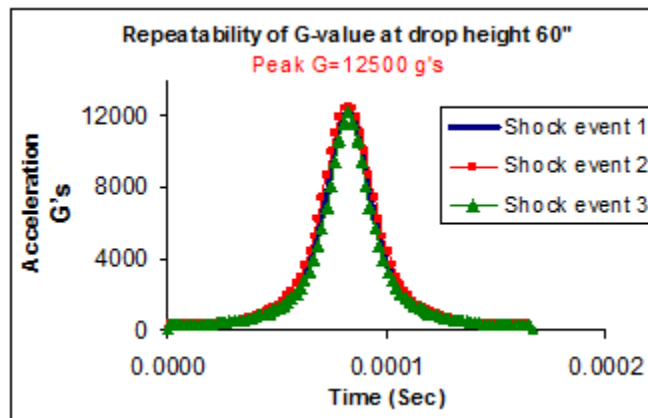


Figure 4.20: Measured acceleration curve corresponding to drop height 60inch

In the Figure 4.21, hatched red and blue regions indicates failure locations of the package during high-G level drop test. For this particular test it has been found that package failure time is below 1 milliseconds. Figure 4.22 shows continuity time histories for this test indicating the failure time for various package sub-regions. The failed package has been cross-sectioned and optical microscope image (Figure 4.23) used to determine failure cites.
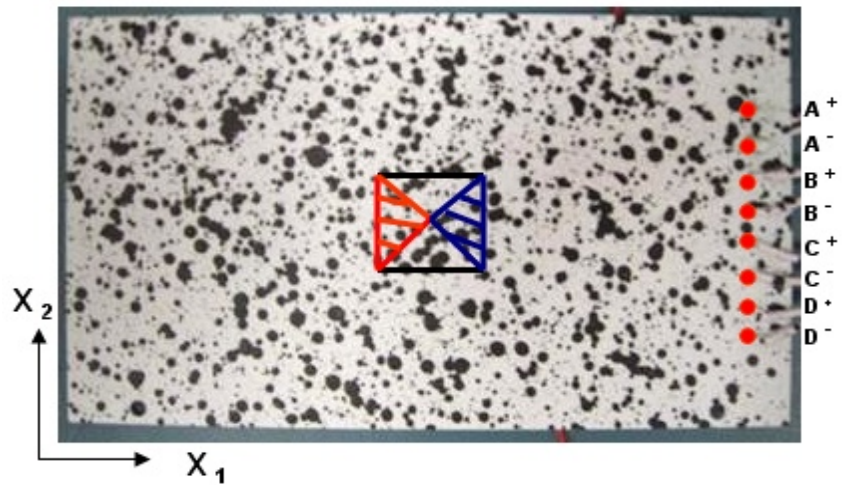


Figure 4.21: Speckle patterned test board indicating failure locations



(a)

(b)
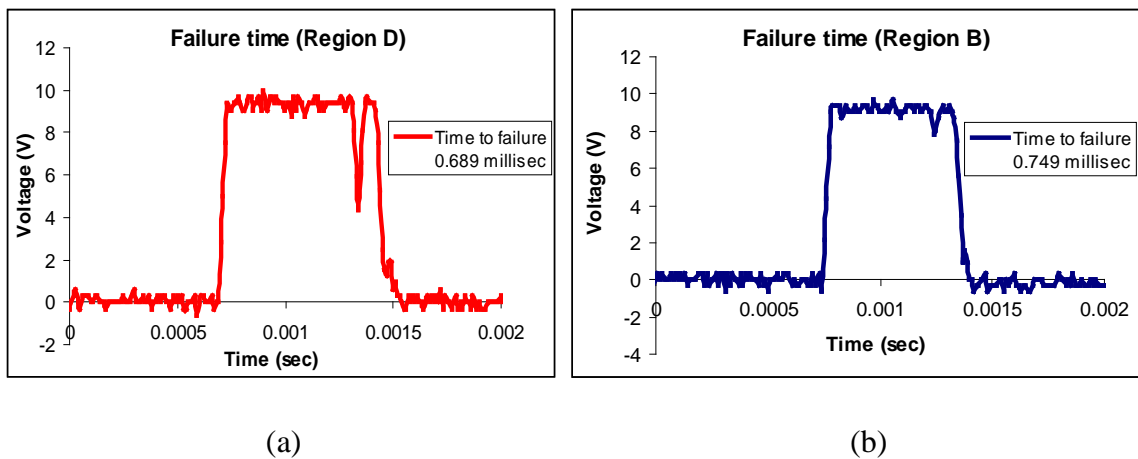
Figure 4.22: (a) and (b) Continuity time history in 0°-drop-shock indicating the failure time for various package sub-regions
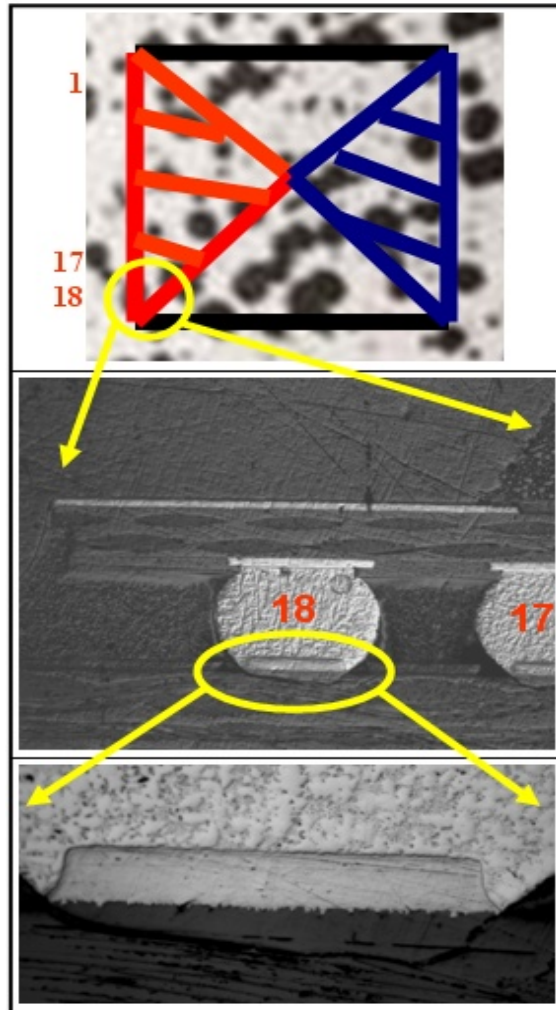
Figure 4.23: Failure on the board side across solder joint

### 4.7.1 Digital Image Correlation for PCB subjected to 0° drop test

3D-DIC measurement concept for a truss member as shown in Figure 4.4 can be expanded to entire PCB assembly subjected to drop and shock [Lall 2009, 2007[c], 2008[d]]. Full-field in-plane 2D strain contour at different time steps has been extracted (*within 1-ms of the drop event* Figure 4.24, *first cycle of the drop event* Figure 4.25). Figure 4.26, provides full field strain rate contour along the board length direction at different time steps. Also, Figure 4.26 shows the location maximum strain rate experienced by the board under compression which is corresponding to the left bottom of the package side which is facing down (not seen in the Figure 4.26).
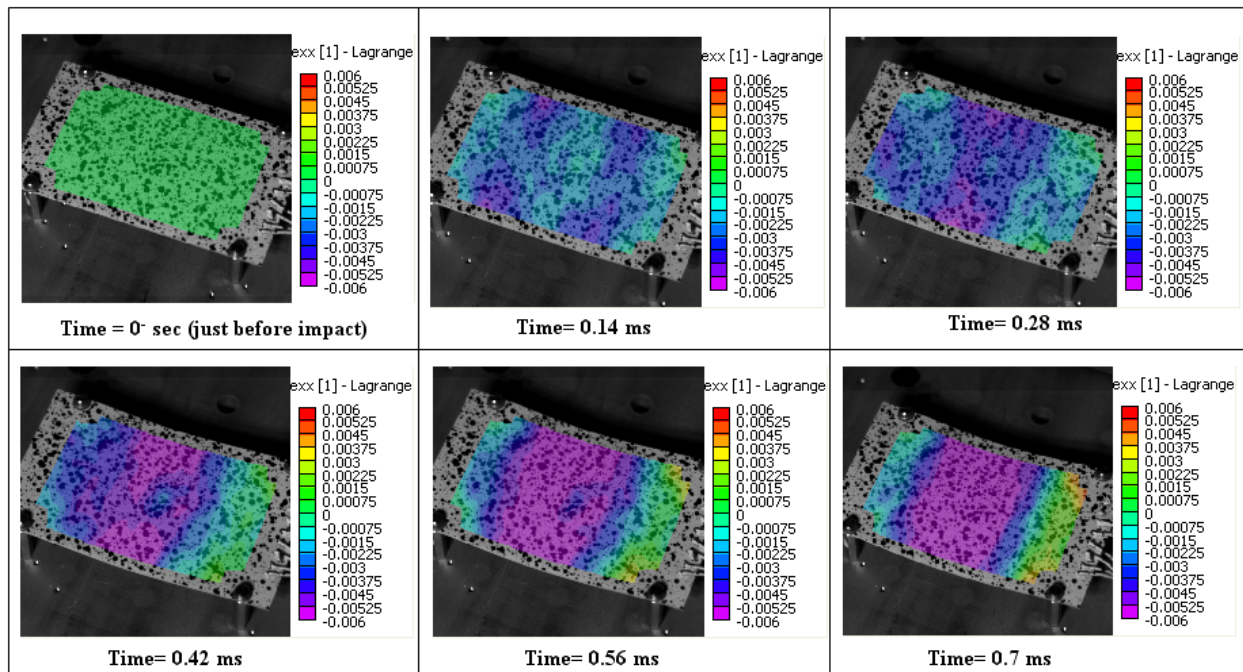


Figure 4.24: DIC based 2D full field strain contour ($\varepsilon_{xx}$) on board (*Within 1-ms of the drop event*)
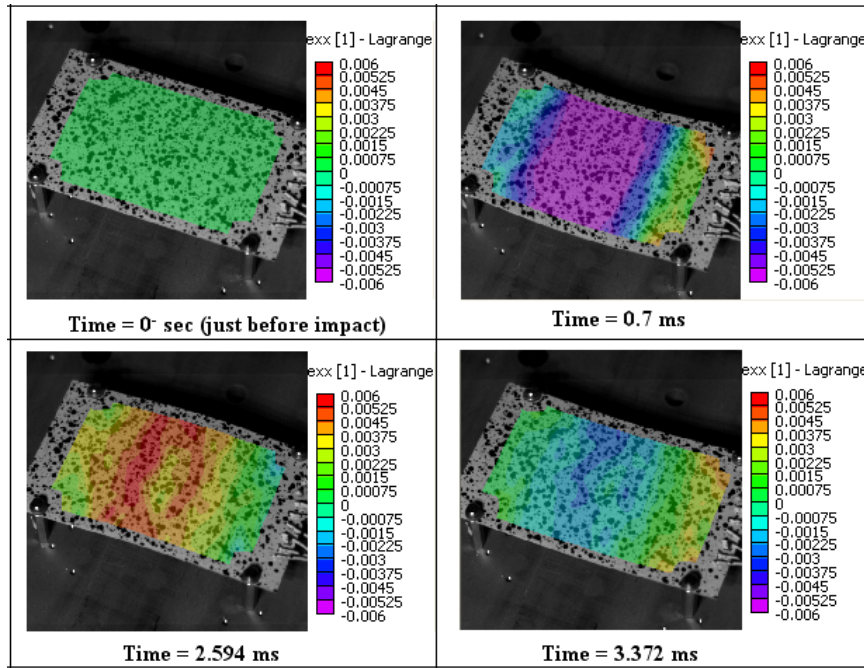
Figure 4.25: DIC based 2D full field strain contour ($\varepsilon_{xx}$) on board (*first cycle of the drop event*)
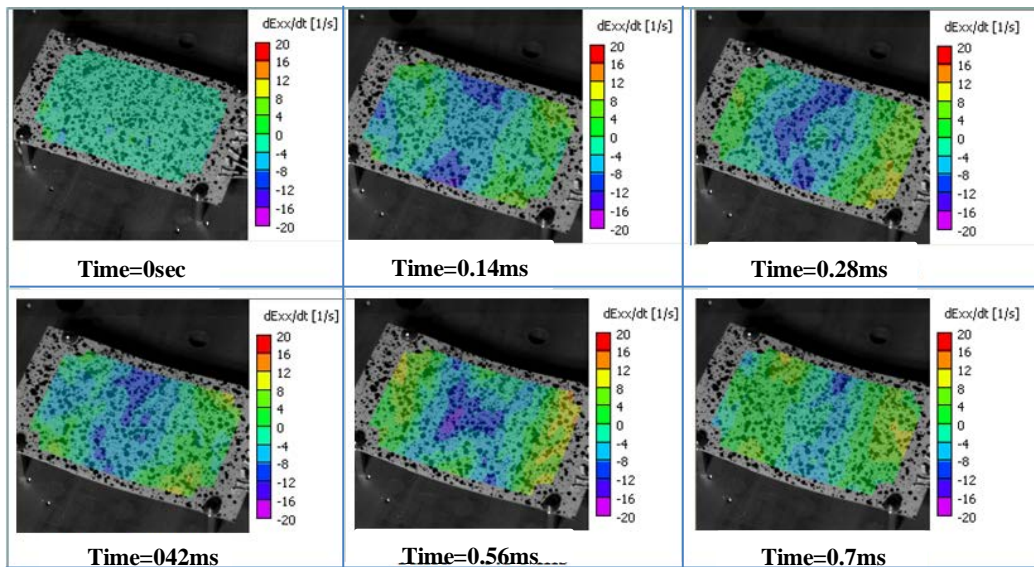


Figure 4.26: DIC based 2D full field strain rate contour ($\varepsilon_{xx}$) on board (*Within 1-ms of the drop event*)
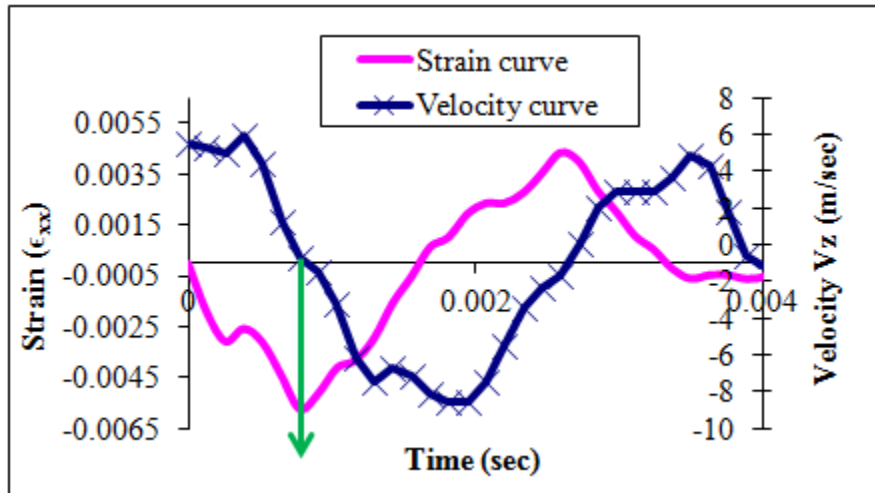
Figure 4.27: Strain ($\varepsilon_{xx}$) along the length of the board at center location and corresponding velocity component in dropping direction

PCB transient strain history ($\varepsilon_{xx}$) at the centre location with the corresponding velocity time history for this drop test is shown in Figure 4.27. In the same plot green arrow indicates that the board is undergoing maximum compression at zero velocity as expected.
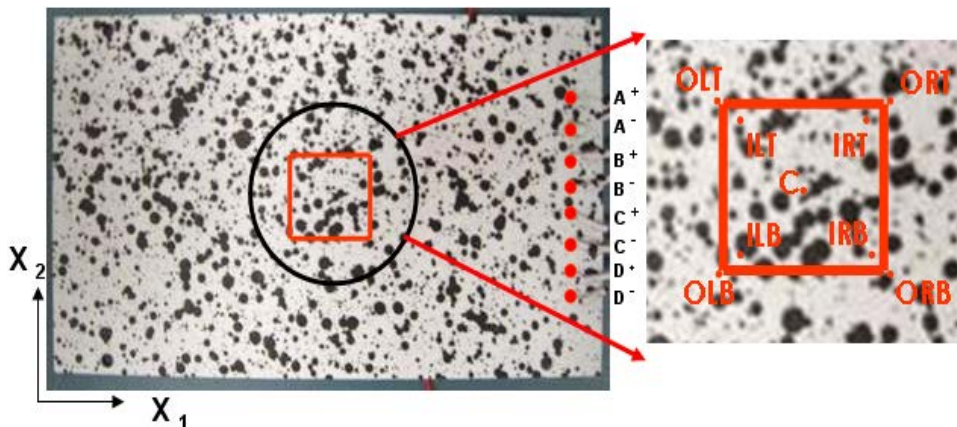


Figure 4.28: Speckle patterned test board indicating discrete locations where velocity components (V3) are being extracted using DIC technique

Figure 4.29 shows relative velocity vectors extracted from DIC at discrete locations of the test board. Specific locations have been identified by OLT: outer left top; ILT: inner left top; ORT: outer right top; IRT: inner right top; ORB: outer right bottom; IRB: inner right bottom; OLB: outer left bottom; C: center. These experimentally extracted data will be implemented in the FE analysis as initial and boundary conditions [Lall 2009].
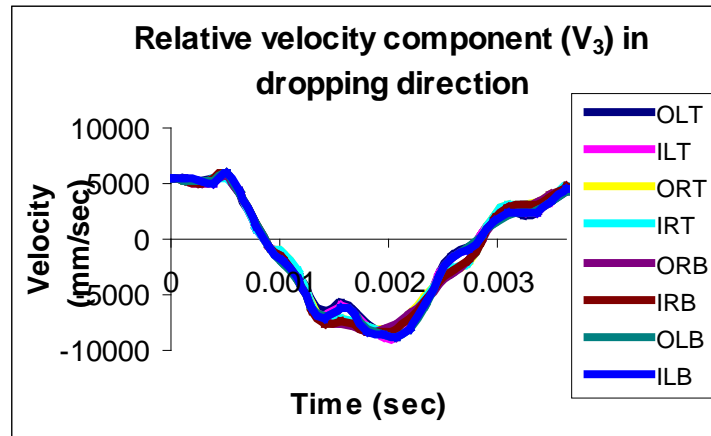


Figure 4.29: Velocity (V3) components along dropping directions of the board at 8 discrete locations using DIC technique

## 4.7.2 Peridynamics based FEA of Electronic Package Subjected to Drop Test

Simulation of the PCB assembly drop test has been carried out using peridynamic approach within FE code. Coupling of FE and peridynamic scheme is retained to reduce the computational time [Macek 2007]. Hybridization of the conventional finite elements with peridynamics trusses modeling concept for uniaxial tensile test has been expanded to simulate the PCB assembly drop and shock event. Figure 4.30 shows peridynamic based FE modeling concept for electronic package across the solder interconnect interface. All corner solder interconnects region has been chosen to be the peridynamic truss region since they are the weakest link in the entire PCB assembly [Lall 2005]. Peridynamic truss region has been deployed on both PCB-solder and

substrate-solder side in order to simulate multiple failure modes such as cracks between copper and solder on package side as well as board side, bulk solder failure, cracks between PCB and solder. This model contains two set of trusses similar to peridynamics based uniaxial tensile test simulation but with the different dimension. Truss lengths modeled for peridynamic region across solder interconnect is mentioned in the Table 4.4. Elastic modulus (E) for different layers of truss region has been derived similar to the peridynamic Elastic modulus calculation implemented for truss region under uniaxial tensile test. Figure 4.31 shows the 3D view of the peridynamics based truss elements across the solder interconnect interface with dotted line representing truss regions.

Table 4.4: Truss lengths for solder interconnect

| Truss Set 1 | Length = $X_1$ = 0.045E-03 m |
|---|---|
| Truss Set 2 | Length = $X_2$ = 0.045E-03 m |
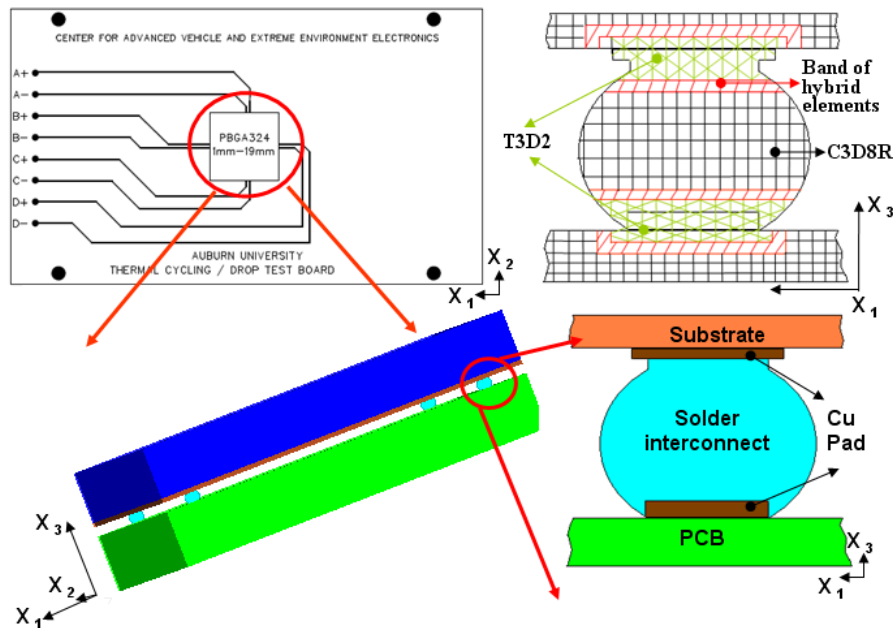


Figure 4.30: Peridynamic based FE Modeling concept for electronic package across the solder interconnect interface

139
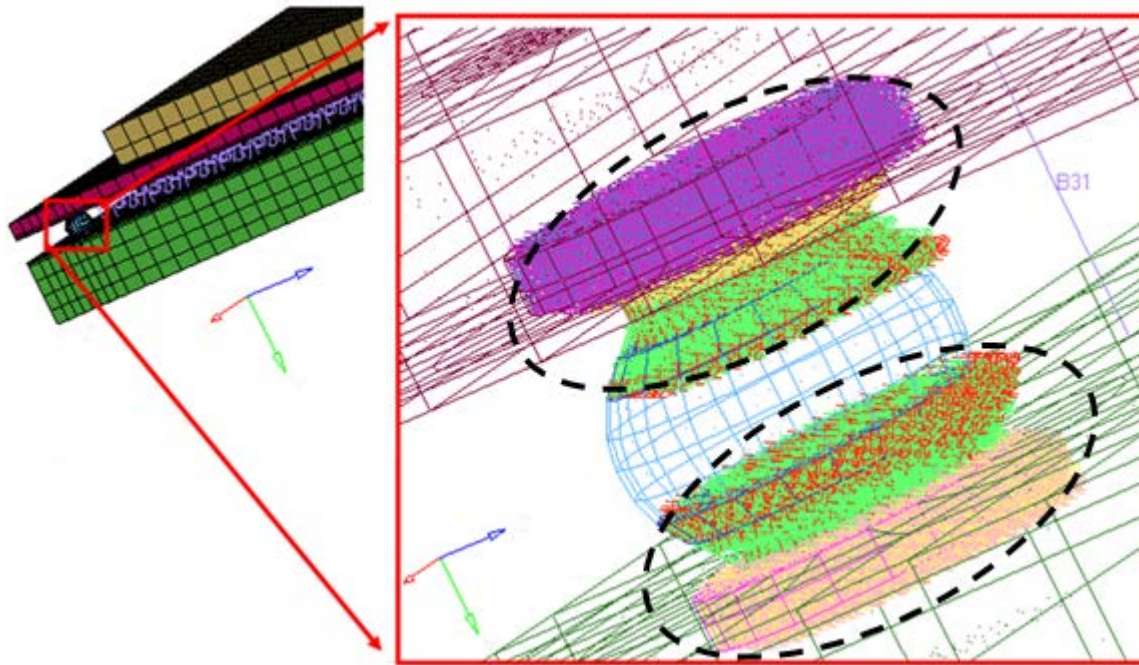
Figure 4.31: 3D view of the peridynamics based truss elements across the solder interconnect interface (*elements with in dotted ellipse represents peridynamic truss region*

### 4.7.3  FE Model Prediction and Correlation with Experimentation

Figure 4.32 shows the location of peridynamic based solder interconnects in the finite element model. All the four corners of PBGA are modeled using peridynamic truss elements. Figure 4.33 shows the damage initiation and damage progression across the left bottom (LB) solder interconnect at various time steps. For the LB solder interconnect which is residing in the red hatched region damage is predicted between the time interval 0.6ms to 1ms and in the actual drop event red hatched region failure time is 0.7ms.
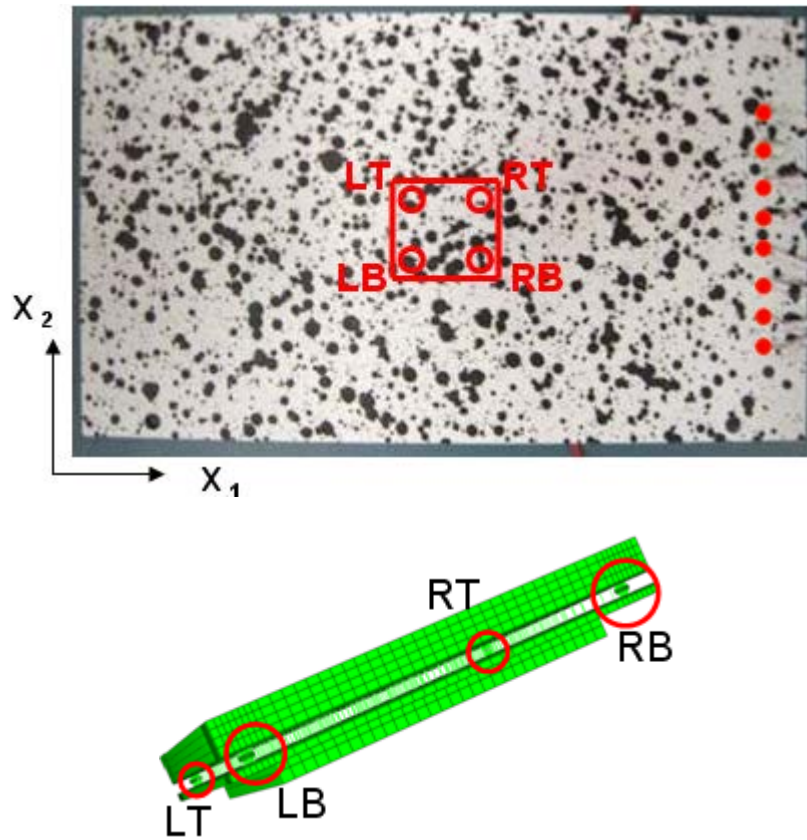
Figure 4.32: corner solder balls locations represented as LT, RT, RB and LB

This shows the capability of the peridynamic FE modeling approach to predict the damage initiation and damage progression for extremely loaded structures. Mostly for all the corner solder interconnects damage initiates between solder and board side. This is expected since experimentally board has failed with in 1ms from the point of impact (i.e. before board reaching maximum compression state).
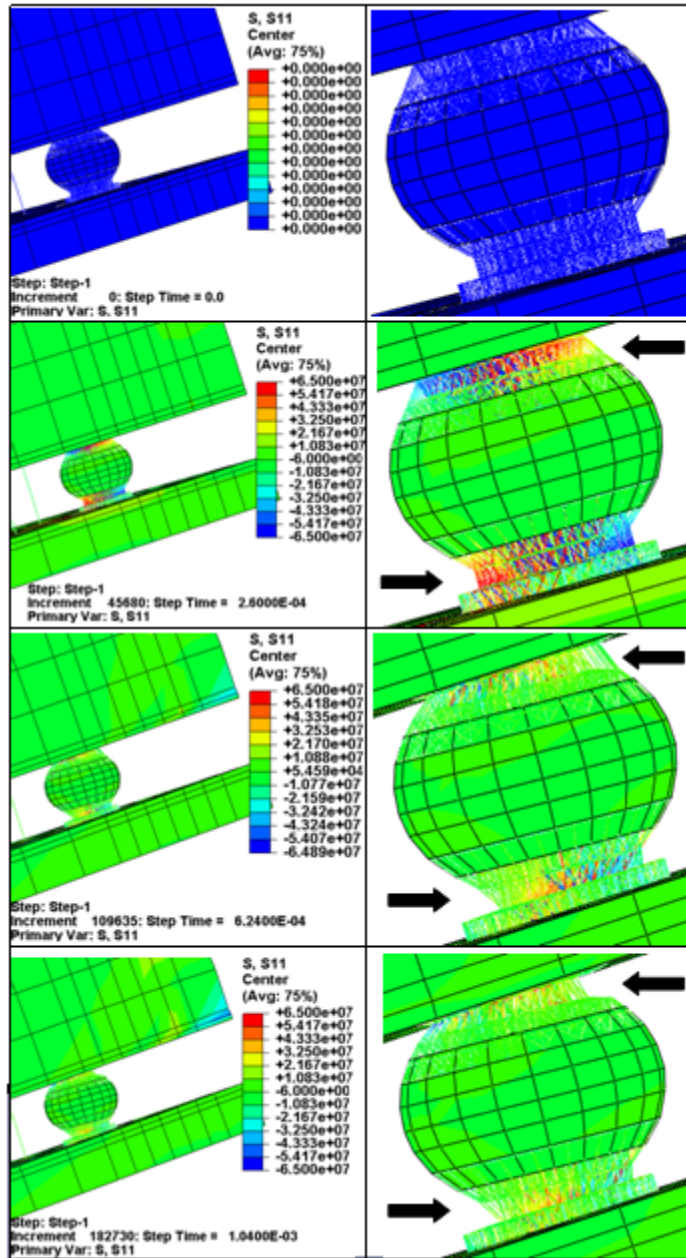
Figure 4.33: Damage initiation and damage progression across left bottom (LB) solder interconnect on board side

## Summary

In this work author  has developed a new method for characterizing materials at constant high strain rates in the neighborhood of 1 to 100 per sec. Uniaxial tensile tests for lead-free SAC solder specimen were carried out at 4  high strain rate events (10, 35, 50 and 75 per sec ). Material properties and failure thresholds have been derived from high-strain rate uniaxial tension test. High-speed imaging and DIC based full-field strain measurement on the SAC solder specimen were carried out. Material properties of SAC solder alloys subjected to elevated aging temperatures were compared with pristine samples. Non-linear Ramberg-Osgood model's parameters for the solder alloys were extracted from experimentation and implemented in finite element frame work. Also, a detailed procedure of a simple uniaxial high speed tensile test simulation based on peridynamic approach has been provided. Peridynamic modeling concept has been extended to simulate damage phenomena for the electronic package subjected to controlled drop test. Material properties and failure thresholds have been derived from high-strain rate uniaxial tension tests. In addition, high-speed imaging and DIC measurements on board assemblies have been used to measure the initial and boundary conditions for explicit time integration scheme. Peridynamic based FE analysis of the board assembly has been used to predict the failure location in the second-level solder interconnects. Measurements show that FE based peridynamics is a useful technique to predict damage initiation and damage progression for various test boards with ball-grid array package architecture under extreme high-G loading situations.

# Reference

Abaqus 6.9-1 Documentation, Section 28.5.3: Modeling with cohesive elements, 2009a.

Abaqus 6.9-1 Documentation, Section 10.6.1: Modeling discontinuities as an enriched feature using the extended finite element method, 2009b.

Abtew, M., and Selvaduray, G., "Lead-free Solders in Microelectronics," Materials Science and Engineering: R: Reports, Vol. 27, pp. 95-141, 2000.

Agwai, A., Guven, I., Madenci, E., Peridynamic Theory for Impact Damage Prediction and Propagation in Electronic Packages due to Drop, 58th Electronic Components and Technology Conference, pp. 1048-1053, Lake Beuna Vista, Florida, 2008.

Amodio, D., Broggiato, G., Campana, F., Newaz, G., Digital Speckle Correlation for Strain Measurement by Image Analysis, Society for Experimental Mechanics, Vol. 43, No. 4, December 2003.

Belytschko, T., Black, T., Elastic crack growth in finite elements with minimal remeshing, International Journal for Numerical Methods in Engineering Volume 45 Issue 5, pp. 601-620, April 1999.

Cadge, D., Reid, D., Krishna, S., Advancements in fracture and failure simulation for electronic package application, Microelectronics and Packaging Conference (EMPC), 18th European, 2011.

Cai, Z., Reduction of Lead Free Solder Aging Effects Using Doped SAC Alloys, Dissertation, 2012. http://etd.auburn.edu/etd/handle/10415/3368.

Chan, D., Nie, X., Bhate, C., Subbarayan, G., Dutta, I., High Strain Rate Behavior of Sn3.8Ag0.7Cu Solder Alloys and Its Influence on the Fracture Location Within Solder Joints, 3rd International Conference on Energy Sustainability, ASME InterPACK, San Francisco, California, USA, pp 989-995, July 19–23, 2009.

Chong, D.Y.R., Toh, H.J., Lim, B.K., Low, P. T.H., Drop Reliability Performance Assessment for PCB Assemblies of Chip Scale Packages (CSP), Electronic Packaging Technology Conference, pp. 262-269, June, 2005.

Chuang, C. M., Liu, T. S., Chen, L. H., Effect of Aluminum Addition on Tensile Properties of Naturally Aged Sn-9Zn Eutectic Solder, *Journal of Materials Science*, Vol. 37(1), pp. 191-195, 2002.

Cook, R., Malkus, D., Plesha, M., Witt, R., Concepts and Applications of Finite Element Analysis, 4th edition, John Wiley and Sons, Inc, 2005.

Coyle, R. J., Solan, P. P., Serafino, A. J., and Gahr, S. A., The Influence of Room Temperature Aging on Ball Shear Strength and Microstructure of Area Array Solder Balls, Proceedings of the 50th Electronic Components and Technology Conference, pp. 160-169, 2000.

Darveaux, R., Shear Deformation of Lead Free Solder Joints, Proceedings of the 55th Electronic Components and Technology Conference, pp. 882-893, 2005.

Ding, Y., Wang, C., Tian, Y., and Li, M., "Influence of Aging on Deformation Behavior of 96.5Sn3.5Ag Lead Free Solder Alloy During In Situ Tensile Tests," *Journal of Alloys and Compounds*, Vo. 428, pp. 274-285, 2007.

Han, P., Tensile Testing, ASM International, June 1992.

Hsuan, T. C., and Lin, K. L., Effects of Aging Treatment of Mechanical Properties and Microstructure of Sn-8.5Zn-0.5Ag-0.01Al-0.1Ga Solder, Materials Science and Engineering, A 456, pp. 202-209, 2007.

JESD22-B111, Board Level Drop Test Method of Components for Handheld Electronic Products, JEDEC SOLID STATE TECHNOLOGY ASSOCIATION, July 2003.

Jenq, S., T., Chang, H., Lai, Y., Tsai, T., "High strain rate compression behavior for Sn–37Pb eutectic alloy, lead-free Sn–1Ag–0.5Cu and Sn–3Ag–0.5Cu alloys," Microelectronics reliability 49, pp 310-317, 2009.

Kaminishi, K., Sekine, T., Maruichi, T., Osaki,S., *Trans. Jpn. Soc. Mech. Eng.* 70, 90. 2004.

Kim, K., S., Huh, S., H., Suganuma, K., "Effects of cooling speed on microstructure and tensile properties of Sn–Ag–Cu alloys," Materials Science and Engineering A333,pp 106–114, 2002.

Lall, P., Shantaram, S., Suhling, J., Effect of Aging on the High Strain Rate Mechanical Properties of SAC105 and SAC305 Leadfree Alloys, ECTC, pp 1277-1293, 2013.

Lall, P., Kulkarni, M., Angral, A., Panchagade, D., Suhling, J., Digital-Image Correlation and XFEM Based Shock-Reliability Models for Leadfree and Advanced Interconnects, Proceedings of the 60th ECTC, pp. 91-105, 2010.

Lall, P., Shantaran, S., Angral, A., Kulkarni, M., Explicit Submodeling and Digital Image Correlation Based Life-Prediction of Leadfree Electronics under Shock-Impact, 59th ECTC, San Diego, CA, pp. 542-555, May 25-29, 2009.

Lall, P., Choudhary, P., Gupte, S., Suhling, J., Health Monitoring for Damage Initiation and Progression during Mechanical Shock in Electronic Assemblies, IEEE Transactions on Components and Packaging Technologies, Vol. 31, No. 1, pp. 173-183, March 2008a.

Lall, P., Panchagade, D., Choudhary, P., Gupte, S., Suhling, J., Failure-Envelope Approach to Modeling Shock and Vibration Survivability of Electronic and MEMS Packaging, IEEE Transactions on Components and Packaging Technologies, Vol. 31, No.1, pp. 104-113, March 2008b.

Lall, P., Iyengar, D., Shantaram, S., Pandher, R., Panchagade, D., Suhling, J., Design Envelopes and Optical FeatureExtraction Techniques for Survivability of SnAg Leadfree Packaging Architectures under Shock and Vibration, Proceedings of the 58th Electronic Components and Technology Conference (ECTC), Orlando, Florida, pp.1036-1047, May 27-30, 2008d.

Lall, P., Gupte, S., Choudhary, P., Suhling, J., Solder-Joint Reliability in Electronics Under Shock and Vibration using Explicit Finite Element Sub-modeling, IEEE Transactions on Electronic Packaging Manufacturing, Volume 30, No. 1, pp. 74- 83, January 2007b.

Lall, P., Panchagade, D., Iyengar, D., Shantaram, S., Suhling, J., Schrier, H., High Speed Digital Image Correlation for Transient-Shock Reliability of Electronics, Proceedings of the 57th ECTC, Reno, Nevada, pp. 924-939, May 29 – June 1, 2007c.

Lall, P., Gupte, S., Choudhary, P., Suhling, J., Darveaux, R., Cohesive-Zone Explicit Sub-Modeling for Shock Life- Prediction in Electronics, 57th ECTC, pp. 515-527, Reno, NV, May 29- Jun 1, 2007e.

Lall, P., Choudhary, P., Gupte, S., Health Monitoring for Damage Initiation & Progression during Mechanical Shock in Electronic Assemblies, Proceedings of the 56th ECTC, San Diego, California, pp.85-94, May 30-June 2, 2006a.

Lall, P., Gupte, S., Choudhary, P., Suhling, J., Solder-Joint Reliability in Electronics Under Shock and Vibration using Explicit Finite-Element Sub-modeling, Proceedings of the 56th ECTC, pp. 428 – 435, 2006b.

Lall, P., Panchagade, D., Choudhary, P., Suhling, J., Gupte, S., Failure-Envelope Approach to Modeling Shock and Vibration Survivability of Electronic and MEMS Packaging, Proceedings of the 55th Electronic Components and Technology Conference, pp. 522-529, 2005.

Lee, S. W., Tsui, Y. K., Huang, X., and Yan, C. C., Effects of Room Temperature Storage Time on the Shear Strength of PBGA Solder Balls, Proceedings of the 2002 ASME International Mechanical Engineering Congress and Exposition, Paper IMECE2002-39514, pp. 1-4, 2002.

Lopes, E., Lead-free Soldering European RoadManp Soldertec Report 2003.

Lee, N. C., Lead-Free Soldering—Where the World is Going, Indium Corporation of America Report, Clinton, NY 1999.

Liu, S., Wang, X., Ma, B., Gan, Z., Zhang, H., Drop Test and Simulation of Portable Electronic Devices, International Conference on Electronic Packaging Technology, pp.701-704, June, 2005.

Macek, R., Silling, S., Peridynamics via finite element analysis, Finite Element in Analysis and Design 43, pp 1168-1178, 2007.

Meier, K., Roellig', M., . Wiese S,. Wolter K.-J., "Characterisation of the Mechanical Behaviour of SAC solder at High Strain Rates," 11th. Int. Conf. on Thermal, Mechanical and Multiphysics Simulation and Experiments in Micro-Electronics and Micro-Systems, pp 1-6, EuroSimE 2010.

Meyer, M., Dynamic behavior of Materials, John Wiley and sons, Inc, 1994.

Miller, T., Schreier, H., Reu, P, High-speed DIC Data Analysis from a Shaking Camera System, Proceedings of the SEM Conference, Springfield, Massachusetts, June 4-6, 2007

Moon, K. W., Boettinger, W. J., Kattner, U. R., Biancaniello, F. S., and Handwerker, C.A., "Experimental and Thermodynamic Assessment of Sn-Ag-Cu Solder Alloys," Journal of Electronic Materials, Vol. 29, pp. 1122-1136, 2000.

Ong,Y.C., Shim,V.P.W., Chai, T.C., LimC.T., Comparison of Mechanical Response of PCBs Subjected to Product-Level and Board-Level Drop Impact Tests, Electronic Packaging Technology Conference, pp. 223-227, June, 2003.

Pang, J. H. L., Xiong, B. S., and Low, T. H., Low Cycle Fatigue Models for Lead-Free Solders, Thin Solid Films Vol. 462- 463, pp. 408-412, 2004.

Park, S., Shah, C., Kwak, J., Jang, C., Pitarresi, J., Transient Dynamic Simulation and Full-Field Test Validation for A Slim-PCB of Mobile Phone under Drop Impact, Proceedings of the 57th ECTC, Reno, Nevada, pp. 914-923, May 29 – June 1, 2007a.

Park, S., Reichman, A., Kwak, J., Chung, S., Whole Field Analysis of Polymer Film, Proceedings of the SEM Conference, Springfield, Massachusetts, June 4-6, 2007b.

Park, S., Al-Yafawi, A., Yu, D., Kwak, J., Lee, J., Goo, N., Influence of Fastening Methods on the Dynamic Response and Reliability Assessment of PCBS in Cellular Phones Under Free Drop, Proceedings of the ITherm, Intersociety Conference on Thermal and Thermo-mechanical Phenomena, Orlando, Florida, pp.876-882, May 28-31, 2008

Peterson, D., Cheng, C., Karulkar, P.C., Characterization of Drop Impact Survivability of a 3D-CSP Stack Module, Proceedings of the 58th Electronic Component and Technology Conference, Orlando, Florida, pp. 1648-1653, May 27-30, 2008.

Plumbridge,W., J., Gagg, C., R., "Effects of strain rate and temperature on the stress strain response of solder alloys," JOURNAL OF MATERIALS SCIENCE: MATERIALS IN ELECTRONICS, 10, pp 4 6 1- 4 6 8, 1999.

Puttlitz, K., Stalter, K., Handbook of Lead-Free Solder Technology for Microelectronic Assemblies, Marcel Dekker, 2004.

Qin, F., An, T., Chen, N., "Strain Rate Effects and Rate-Dependent Constitutive Models of Lead-Based and Lead-Free Solders," Journal of Applied Mechanics, Vol. 77 / 011008-1, Jan, 2010.

Rahn, A.,The Basics of Soldering, Wiley-Interscience, 1993.

Ramberg,W., Osgood, W., "Description of Stress-Strain curves by three parameters," NACA Technical Note No. 902, 1943.

Scheijgrond,P.L.W., Shi, D.X.Q., Driel, W.D.V., Zhang,G.Q., Nijmeijer, H., Digital Image Correlation for Analyzing Poratable Electronic Products during Drop Impact Tests, 6th International Conference on Electronic Packaging Technology, pp. 121– 126, Aug 30.-Sept 2. 2005.

Seah, S.K.W., Lim, C.T.,Wong, E.H., Tan, V.B.C., Shim, V.P.W., Mechanical Response of PCBs in Portable Electronic Products During Drop Test, Electronic Packaging Technology Conference, pp. 120-125, May, 2002.

Silling, S., A., Askari, E., A meshfree method based on the peridynamics model of solid mechanics, Comput. Struct. 83, pp1526-1535, 2005.

Silling, S., Zimmermann, M., Abeyaratne, R., Deformation of Peridynamic bar, J. Elaticity 73, pp 173-190, 2003.

Silling, S., Refomulation of elasticity theory for discontinuities and Long-range forces, J. Mech. Phys. Solids 48, pp175-209, 2000.

Siviour, C., R., Walley,S., M., Proud, W., G., Field, J., E., Mechanical properties of SnPb and Lead-free Solder at High Rates of Strain, Journal of Physics D: Applied Physics 38, 4131-4139, 2005.

Srinivasan, V., Radhakrishnan, S., Zhang, X., Subbarayan, G., Baughn, T., Nguyen, L., High Resolution Characterization of Materials Used In Packages Through Digital Image Correlation, InterPACK Conference Proceedings, July 17-22, 2005.

Suh, D., Kim, D., Liu, P., Kim, H.,  Weninger, J., Kumar, C., Prasad, A, Grimsely, B., Tejada, H., Effect of Ag content on fracture resistance of Sn-Ag-Cu Lead-free Solder under high-strain rate condition,  Elsevier, Volume 460-461, pp 595-603, July 2007.

Suhling, J., Mechanical Engineering Department course MECH6310 at Auburn University Spring 2007.

Tsui, Y. K. , Lee, S. W., and Huang, X., Experimental Investigation on the Degradation of BGA Solder Ball Shear Strength Due to Room Temperature Aging, Proceedings of the 4th International Symposium on Electronic Materials and Packaging, pp. 478-481, 2002.

Vianco, P., "Fatigue and Creep of Lead-Free Solder Alloys: Fundamental Properties," ASM International, pp.67-106, Aug 2005.

Wong, E.,H., Selvanayagam, C.,S., Seah, S.,K.,W., Van Driel, W., D., Caers, J., F., J., M.,. Zhao, X.,J., Owens, N.,Tan, L., C., Frear, D., R.,. Leoni, M.,. Lai Y.-S, Yeh C.-L," Stress–Strain Characteristics of Tin-Based Solder Alloys for Drop-Impact Modeling," Journal of ELECTRONIC MATERIALS, Vol. 37, No. 6, 2008.

Xu, L., Pang, J., Che, F., Impact of Thermal Cycling on Sn-Ag-Cu Solder Joints and Board – Level Drop Reliability, Journal if Electronic Materials, Volume 37, Issue 6, pp 880-886, June 2008.

Yeh, C., Lai, Y., Transient Analysis of Board-level Drop Response of Lead-free Chipscale Packages with Experimental Verifications, Electronic Components and Technology Conference, pp. 695-700, June, 2004.

Zhang, Y., Cai, Z., Suhling, J.,C., Lall, P., Bozack, M., "Aging Effects in SAC Solder Joints," *Proceedings of the SEM Annual Conference* June 1-4, 2009 Albuquerque New Mexico USA, 2009.

Zhang, Y., The Effects of Aging on the Mechanical Behavior of Lead Free and Mixed Formulation Solder Alloys, PhD dissertation, 2009.

http://etd.auburn.edu/etd/handle/10415/2/browse?value=Zhang%2C+Yifei&type=author.

Zhou, P., Goodson, K. E., Sub-pixel Displacement and Deformation Gradient Measurement Using Digital Image- Speckle Correlation (DISC), Optical Engineering, Vol. 40, No. 8, pp 1613-1620, August 2001.

Zhua, F., Zhang, H., Guana, R., Liu, S., "Effects of temperature and strain rate on mechanical property of Sn96.5Ag3Cu0.5," Journal of Alloys and Compounds 438 , pp 100–105, 2007.